STARS

2009

Characterization Of An Inline Row Impingement Channel For Turbine Blade Cooling Applications

Mark Ricklick
University of Central Florida

Showcase of Text, Archives, Research & Scholarship

CHARACTERIZATION OF AN INLINE ROW IMPINGEMENT CHANNEL FOR TURBINE BLADE COOLING APPLICATIONS

by

MARK A. RICKLICK
B.S.M.E University of Central Florida, 2006

A dissertation submitted in partial fulfillment of the requirements
for the degree of Doctor of Philosophy in Thermo-Fluid Sciences
in the Department of Mechanical, Materials, and Aerospace Engineering
in the College of Engineering and Computer Science
at the University of Central Florida
Orlando, Florida

Fall Term 2009

Major Professor: Jay Kapat

ABSTRACT

Gas turbines have become an intricate part of today's society. Besides powering practically all 200,000+ passenger aircraft in use today, they are also a predominate form of power generation when coupled with a generator. The fact that they are highly efficient, and capable of large power to weight ratios, makes gas turbines an ideal solution for many power requirement issues faced today. Designers have even been able to develop small, 'micro' turbines capable of producing efficient portable power. Part of the turbine's success is the fact that their efficiency levels have continuously risen since their introduction in the early 1800's. Along with improvements in our understanding and designs of the aerodynamic components of the turbine, as well as improvements in the areas of material design and combustion control, advances in component cooling techniques have predominantly contributed to this success. This is the result of a simple thermodynamic concept; as the turbine inlet temperature is increased, the overall efficiency of the machine increases as well.

Designers have exploited this fact to the extent that modern gas turbines produce rotor inlet temperatures beyond the melting point of the sophisticated materials used within them. This has only been possible through the use of sophisticated cooling techniques, particularly in the 1st stage vanes and blades. Some of the cooling techniques employed today have been internal cooling channels enhanced with various features, film and showerhead cooling, as well as internal impingement cooling scenarios. Impingement cooling has proven to be one of the most capable heat removal processes,

and the combination of this cooling feature with that of channel flow, as is done in impingement channel cooling, creates a scenario that has understandably received a great deal of attention in recent years.

This study has investigated several of the unpublished characteristics of these impingement channels, including the channel height effects on the performance of the channel side walls, effects of bulk temperature increase on heat transfer coefficients, circumferential heat variation effects, and effects on the uniformity of the heat transfer distribution. The main objectives of this dissertation are to explore the various previously unstudied characteristics of impingement channels, in order to sufficiently predict their performance in a wide range of applications. The potential exists, therefore, for a designer to develop a blade with cooling characteristics specifically tailored to the expected component thermal loads.

Temperature sensitive paint (TSP) is one of several non-intrusive optical temperature measurements techniques that have gained a significant amount of popularity in the last decade. By employing the use of TSP, we have the ability to provide very accurate (less than 1 degree Celsius uncertainty), high resolution full-field temperature measurements. This has allowed us to investigate the local heat transfer characteristics of the various channel surfaces under a variety of steady state testing conditions. The comparison of thermal performance and uniformity for each impingement channel configuration then highlights the benefits and disadvantages of various configurations.

Through these investigations, it has been shown that the channel side walls provide heat transfer coefficients comparable to those found on the target surface, especially at small impingement heights. Although the side walls suffer from highly non

uniform performance near the start of the channel, the profiles become very uniform as the cross flow develops and becomes a dominating contributor to the heat transfer coefficient. Increases in channel height result in increased non-uniformity in the streamwise direction and decreased heat transfer levels. Bulk temperature increases have also been shown to be an important consideration when investigating surfaces dominated by cross flow heat transfer effects, as enhancements up to 80% in some areas may be computed. Considerations of these bulk temperature changes also allow the determination of the point at which the flow transitions from an impingement dominated regime to one that is dominated by cross flow effects. Finally, circumferential heat variations have proven to have negligible effects on the calculated heat transfer coefficient, with the observed differences in heat transfer coefficient being contributed to the unaccounted variations in channel bulk temperature.

DEDICATED TO SUNDAY; WITHOUT YOU I WOULD STILL HAVE ALL MY

SNEAKERS.

ACKNOWLEDGMENTS

I first must acknowledge my family; they are the reason I am who and where I am today. Your guidance and support has been invaluable. Dr. Kapat, I've been lucky to have you as an advisor and as a role model. Seeing the dedication and passion you have for science kept me strong through the difficult moments. Vaidy, Jeff, Lee, An, Jason, everyone that has been a part of building 44, The City Beautiful, OWC, my friends here and at home, Cutler Ridge, dog parks, sugar free Monster, the Dutch, camouflage forts, potato guns, the MMAE staff, mud and sand, technology, turbines, Red Bull Flugtag, squirrels, birthday cake, Mitch Hedberg, coffee, Oxygen & Acetylene, soccer, 20 hour road trips, conferences & expos, toll booths, the Legendary JC's, Orange Ave., Photoshop, parachutes, S&S, lab coats & safety glasses, National Committee for Fluid Mechanics Films, electricity, Albert Einstein, Osborne Reynolds, Zhuangzi, Google, NASA, Home Depot, Wikipedia, homemade computers, senior design groups, curiosity, Schaum's outlines, jokes, the sun, blood, sweat, and tears, compressed air lines, lunch time, all three generations of Hank Williams, math, physics, and all sciences in general; you have made my graduate career unforgettable.

TABLE OF CONTENTS

LIST OF FIGURES

LIST OF TABLES

NOMENCLATURE

A_{cs}	Cross Sectional Area
A_h	Heater Surface Area (m^2)
C_d	Discharge Coefficient
Cp	Specific Heat at Constant Pressure (kJ/kg·K)
D	Jet Diameter (m)
D_{ch}	Channel Hydraulic Diameter (m)
f	Friction Factor
G	Mass Flux (kg/s·m^2)
h	Heat Transfer Coefficient (HTC) (W/m^{2}K)
$\bar{h}$	Average Heat Transfer Coefficient (W/m^{2}K)
i	Jet Number (1,2…N$_h$)
L	Channel Length (m)
$\dot{m}$	Mass Flow Rate (kg/s)
$\dot{m}_a$	Actual Mass Flow Rate (kg/s)
N_h	Number of Impingement Holes
Nu	Nusselt Number
P	Static Pressure (kPa)
P_0	Total Pressure (kPa)
P.D.	Pressure Driven
Pr	Prandtl Number
q''	Heat Flux (W/m^2)

Q'	Heat Input per Unit Length (W/m)
Q	Total Heat Input (W)
R	Air Gas Constant (J/kg·K
R_h	Heater Resistance (ohm)
Re	Reynolds Number
S.D.	Suction Driven
SW	Side Wall
T	Temperature (K)
T_0	Total Temperature (K)
TC	Thermocouple
TW	Target Wall
U	Channel Exit Velocity (m/s)
UC	Uniformity Coefficient
V	Voltage Potential
x	Streamwise Location
X	Streamwise Distance (m)
Y	Spanwise Distance (m)
Z	Impingement Height (m)
η	Thermal Performance Parameter
κ	Ratio of Specific Heats
ρ	Air Density (kg/m^3)

Subscripts

blk	Mixed Mean (Bulk) Value
c	Cross Flow Value
e	Exit
eff	Effective
j	Jet Value
$loss$	Quantity Lost to the Environment
P	Plenum
R	Reference Value
w	Wall Value
0	Base Line Value

CHAPTER 1   **INTRODUCTION**

1.1   Turbine Blade and Component Cooling

Through studies of various thermodynamic cycles, and specifically the Brayton Cycle used to describe gas turbines, it is obvious that increases in turbine inlet temperature increase the potential power and efficiency of the system. A generic, ideal Brayton cycle is shown in Figure 1-1.
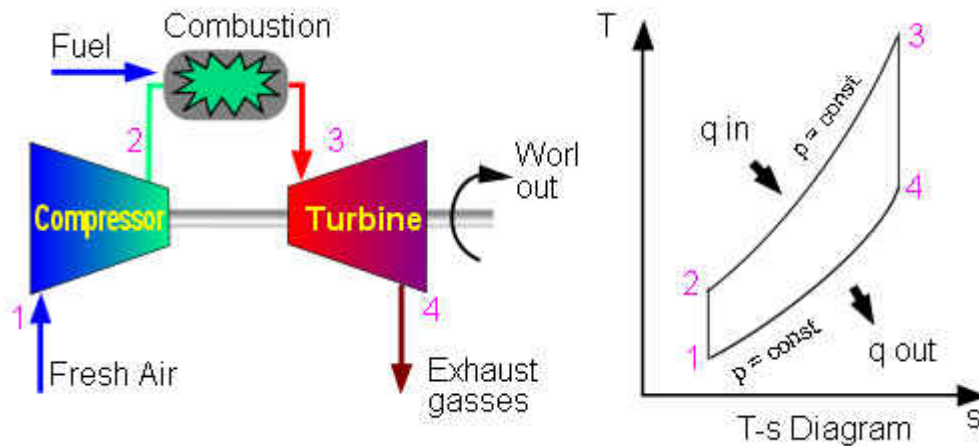
Figure 1-1: Ideal Brayton Cycle

The maximum temperature (T3) is ultimately governed by the maximum attainable combustion temperature, the adiabatic flame temperature, on the order of 2000-3000°C for the standard fuels used today. However, typical super alloys used within the machine cannot withstand these extreme temperatures, with a typical melting temperature on the order of 1500°C or less. The limiting T3 would then have to be considerably less than this temperature to promote component life, as was the case for the early turbine systems. However, with the use of modern cooling techniques, as described in Figure

1-2, designers have been able to push this maximum temperature beyond the material melting point while maintaining acceptable component life.
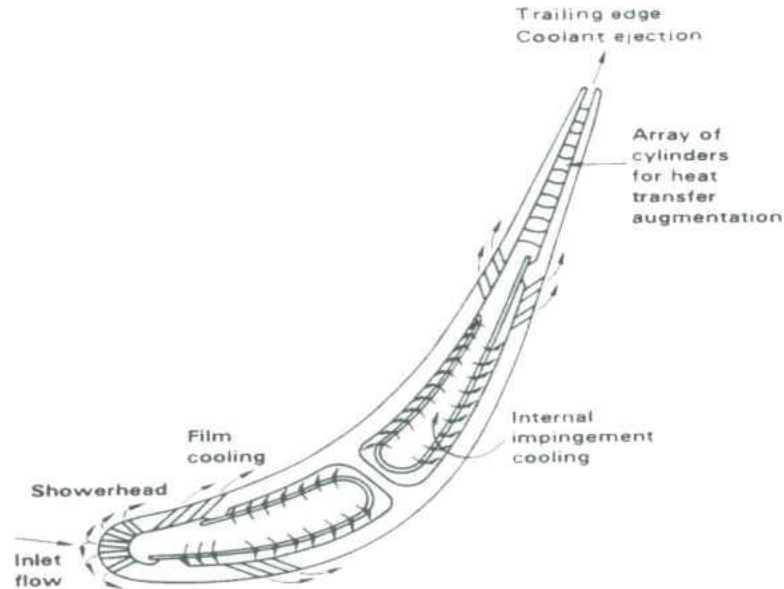
Figure 1-2: Turbine Blade Cooling Techniques (Taylor, 1980)

Figure 1-3 and Figure 1-4 exemplify the importance and benefit of this increased inlet temperature. However, it is important to realize that the air used for cooling is normally bled from the compressor, therefore reducing the efficiency of the machine. It is therefore important that these cooling techniques not only be effective, but also efficient in the sense that minimal amounts of coolant are used. In order to further increase the power and efficiency of these machines, it is necessary for both material and thermo-fluids engineers to continuously work to improve the materials and cooling methods used within the machines.
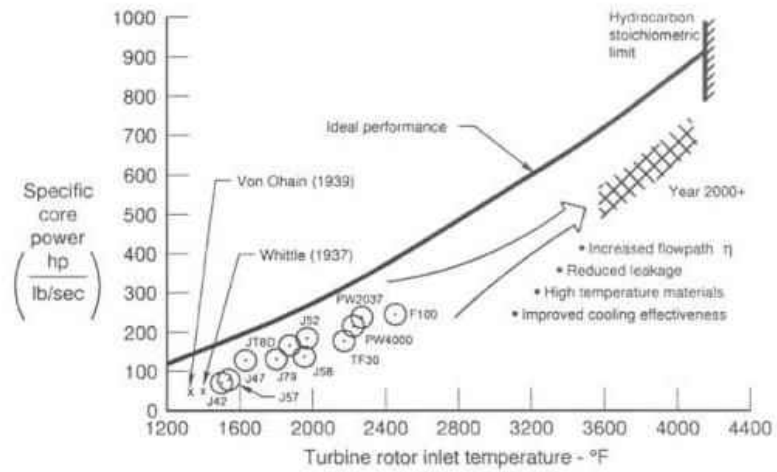
Figure 1-3: Turbine Inlet Temperature versus Power (Sautner et al., 1992)
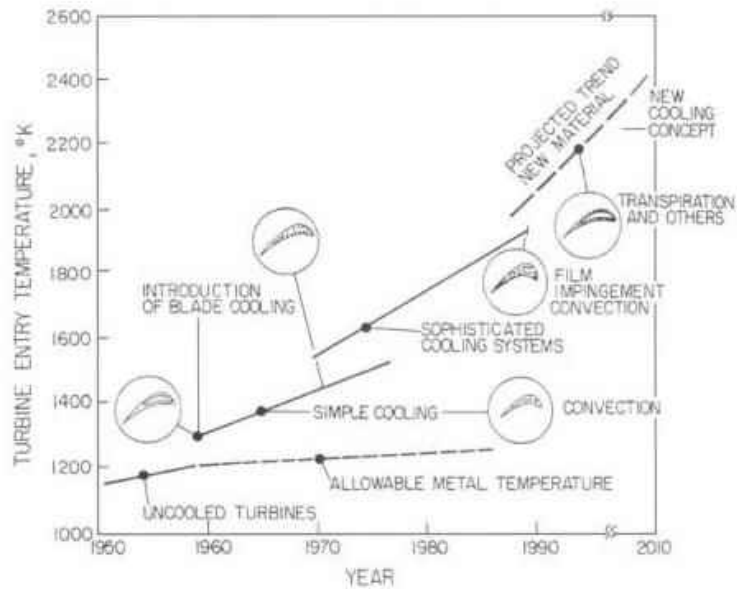
Figure 1-4: Inlet Temperature Variation over Recent Years (Clifford, 1985)

All of the various components exposed to the hot gas require some sort of thermal protection, either through cooling, protective coatings, or most commonly a combination of the two. This includes stators, blades, endwalls, and combustor walls. As shown in Figure 1-5, numerous cooling techniques are used within the blade to maintain safe

3

material temperatures. Showerhead and film cooling are techniques employed to protect the blade from the hot gas path. The driving concept behind these cooling techniques is to place a thin blanket of cooler air along the material surface so as to protect the metal from the hot gasses. Heat transfer within the internal cooling channels is typically augmented with pin fins in the trailing edge (to also add structural support) and ribs or dimples in the mid-cord and leading edge sections. Finally, internal impingement cooling has begun to receive more attention in recent years, typically being used to cool the leading edge region, but designs have also used the method in the mid-cord sections as well.
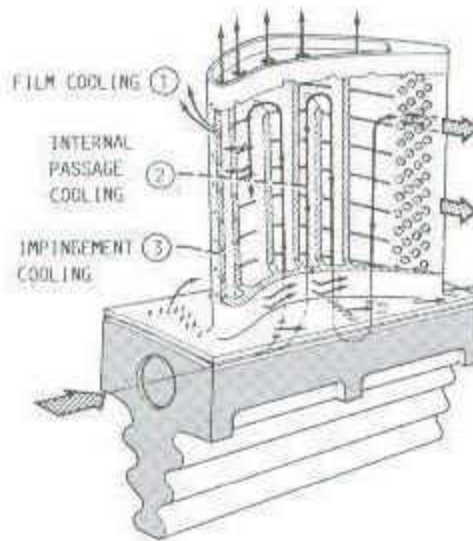
Figure 1-5: Blade Cooling Techniques (Gladden and Simoneau, 1988)

1.2   Impingement and Impingement Channel Cooling

The motivation behind impingement channel cooling is to remove the heat at a location close to its source so that the less entropy is generated during the heat removal process; yielding a process that is thermodynamically more efficient. Since heat comes

from the hot gas path in an airfoil, the impingement channel cooling technique places the cooling ducts right beneath the airfoil's hot surface. This cooling involves impinging cool air from inside the airfoil through small holes leading to a narrow channel near the airfoil's outer skin. These impingement channels are produced in numerous ways, including the placement of a perforated inserts within a hollow airfoil, casting, and machining. Because of limitation of available space, the cooling duct has also become small.

The flow structures within these cooling ducts are very complex. The fact that the jets are constricted to flow in a single direction creates a cross flow that increases in velocity as it passes each jet, as seen in Figure 1-6. This developing cross flow interacts with the downstream jets in a very complicated fashion, including the development of vortical structures (Fox, 1993). Downstream jet effects are dampened and impingement locations are shifted in the downstream direction, and eventually dominated by the developing cross flow. The literature has also shown that the impinging jets also produce vortex structures similar to those found in pin fin arrays, when a cross flow is imposed against them. These vortical structures, along with the competing effects of the secondary flows from impingement, determine the wall surface temperature distribution. The hot surrounding gases are also entrained within the shear layer of the jet due to these vortex structures (Fox, 1993). To complicate matters further, although a constant supply pressure may be present, as the cross flow velocity increases, a decrease in channel pressure results. This forces a distribution in jet velocities, with downstream jets being faster. These effects are highly dependent on the channel's cross-sectional size. Because of this variation of individual jet Reynolds number along the channel, impingement

channel flows are characterized by the average jet Reynolds number. With the right combination of geometry and hole design, this cooling technique can take advantage of this highly turbulent flow scenario.
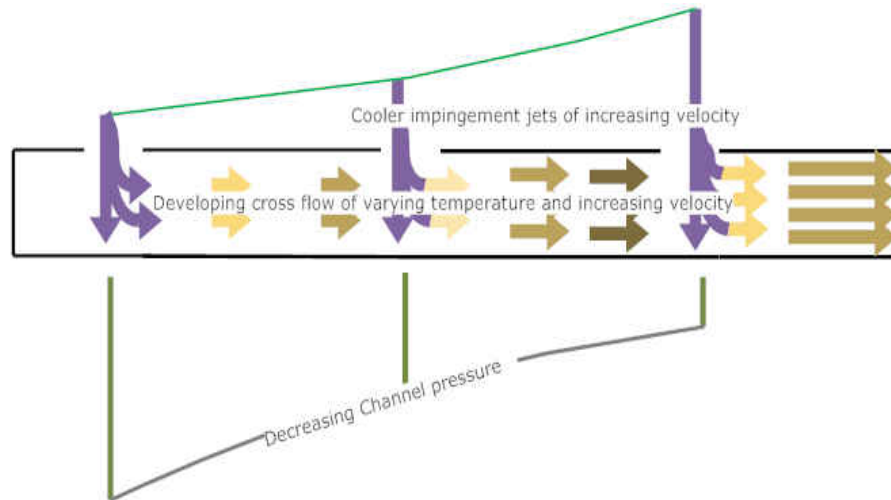
Figure 1-6: Impingement Channel Flow Scenario

Extensive amounts of research in the areas of impingement, impingement channels, and circumferential boundary conditions have been presented throughout the years. Nevertheless, there has not yet been a tight, universal correlation developed to predict the heat transfer characteristics of an impingement channel (Son et al, 2001). This is partially due to the complex flow structures formed in these cooling scenarios, which are so sensitive to the channel geometry.

1.3   Objectives

Several objectives have been defined for the current work. Initially, through several steady state heat transfer tests and a thorough literature survey, the general performance characteristics of impingement channels should be defined. We would like

to investigate these characteristics on multiple wetted surfaces, including the previously neglected channel side walls. Because of the known behavior of the wall jet developed after impingement, there exists some potential for the side wall to participate in the heat removal process. Numerical studies will be performed to help further understand some of the phenomenon occurring within the channel. Attempts will also be made to quantify the uniformity of the heat transfer profile, rather than only considering the heat transfer levels themselves. This will be beneficial in the sense that smaller temperature gradients, and thus thermal stresses, will be generated in practice, which could effectively allow higher gas temperatures (Bunker, 2007). Because of the nature of impinging flows, heat transfer reference temperatures are often assumed to be the jet temperature. However the development of the actual mixed mean flow temperature is often important to designers. Models will be developed to better predict these trends, and an investigation into their effects on the calculated heat transfer trends will be conducted. In order to fully explain the applicability of these cooling configurations, it is also important to understand the losses associated with them. Especially considering advancements in turbine efficiency will require cooling designs that present minimal parasitic effects. For these reasons, a friction factor and thermal performance parameter will be defined for these configurations, and investigated.

With a thorough understanding of the impingement channels, we intend to make some conclusions on the effective and efficient use of these cooling devices. This will be done through the examination of multiple channel characteristics, highlighting channels that would perform best, considering certain penalties.

CHAPTER 2   **LITERATURE REVIEW**

2.1   <u>Introduction</u>

Impingement channels have slowly developed over the years. Initially, studies of impingement jets and internal channel flows were performed separately. The idea of impingement channel cooling did not begin to receive considerable attention until the late 1970's and early 1980's. Prior to this, researchers concentrated on conventional channel flow cooling techniques, as well as introductory studies into the heat transfer performance of unconstrained impingement jets. As designers began to apply the large heat carrying capacity of impingement jets to cooling scenarios where the jets become constrained (such as into finned heat sinks or the leading edge section of an airfoil), investigations into impingement channels soon began. It was not long before engineers understood the potential of this cooling method, and some forms of it began to show up in equipment designs, such as gas turbines blades. Investigations of both the unconfined impingement jet, as well as the impingement channel continue to explore and attempt to correlate the effects of various characteristics. The flow characteristics of the unconstrained free jet and impingement jet have been thoroughly studied and explained, and the structures within the impingement channel are gaining clarity every year. As the structures found within these flow features are highly complex, analytical methods are not yet able to provide accurate predictions to their heat transfer performance in the practical range of jet Reynolds numbers employed in the gas turbine industry; this results in the need for continuous experimental investigations. Nevertheless, numerical results are growing in popularity and accuracy, as models become more sophisticated.

2.2   Turbine Blade Cooling

As previously discussed, the sophistication of the component cooling techniques has allowed for the continuous increase in turbine inlet temperatures. In fact some of the literature has shown that current technology levels would be impossible to reach without the advancements in cooling. For example, material advancements have led to about a 4 degree Celsius increase in firing temperature per year, compared to cooling advances which have contributed to increases of 11 degrees Celsius per year (Boyce, 2006). Clearly, the importance of component cooling is extreme. Component cooling has become customary, rather than unusual as it was during the early days of the gas turbine (Downs, 2009). These techniques have varied over the years, depending on knowledge, capabilities, as well as system requirements. Current technologies have pushed future high tech machines to inlet temperatures on the order of 2000K, employing minimal coolant usage in a hybrid cooling scheme (Ito, 2005). This method of cooling uses a combination of closed loop cooling with steam as a working fluid and compressor bled film.

Some of the high tech internal channel cooling technologies employed today include skewed broken rib patterns. These features not only help break up the boundary layer and increase turbulence, their skewness also creates secondary flows which also promote heat transfer. These configurations have been shown to enhance heat transfer up to 3 times that expected in a smooth channel at an equal Reynolds number (Ito, 2005).

Future advances, however, are becoming more difficult to achieve, as the rate of technology improvement has somewhat reached a plateau in the past 10 years (Bunker, 2007). Advanced cooling techniques have become more advanced, but have added further complexity to the machine as well. As the requirements for turbine cooling systems becomes more demanding, it has become necessary to pause and consider where these technologies have come, and where they need to go. Bunker (2007), and Downs and Landis (2009) have published critical papers in this regard. Both papers agree on the trend towards distributed near wall cooling technologies, where small cooling channels are methodically distributed on the turbine blade. The goal is to reduce the thermal resistance of the airfoil, while minimizing thermal gradients and stresses. This would result in cooling methods that not only produce high levels of heat transfer, but also yield uniform component temperature profiles.

Chyu et al (2009) and Sierra et al (2009) also acknowledge the importance of reduced thermal gradients and their dependence of cooling uniformity. An attempt to accomplish this is considered by Chyu, through the use of impingement channels, or skin cooling as it is sometimes called. It is clear that advanced machines will have these additional uniformity requirements.

Bunker (2007) also discusses the fact that cooling technologies must require minimal amounts of coolant usage as well as frictional losses. However, this is often neglected in the literature. Achieving maximum coolant effectiveness is also a crucial factor that should be considered, and is a major area of improvement with current designs (Downs, 2009). These characteristics must be explored for all cooling technologies, including impingement channels.

2.3   <u>Impingement Cooling</u>

Impingement cooling can be placed in one of several categories. An impinging jet can be submerged, where the same fluid is found throughout the cooling channel, or unsubmerged, where the injected fluid is different than the surrounding fluids. Only submerged jets will be considered here, since they are most applicable to turbine applications. Impingement jets can also be unconstrained, where the jet simply exits an orifice, possibly impinging against a target surface, with no surrounding walls. On the other hand, the constrained jet is confined within a cavity or channel, altering its behavior. The constrained jet is of greatest interest to the turbine industry, as the exiting jets must be confined within some exiting channel, however an introduction to unconstrained jets is of the utmost importance for one to get a full understanding of an impingement channel cooling scheme.

2.3.1   Unconstrained Impingement

The impingement jet has been proven to possess one of the highest potentials for heat transfer. By exhausting a jet of fluid against a surface, large heat transfer coefficients result in the area of stagnation. This allows designers to effectively remove heat from close to its source, yielding a more thermodynamically efficient cooling process. These jets possess large fluctuating velocities, with typical turbulence levels on the order of 25% (Han, 2000), aiding in the efficient removal of heat. The stagnating flow also yields very thin boundary layers, further aiding in high heat transfer rates.

The structure of an impinging jet has been described by several authors (Viskanta, 1993, and Martin, 1977 for example), and compared to that of a free jet. They have similar structures, until the impinging jet comes close to the stagnation region. For the impingement jet, there is a free jet region, which leaves the jet hole with a velocity distribution dependant on the hole geometry. For example, if the hole is short enough (L/D <1), as is typically seen in industry, a nearly flat velocity profile results, as is shown in Figure 2-1. However, if the hole is long, as has been done in some experiments in the literature (Bradbury, 1965) for example), the flow becomes developed and resembles a parabolic profile, with a maximum at the centerline. A potential core is defined as the portion of the free jet where the velocity is at least 95% of that at the nozzle exit. This core length is significant, as impingement heights beyond this length yield lower heat transfer values, and heights below this value often yield negligible changes in heat transfer rates. The potential core eventually dissipates as a result of mixing with the surrounding fluid, with typical lengths being reported from 4 to 7.7 in different papers (Livingood, 1973 & Martin, 1977). These differences are attributed to the difference in turbulence intensity, geometric scales, and the velocity profile at the jet exit (Glauer, 1956). The turbulence generated within these jets due to the mixing with their surroundings is much larger than would be experienced in typical pipe flow (Liu, 2006). This is a direct contributor to the large heat transfer rates provided by the impinging jet.
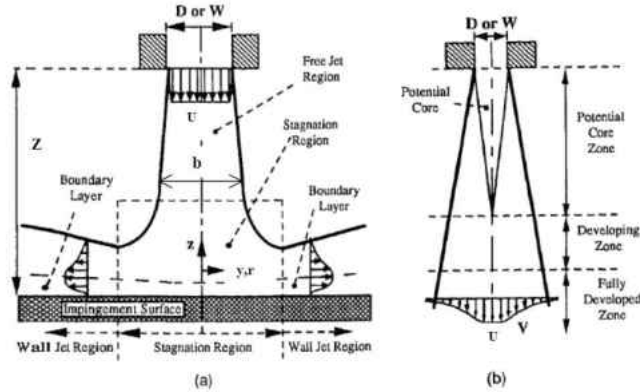
Figure 2-1: Hydrodynamics of Impinging Flow (Viskanta, 1993)

The free jet eventually impinges a surface, creating a stagnation region as seen in Figure 2-1. According to Martin (1977), the height of this stagnation region is on the order of 1.2 diameters. However, as is true with the potential core length, many factors potentially affect this value. The pressure at the stagnation point is a maximum, typically equal to the total pressure of the plenum. However, with larger impingement heights (Z/D>5), the stagnation point is not able to recover all of the source pressure (Lucas, 1992). This is due to the excessive mixing losses that occur as the jet travels though the surrounding fluid. From this stagnation point, where the velocity is zero, the flow accelerates horizontally outward, eventually reaching a maximum value at the edge of the stagnation region. Here the pressure has returned to ambient; at about 1.6 to 3 diameters away from the stagnation point (Gauntner, 1970). Because of mixing and the exchange of momentum with the fluid in this region and the surrounding fluid, the flow eventually transforms to a decelerating wall jet.

For the single unconstrained impingement jet, the wall jet velocity eventually reduces to zero in an exponential fashion (Liu, 2006). Work performed by Glauert (1956), showed the wall jet consists of 2 distinct regions; an inner layer similar to a

13

typical boundary layer, and an outer layer similar to free turbulent flow. At the boundary of these regions the velocity is a maximum, with the profiles being accurately described in the literature (Gauntner, 1970). The region within the stagnation zone is typically laminar, due to the stabilizing effect of the acceleration of the flow; as the flow decelerates, however, a transition to a turbulent nature occurs.

As is typically done in turbine blade cooling, these impinging jets are placed in arrays, changing their flow distribution slightly, mostly in the vicinity of the wall jet. As the wall jets from two impingement jets approach each other, they collide and create a 2nd stagnation point. This second stagnation point further aids in heat transfer augmentation, as the boundary layer is again diminished in this location.

Impingement channel heat transfer rates are calculated in a somewhat traditional fashion, according to the following equation:

$$h = \frac{q''}{(T_W - T_R)}$$

<div align="right">(1)</div>

Here the reference temperature is often taken as the plenum or adiabatic wall temperature. Using the constant plenum temperature for impingement channel cooling considerations, as will be shown, can introduce some slight misconceptions when examining all of the wetted surfaces. However, this results in little errors when considering surfaces dominated by impingement flow, as the jet's high velocity helps it maintain nearly uniform temperatures (at or near the plenum temperature).

Numerous characteristics affect the heat transfer performance of an impinging jet. These include jet velocity profile, jet hole geometry, impingement height, surface

conditions, turbulence levels, as well as numerous other characteristics (Liu, 2006). Eckert et al (1953) gave a correlation of the Nusselt number for the stagnation point of a cylinder exposed to uniform flow. Similar features are seen within an impinging jet situation, suggesting a similar power law relationship might be used for empirical correlations in the form of $Nu=C*Re^a*Pr^b$. However, it has been shown that things are not as simple as suggested, since so many factors affect the performance of the jets. It is for this reason that no tight correlation for the performance of impinging jet arrays confined in a channel has been made available in the literature. There are, nonetheless, several correlations available for specific situations.

Experiments were performed by C.J. Hoogendoorn in 1977 to study the effects of turbulence at the stagnation point of an impingement jet. Effects of impingement height and turbulence levels were reported. Results showed a similar relationship to the stagnation zone of a cylinder in a free stream. Increases in turbulence yielded similar effects to increasing the impingement height. Compared to small channel heights, and low turbulence levels, a much broader heat transfer profile is observed with larger turbulence levels. The jet was created though a long tube, with variations in the exit condition examined as well. The often mentioned 2nd peak was also observed, at impingement heights of less than 8 diameters. This was related to the increases in turbulence levels in the developing wall jet. Turbulence measurements were taken in the free jet at the theoretical impingement location, and surface temperatures were recorded with liquid crystals. It was shown that the main effects of turbulence are only seen at the stagnation point, and a correlation similar to that found for cylinders in cross flow was developed relating the turbulence level and Reynolds number to the impingement Nusselt

number. Effects of turbulence on the Nusselt number, as well as velocity and turbulence

distribution levels are presented in Figure 2-2 and Figure 2-3.
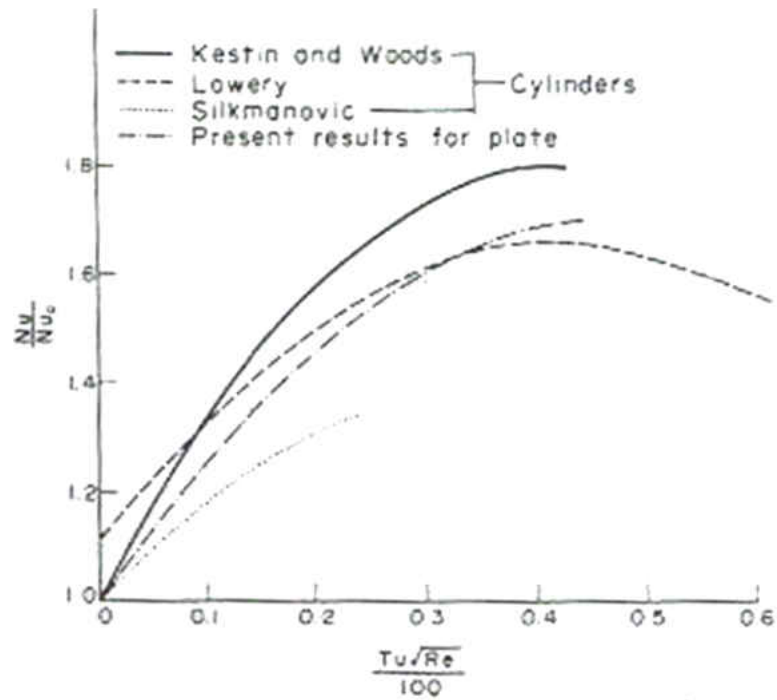
Figure 2-2: Turbulence effects on stagnation Nu (Hoogendoorn (1977))
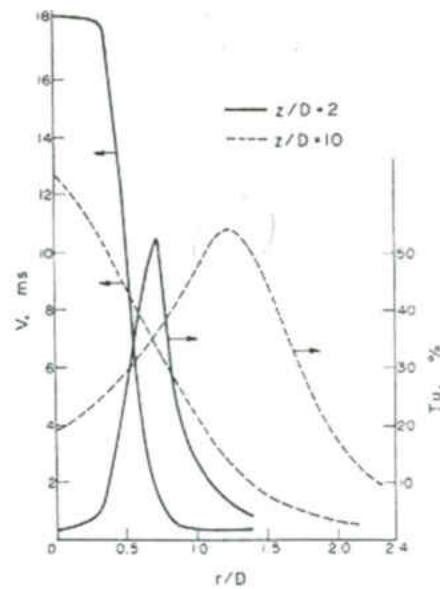
Figure 2-3: Z/D effect on turbulence and velocity (adapted from Hoogendoorn , 1977)

Lucas et al (1992) investigated the effects of jet Reynolds number, jet to target

spacing, as well as boundary condition effects on the heat transfer of a jet impinging

against a flat surface. TLC was used to measure temperature, in a 3 temperature problem

17

method. The jet plate temperature was controlled, and the target plate was uniformly heated. Jet Reynolds numbers of 7.5k, 15k, and 30k were tested at impingement heights of 1, 2, and 3 jet diameters. Flow visualization was performed with a small tuft suspended from a nylon string. The jet Reynolds number was decreased from 30k to 15k at a Z/D of 1 and no significant changes were observed in the flow field. A considerable amount of flow was seen to circulate back toward the jet along the top surface. This was the result of a donut recirculation vortex, which was also observed by others in the literature (Bower et al (1981)). At Z/D of 1 and 2 the heat transfer rate was almost the same (as was also observed by Yan et al (1992) at Z/D of 2 and 4). This is the result of the potential core of the jet extending to the plate surface for smaller heights, where the pressure coefficient equaled 1. As the channel height is varied within the potential core length, similar velocity profiles impinges the surface, yielding comparable results. Differences in the heat transfer rates between this paper and others was attributed to the fully developed jet used in many of the other papers, as well as possible higher turbulence intensity values. They concluded, among other things, that the temperature of the plate has a significant effect on the impingement heat transfer coefficient for Z/D of 2 and 3, possibly because of the larger recirculation zone created.

2.3.2 Constrained Impingement

Experiments performed by Florschuetz et al (1980, 81, 83) included jet impingement on a heated segmented plate. Numerous array geometries and channel sizes were tested. Early tests were performed to determine array averaged heat transfer coefficient, and general trends in Nusselt numbers were observed. In his later works, a

one dimensional model was developed that predicted the flow distribution (local jet and cross flow mass fluxes), allowing the development of a correlation based on geometric parameters and local jet to cross flow mass flux ratios. However, this correlation is not universal, and does not account for potential contributions of the side walls or jet plate. Investigations were also performed on the effects cross flow had on the jet discharge coefficient.

In order to explain some of the discrepancies encountered in their earlier works, Florschuetz and Isoda (1983), performed a set of studies investigating the effects of channel cross flow on the jet hole discharge coefficient. The discrepancies they discussed involved differences in the predicted total mass flow rate (determined from the C_d value and pressure profile) and the actual measured mass flow rate. These differences were significant when initial cross flow ratios were high or channel heights were small, up to 42 percent in some cases. It was then decided to perform a special set of tests to parametrically study the effects of cross flow velocity and impingement height on the jet discharge coefficient. This work investigated an important aspect of impingement channel cooling, as it is traditionally the case that discharge coefficients are calculated under a no cross flow situation. This proves acceptable under normal situations. In order to investigate these effects, a slightly modified test section was developed, where an initial, adjustable, amount of cross flow was introduced upstream through the impingement of two jets. This cross flow then approached the normal impingement array which was used in their previous experiments. In order to carefully characterize the effects of the cross flow, mass flux ratios (G_c/G_j) from zero to 8 were tested. This required pressure ratios on the order of 2.7, which are admittedly not very easy to obtain.

This was significant, since all prior studies had only investigated mass flux ratios up to 0.8. Most importantly, their results defined a maximum value of G_c/G_j, beyond which the discharge coefficient is strongly influenced by the cross flow ratio. This value was dependant on the array geometry however, as were the equations used to correct the discharge coefficient. This value was typically around 0.6 and above. They also showed that although the discharge coefficient significantly varied for large variations in cross flow, it remained relatively constant for variations in jet Reynolds number, regardless of G_c/G_j. With knowledge on the behavior of the discharge coefficient versus cross flow, Florschuetz et al was able to modify the flow model previously developed for a constant discharge coefficient. This model required a numerical approach, and is not necessary under normal cross flow ratios.

Osama Al-aqal (2003) conducted experiments to determine heat transfer distributions on the walls of a narrow channel with jet impingement and cross flow. The experiments had three different configurations of impinging jets; a single row of 6 holes, 2 rows totaling 24 holes, and 3 rows totaling 54 holes. Each case has the same total hole area, allowing a comparison between the results. Reynolds numbers between 5k and 33k were tested. Local data was taken on the target wall and the jet-issue wall using the transient liquid crystal technique. Jets introduced through piping leading into the test section, with the flow constrained to leave in a single direction. The optimal distance for jet-to-target plate spacing was found to be dependent on the hole geometry as well as the wall which is being optimized, with taller channel heights usually being more beneficial to the jet plate. Local heat transfer on the target plate showed much more uniformity at small jet-to-target spacing than large jet-to-target spacing. His work also compared

impingement heat transfer values to those calculated using smooth pipe correlations. He showed that target surfaces yielded enhancements between 1.3-5.4, depending on the geometry, with the 54 hole case yielding the highest. Jet plate enhancement values ranged from 0.7-2.7 times pipe flow values. Again the 54 hole case performed the best. Also important is the fact that the 6 hole case yielded minimum values below those predicted by smooth pipe correlations. This suggests a need for improved methods of heat transfer regarding this surface. References were also made to previous works by M.K. Chyu (1997), where a numerical operation was developed to convert a heat transfer coefficient based on inlet temperature to one based on local bulk flow temperature for cooling though a long cooling channel with roughened vortex generators.

U. Uysal (2005) varied the jet hole-size and spacing for a jet array impinging in a duct. Jet diameters were increased in the streamwise direction, in an attempt to achieve impingement at locations downstream where the cross flow has become significant. Local data was again obtained for the target plate and the jet-issue plate. Variable hole sizes, as expected, resulted in increased heat transfer values in the downstream location, opposite to the uniform profile. Key heat transfer features in the impinged region directly underneath a jet bear strong resemblance to that of a single jet, implying that direct interaction among neighboring jets in the array is weak. Heat transfer characteristics on the jet-issuing plate are very different from that on the target plate. Overall, the average heat transfer on jet plate is approximately one-third to one-half the corresponding values on target plate.

The effects of jet Reynolds number is typically the dominating flow characteristic that is controlled during impingement experiments. In this sense, the majority of existing

works are only applicable at low Mach numbers, where compressibility effects within the jet are negligible. Modifications to the correlation developed by Florschuetz were made by Park et al (2006). Through experiments controlling both Mach number and Reynolds number independently, it was shown that increases in jet Mach number led to increases in stagnation heat transfer levels, while Reynolds numbers were maintained constant. Mach numbers between 0.1 and 0.6, and Reynolds numbers between 11,000 and 59,000 were tested.

K. Mushatat (2007) numerically studied the two dimensional effects of various parameters on a slot jet cooling geometry. A k-ε model was used to model the turbulence effects, and a wall function was employed to account for wall effects. The number of jets was varied from 2 to 4, and an initial uniform cross flow was also present. Channel heights as well as slot spacing effects were also examined, both in the heat transfer results as well as in the flow field. Results were compared against published works, with satisfactory results. This proved the applicability of the k-ε method to effectively simulating impingement flow scenarios. The stream line contours effectively displayed the recirculation zone downstream of the jets, near the jet plate. This is the driving force to the jet temperature increase described by Lucas (1992) and others. Further work was done to see the effects 2 different rib layouts had on the target surface heat transfer coefficient and flow field results. Distinct peaks resulted in the heat transfer profile, due to the recirculation zones that were evident in the streamline and velocity distribution profiles. His results highlighted the importance of rib placement with respect to the jets; and the fact that the recirculation zone behind the jets becomes larger with increases in jet velocity. Finally, heat transfer values increased with increases in these recirculation

zones, and decreased with increases in channel height, similar to the results found in the available literature. Figure 2-4 shows some of the flow field results produced in this work, and highlights the potential use of features for heat transfer augmentation. Although the flow field produced by a slot jet is inherently simpler than that produced from a circular jet, this paper highlights the usefulness of using commercially available numerical tools to understand the flow behavior in these channels.
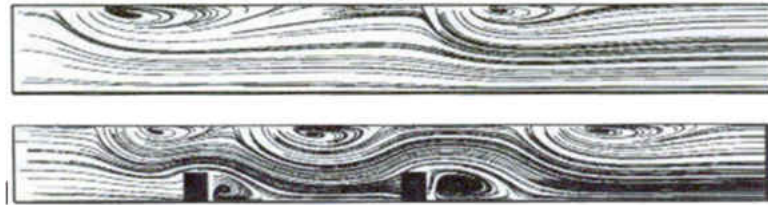
Figure 2-4: Streamline comparison between smooth and ribbed impingement (Mushatat , 2007)

Round impinging jets, especially constrained within a channel, have often been studied numerically, as it is know that available models need improvement before their results are completely accepted. Studies have been carried out (El-Gabry, 2005) that have compared experimental results with different numerical models. Their model considered the performance of a standard k-ε model and that of a Yang-Shih model, with varying impingement angles. Reynolds numbers between 10,000 and 35,000 were tested at a Z/D equal to 1 and 2. Square arrays, with no side walls were used in both the experiment and model. The k-ε model was shown to yield results that matched experimental results most closely for the orthogonal jet arrangement. Deviations were greatest at stagnation locations, as well as at the locations of heat transfer minima. The deviation are attributed to the inaccuracies in the way the model accounts for the mixing between the jet and the cross flow. This also resulted in errors in the location of some of

the downstream stagnation regions, where experimental results experienced higher degrees of deflection at higher Reynolds numbers. It was shown though that the numerical predictions did accurately describe the trends in heat transfer, serve as an important means of understanding the flow.

Changmin Son et al (2001) performed a comprehensive study on an engine representative impingement channel cooling system. Pressure loss and pressure distribution, as well as surface shear stress visualization results accompanied the local heat transfer results. Results were then compared to industry standard predictions. Results were also normalized by smooth channel predictions at the channel's exit conditions. Besides the introduction of several modified measurement and visualization techniques for impingement cooling, their results showed that the downstream locations yielded results 50% lower than those at the impingement locations. Shear stress patterns also effectively showed the effects of the stagnation point, wall jet development, and secondary stagnation points, proving its usefulness in this area. These shear stress patterns are shown in Figure 2-5.
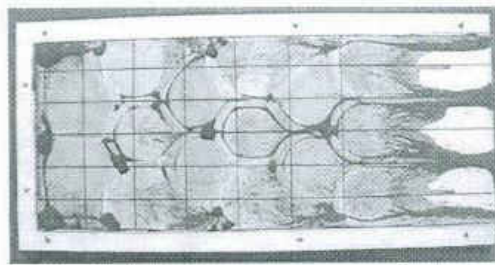
Figure 2-5: Shear stress visualization (Son et al, 2001)

An important result of the location and size of these small cooling ducts is the fact that the heat flux they experience is highly non-uniform. The target surface is exposed to hot gases on its back side, and therefore has significantly higher heat rates than the other

surfaces. It has been suggested through examples in the literature, by Reynolds (1963) for example, that variations in Nusselt number may result from highly non-uniform heating applications. This work, along with those presented by Sparrow (1963), were purely analytical, making various assumptions about the diffusive properties of the flow, as they would apply to flow through a cylinder, with well defined variations around the circumference. They suggested that with a given change in heat flux, there is a change, although smaller, in Nusselt number. With variations around the circumference, Reynolds for example, showed that peaks in Nusselt number were expected at areas of low heat flux, while decreases in Nusselt number were expected in areas of high heat flux. Later works by Black and Sparrow (1967) investigated the cylindrical problem experimentally. They reported trends similar to those presented in the analytical works, however less pronounced. It was then suggested by Black and Sparrow that these effects are negligible in typical cases, since the variations in Nusselt number are only a fraction of the changes in heat flux. However, the maximum variation of heat flux was only on the order of 1.25 times the average; which resulted in a 1.125 times variation in Nusselt number. The variations in heat flux we expect in the following tests are on the order of 2 to 4 times the average, suggesting larger variations in heat transfer coefficient. Work has also been done on the investigation of the jet plate temperature effects on impingement Nusselt numbers. It was shown by Van Truen et al (1994) and Lucas et al (1992), that at small impingement heights (Z/D<3), jet effectiveness and Nusselt numbers are effected by jet plate temperatures. This was the result of a resulting circulation within the channel, where the exhausted jet eventually is drawn upward toward the jet plate, and back toward the jet. This process eventually brings heat from the jet plate to the

incoming jet, increasing its temperature. This is seen in Figure 2-6 for two channel heights. Although there has been considerable work in the area of heat flux variations, none have been applied to an impingement channel, nor have experimented with such large and abrupt variations in heat flux.
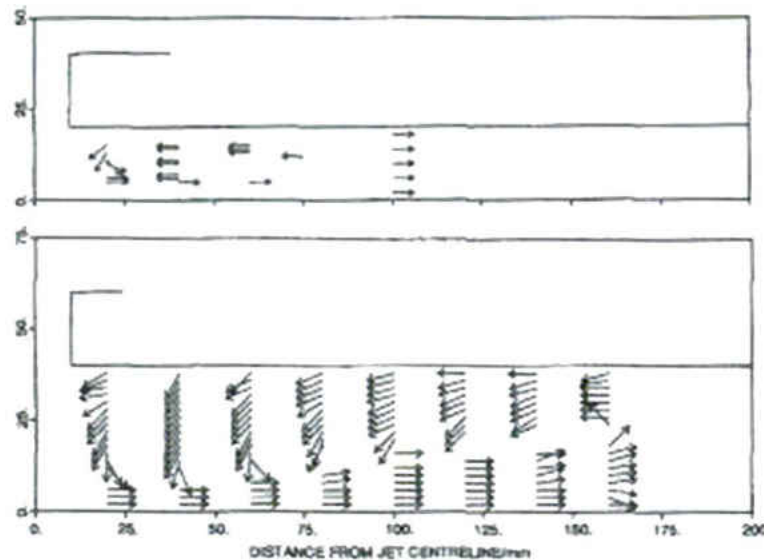
Figure 2-6: Impingement Flow Visualization (Lucas et al (1992))

The use of features to further enhance impingement heat transfer levels has only received moderate attention. M. Annerfeld et al (2001) studied the effect of several different types of turbulators experimentally, in an attempt to correlate the effects of obstructions placed in the gap of platform cooling scenarios. Four different turbulators (wedge, wing, cylinder, rib) were constructed from aluminum and placed on the target surface. Reynolds numbers between 20k and 65k were tested, with a constant hole spacing of 5 diameters and a variable channel height. Heat transfer enhancement values as well as thermal efficiency at a constant pumping power were compared in order to determine the most beneficial arrangement. These comparisons were considered as the enhancement over the smooth impingement channel. An infrared camera was used to

26

measure local temperature distributions. Overall enhancements between 1 and 1.3 were observed, resulting in thermal efficiencies between .4 and 1.2 when compared to smooth impingement cases. Enhancements were concentrated at the base of the turbulator, as well as right behind and diagonally downstream. The latter two positions were described as being the result of the creation of vortexes within the flow field. The enhancement beneath the feature was related to the fin effectiveness of the conductive material used. Tests were performed with features constructed from a material closer to those used within a typical turbine blade, resulting in only a slight reduction in average enhancement values. Enhancement levels increased with increases in cross flow velocities. The turbulators were positioned so that they would protect the downstream jets from the approaching cross flow. The results showed a reduced shift in the slightly increased stagnation point heat transfer level. They suggested the turbulator heights should be less than the full span of the channel, in order to maintain minimal pressure drops. Ribs and cylinders performed the best in this sense. Wider geometries tended to provide a better protection to the downstream jets, however resulted in significant pressure loss increases. Mass flux distributions were also slightly adjusted due to the placement of the features. Considerations were not expressed toward the resulting uniformity of the results, nor effects on the other surfaces. Also, only 1 pattern of each geometry was examined.

It was suggested in the work by Al-Aqal (2003) that a similar analysis as presented by M.K. Chyu (1998) be applied to impingement channels. This analysis performed by Chyu was applied to a channel with wedge shaped vortex generators along one surface. His study addressed the bulk temperature issue as it applied to transient experiments, as they are similarly based off of a plenum reference temperature. In his

work he examined four methods to determining a heat transfer coefficient based on a local bulk temperature, and applied the results to previously performed experiment. Two methods proved superior in their representation of the results, however, one method proved the simplest, yielding a converted heat transfer coefficient from the simple determination of some coefficient.

Some researchers in the area of impingement channel cooling have provided analysis using different schemes for determining the reference temperature (T_R). For example, Kercher and Tabakoff (1970) as well as Hilgeroth (1965), used a Log mean temperature difference (LMTD). This produced heat transfer coefficients that were artificially increased over the other available literature, since $(T_W-T_P) > \Delta(T_{LMTD})$. Kercher and Tabakoff determined from their work that heat transfer coefficients based on the plenum temperature were the most convenient and practical definition of heat transfer coefficient. However, as the amount of spent flow increases and the influence of the side walls become more severe, this may not be true.

The uniformity of the resulting heat transfer profile is often neglected, yet may contribute significantly to the applicability of a design. As mentioned, the thermal stresses are directly related to the thermal gradients resulting from the heat transfer distribution. It is important, therefore, to define and quantify the uniformity of various configurations, so that an optimal design may be selected. This issue is compounded further when considering the high variations associated with impingement cooling. For example, the heat transfer levels are the highest at impingement, and can decrease substantially away from this location. Film cooling geometries face a similar need for balance, where high effectiveness must be coupled with uniform profiles for effective

geometries. This issue was recently addressed in the work by Javadi and Javadi (2008), where a cooling uniformity coefficient was defined, and used to compare several film cooling geometries. They defined this coefficient based on the fact that the maximum film cooling effectiveness is found at the hole centerline, and an ideal distribution would equal this value throughout the spanwise direction. Variations about this maximum effectiveness value were then used to define the coefficient. Their work showed that all geometries tended toward a uniform profile in the downstream direction, due to the spanwise mixing of the coolant. However, blowing ratios tended to play a major role on the uniformity of the distribution, with some dependence on geometry. A similar analysis will be applied to the impingement channel cooling geometry, which as mentioned also suffers from non-uniformity in its cooling profiles.

CHAPTER 3   **METHODOLOGY**

3.1   Experimental Setup

The impingement facility constructed for this project has transitioned through several modifications and upgrades. In order to overcome some of the hurdles encountered during the first iteration, several changes were made and incorporated into a redesigned rig. Both have been validated, and used within the study, with no loss of data integrity, and will be described below.

3.1.1   General Rig Description

In order to attack the problems described above, we will perform several pressure and heat transfer tests. All will be carried out at steady state, constant heat flux (per wall) conditions, as will be described below. The experimental setup is designed to resemble a scaled-up airfoil impingement channel, or peripheral cooling as it is often called, like the one shown in Figure 3-1.
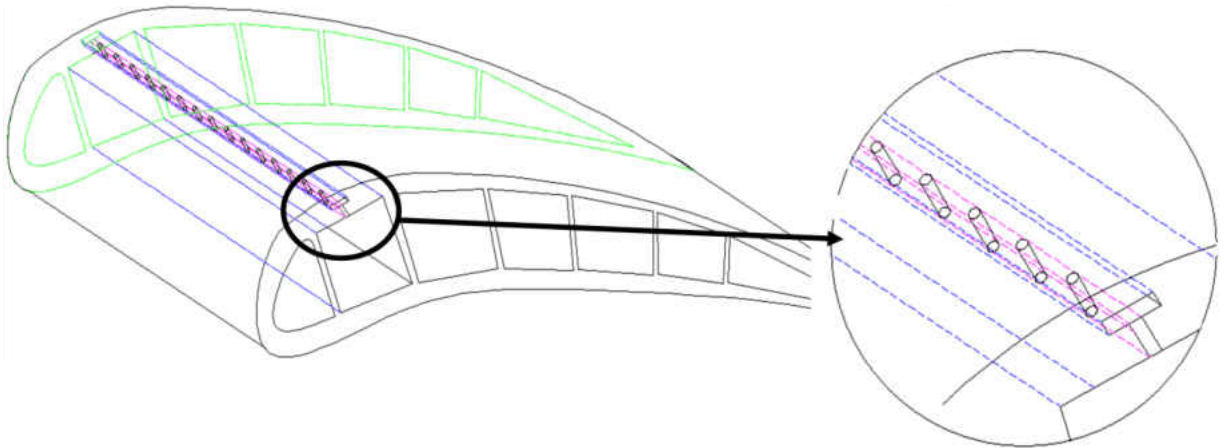
Figure 3-1: Peripheral Cooling Details

The first design iteration was set up with the impingement channel fed under pressure driven conditions. The walls were constructed in a manner that would allow the most channel dimension variations, with minimal parts. The second iteration, developed to overcome some problems to be discussed, was fed under suction mode, with wall constructed for ease of assembly, rather than number of machined parts.

3.1.2 Pressure Driven Rig Description

The test channel includes multiple jet-issue plates and a target plate which are enclosed on three sides as shown in Figure 3-2. Fifteen equal diameter inline impingement holes are milled into each jet plate, with counter bores so that the jet length is equal to 1 diameter, as seen in Figure 3-3. This is essential, and repeated in the literature, so that a nearly flat head jet velocity profile exits, rather than a developed profile. Typical turbines contain similar holes. This also helped minimize losses across the jet plate.
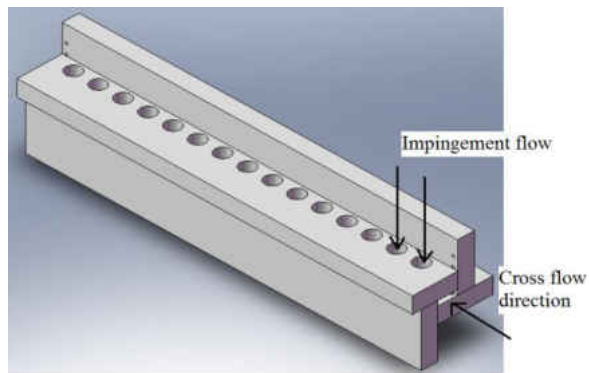
Figure 3-2: Test Section Geometry
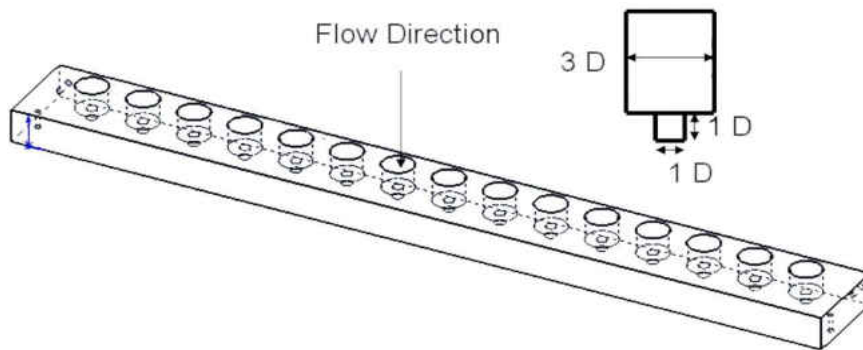
Figure 3-3: Jet Plate Geometry

Separate jet plates were constructed for each channel width (Y/D) to be tested,

with the remaining walls being assembled, as seen in Figure 3-4, in a fashion that allows

for simple adjustment of the channel height (Z/D) and width (Y/D). Hole spacing (X/D)

was adjusted, in multiples of 5 diameters, by plugging the unwanted holes, and ensuring a

smooth jet plate surface where the holes once were. At X/D of zero the channel is

blocked, so the exiting jets are forced to flow in a single direction. The first and last

holes are 5.25 diameters from the channel end. A maximum of 15 rows are tested,

departing slightly from the data presented in the literature. Most published results utilize

10 holes at the most, and leave some room at the end of the channel to explore how the heat transfer rates decrease once impingement has stopped. This decaying effect is not captured in our geometry, although the effect using an excessive number of jets is captured.
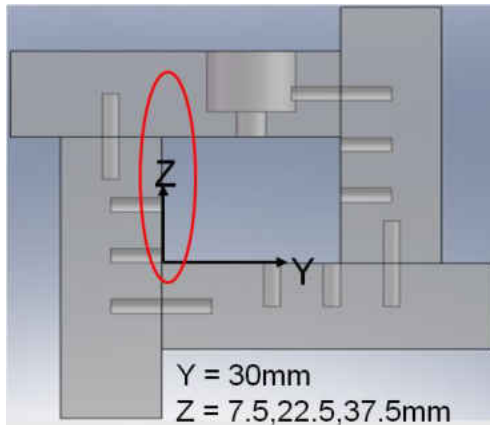
Figure 3-4: Test Section Cross Section

The test section was placed within the flow loop described in Figure 3-5. Flow is supplied from a centrifugal blower (Spencer VB 110), through two networks of pipes, one for impingement flow and one for additional channel flow (used for rig validation). An air to water heat exchanger was used to extract some of the heat dumped into the flow from the blower. The heat exchanger allowed us to maintain flow temperatures on the order of 30 deg C. Impingement flow traveled through a control and metering section, where flow rates were measured with a venture type flow meter; allowing the calculation of an average jet Reynolds number. The flow was then divided and sent through two 'side' plenums. Here the flow was conditioned with screens and straighteners. Inlet temperatures were measured here with type T thermocouples and recorded via a Data Acquisition System (Measurement Computing, 32 channels). The flow then entered a 'center' plenum, which was free of conditioners, were it was then forced through the

holes in the jet plate. This split plenum design allowed us to capture temperature sensitive paint (TSP) data on the jet plate surface, from above the plenum. The plenum dimensions were also chosen so that the flow traveled at negligible velocities within, and was not provided enough length to develop a significant boundary layer. Once the air impinged within the channel, it was constrained to flow in a single direction, eventually exiting into the atmosphere. The channel flow leg was similarly controlled and measured, but simply led into a removable entrance section and then into the channel entrance. This leg was only used for validation testing, and required the removal of the 'cap' at the channel entrance. This cap was simply clamped into place, and removed when necessary.
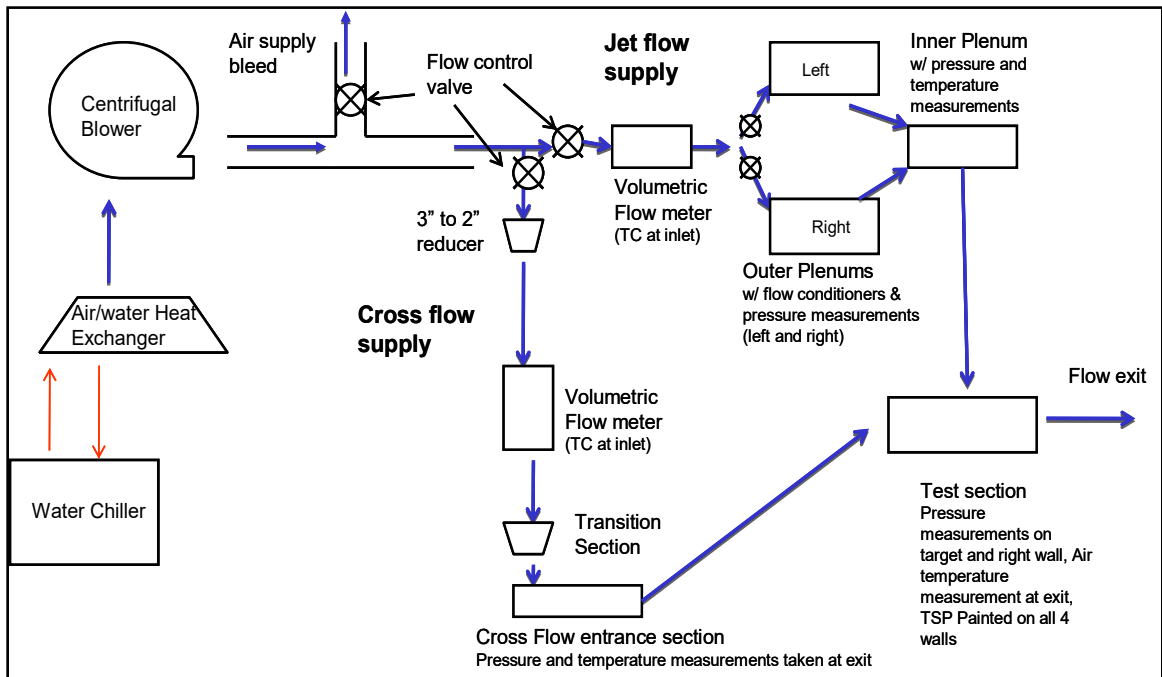
Figure 3-5: Flow Loop

Knowledge of the discharge coefficient of the jet plate used was necessary before actual testing could begin. This jet plate characteristic was determined by allowing the

jets to exhaust into the atmosphere unconstrained (i.e., the channel side and target plates were removed). Flow rates were measured with a venturi type flow meter and pressures were measured via a Scanivalve, over the expected range of pressure ratios and flow rates.

Pressure profiles along the channel length allow the determination of local jet and cross flow mass fluxes. For these tests, two walls (target and side) were instrumented with static pressure taps at locations between each jet. Pressures along the channel and in the plenum were again measured with a Scanivalve, and flow temperatures recorded via the DAQ. Flow rates were measured via the inline venturi flow meter. An image of a typical pressure test is seen in the Figure 3-6.

Figure 3-6: Pressure Test Set-up

Detailed heat transfer data is required for thermal analysis since there may be significant temperature gradients around the walls of these cooling passages and the heat transfer is driven by the local temperature difference. The walls instrumented with pressure taps were replaced with solid walls. All walls were constructed from ¾" acrylic

and are heated and controlled independently. Temperature Sensitive Paint (TSP), provided by ISSI, was coated on the back surfaces of each heater, allowing full field temperature measurements from the outside, as seen in Figure 3-7. The details of the temperature sensitive paint will be discussed later.

The target and side walls were instrumented with commercial foil heaters, constructed from a series of single heater strips, each 1 hole diameter in width, as seen in Figure 3-7. This allowed us to use a single heater for all geometries, turning off the unneeded heaters as the geometry grew smaller. Each active heater strip was connected in series (to increase the overall resistance) on a particular wall. These walls were then powered and controlled via a 130V (20A) VariAC. The jet plate heater was constructed from a 0.25mm thick Inconel heater (supplied by GoodFellow inc.), with holes milled out at the jet locations. This heater, of lower resistance, was powered via a 12V (30A) DC power supply. All voltages and resistances were measured with a high accuracy digital multimeter. Surface temperatures measured by the TSP were verified with 3 type T thermocouples places along the center line of each wall. Plenum temperatures were measured with a single type T thermocouple, and bulk temperature changes were measured with a 5 point thermopile rake.
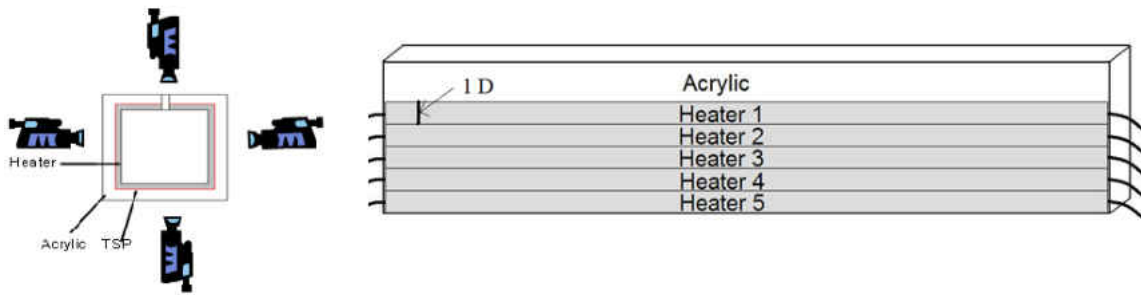
Figure 3-7: Heat Transfer Test Set-up

During heat transfer tests, the scientific grade singe CCD (charge coupled device) thermo-electrically cooled camera (PCO 1600) was positioned with the lens within 24" of the test section. Using a zoom lens, a single image of resolution 1200X1600 pixels, captured an image of approximately 4 inches square. This resulted in a typical resolution of 480 pix/mm^2. Because of the small area captured in each image, the camera was mounted to a computer controlled traversing system. A total of 9 images, with at least 30% overlap between steps, were taken along the 515 mm of temperature domain. The TSP was excited at the appropriate wavelength, with custom made LEDs (Light Emitting Diodes). This provided a nearly uniformly illuminated test surface. A single surface was recorded during each run, required a total of 3 runs (jet plate, side wall, target wall) per case. A typical heat transfer test, with data being recorded on the side wall, is seen in Figure 3-8.
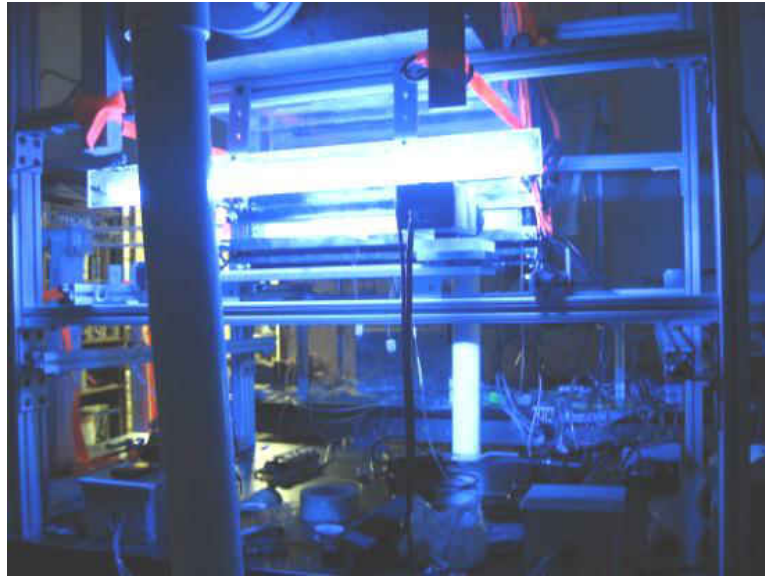
Figure 3-8: Typical Heat Transfer Test

The test matrix was chosen so that a representative variation in channel height and heat flux could be investigated. Because these cooling techniques are typically used to remove large amounts of heat, jet Reynolds numbers on the order of 50k and beyond are typically seen in turbine engines (Han et al, 2000). However, because our test section was supplied a positive pressure head, we were limited by the structural limitations of our plenum (constructed from ¼" thick acrylic). We therefore tested at the maximum average Reynolds number (and thus largest pressure ratio) that our plenum could safely withstand without damage. These initial tests were chosen so that effects of channel height, flux variation, and bulk flow temperature development could be investigated. Notice the smallest and middle channel heights (Z/D=1 & 3) determined the maximum Reynolds numbers tested. An overlap in Reynolds numbers was also scheduled, so that the effects of jet velocity could be captured independently. The tests conducted with the pressure driven rig are described in Table 3-1.

Table 3-1: Test Matrix A (Pressure driven)

Test Matrix A						
Case	Avg. Jet Re	X/D	Y/D	Z/D	No. Holes	Heated Surfaces
5.4.1Ai	17,000	5	4	1	15	A,B,C,D
5.4.1Aii						A,B,C
5.4.1Aii						B
5.4.3Ai	18,000	5	4	3	15	A,B,C,D
5.4.3Bi	45,000	5	4	3	15	A,B,C,D
5.4.3Bii						A,B,C
5.4.3Biii						B
5.4.5Bi	43,000	5	4	5	15	A,B,C,D
5.4.5Bii						A,B,C
5.4.5.Biii						B
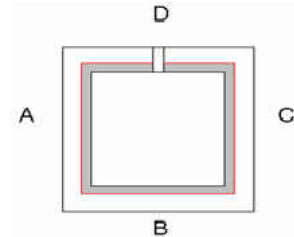
3.1.3 Suction Driven Rig Description

The previously described pressure driven rig, as mentioned, faced several design flaws. Particularly, because the rig was pressure driven, the maximum Reynolds number was limited not by the blower performance curve, but rather by the structural integrity of the rig. The heat that had to be removed from the inlet flow also provided additional, unnecessary complexities. Finally, although the first design of the wall assembly creatively allowed for small changes in channel dimensions without changing many parts, the method was excessively complicated, creating more difficulties than it prevented. It was then decided to redesign the test section so that it was not only suction driven, but assembled in a different manner.

Identical dimensions were used for critical dimensions, including channel dimensions, jet hole and counter-bore dimensions, and channel length. For this configuration, however, atmospheric pressure air was drawn through the jets, and then

out one end of the channel, controlled and measured in a similar fashion to the described pressure driven rig, as shown in Figure 3-9.
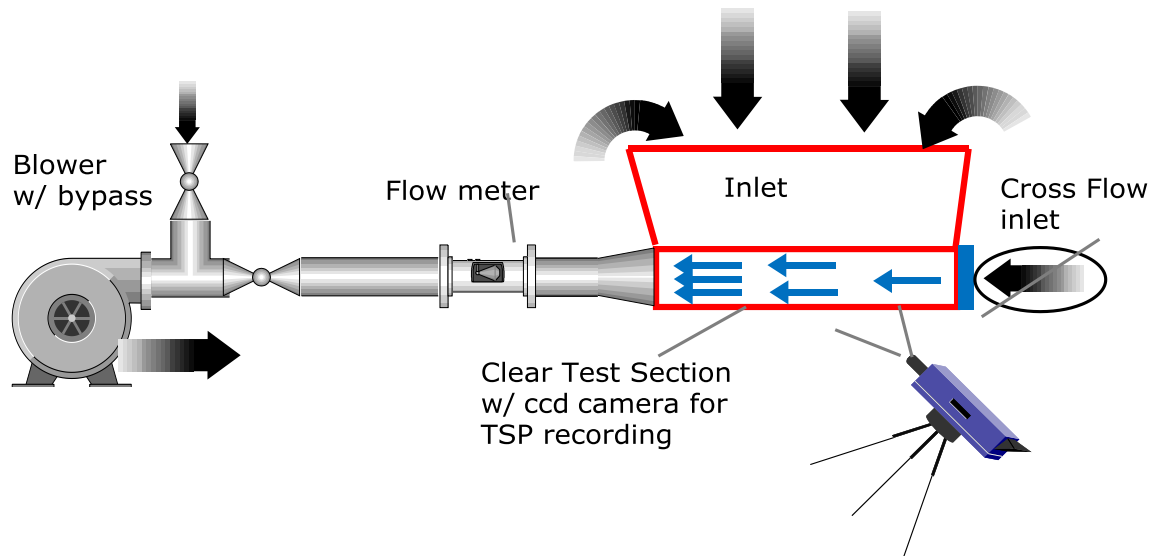
Figure 3-9: Suction Driven Flow Loop

Side walls were replaced for changes in channel height (Z/D), with all 4 walls being held together with threaded studs, and all joints sealed with thin Teflon gaskets. At X/D of zero, the channel is again capped, this time with a bolted end plate, sealed with gaskets. At the downstream side of the channel, flow was drawn, again being fed through a venturi flow meter and a flow control section. Once again, the removable cap at the channel start allowed a smooth channel scenario to be set up for rig validation.

Because of the nature of the suction rig, discharge coefficients could not be measured experimentally as they were with the previous set up. However, as the geometries are essentially the same, similar discharge coefficients were used for this model. These values were validated and adjusted by comparing measured mass flow

rates to those predicted from the pressure profile tests. Identical measurement equipment was used for this configuration.

With results from tests carried out with the first rig, to be discussed in a later section, it was understood that the pressure variations around the circumference of the channel were negligible. This, along with the fact that circumferential heat flux variations had minimal effects on calculated heat transfer coefficients, allowed for a slight variation in heater and pressure tap set up.

Foil heaters, encapsulated in Kapton tape, were again used to supply a heat flux on the surface. However, only the target and 1 side wall were instrumented, allowing pressure taps to be permanently instrumented on the other side wall, in a similar fashion to the previous rig. Heaters this time were constructed 5.08e-2mm steel foil, created in-house, again 1 diameter in width. TSP was painted against the test wall, and heaters were firmly attached using double sided Kapton tape, with temperature drops between the paint and flow surface accounted for. This value was typically on the order of 1 degree Celsius, at a typical heat flux of $7000W/m^2$. Heaters were powered with a DC 12V (30A) power supply, in parallel. A picture of the assembled test section is shown in Figure 3-10. With the current set up, and considering room air as the inlet air, typical wall to jet temperature differences on the order of 20-30 degree Celsius were easily achieved.

Figure 3-10: Assembled Suction Test Section

Identical instrumentation was incorporated into this rig, including inlet, exiting, and wall temperature and pressure measurements. Again, a computer controlled traversing system was used, however at a further distance, requiring only 3 total images in the streamwise direction. Extremely high resolutions were still captured, on the order of 100 pix/mm^2.

The remaining tests carried out on this rig, were intended to investigate pressure, heat transfer coefficient, and the uniformity coefficient distributions with variations in channel height and hole to hole spacing. These tests are outlined below in Table 3-2

Table 3-2: Test Matrix B (Suction Driven)

Test Matrix B						
Case	Avg. Jet Re	X/D	Y/D	Z/D	No. Holes	Heated Surfaces
15.4.1A	17,000	15	4	1	5	A or B
15.4.3A	18,000	15	4	3	5	A or B
15.4.3B	45,000	15	4	3	5	A or B
15.4.5A	18,000	15	4	5	5	A
15.4.5.B	45,000	15	4	5	5	A or B
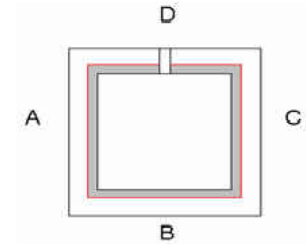
Tests conducted on this rig were designed to investigate some of the remaining parameters not fully explained during the first set of tests. This includes further investigations into the effects on uniformity, as well as thermal performance characteristics. By increasing the spacing of the holes (and thus decreasing the total number of holes and mass flow rate needed), it is possible to explore possibilities in removing similar amounts of heat with significantly less coolant. This, as mentioned, is one of the major concerns of turbine designers today.

3.2 Data Reduction

Data reduction took place at several stages during the testing process. Discharge coefficients were calculated early on, followed by flow distribution and friction factor calculations, and finally heat transfer and uniformity calculations. Various other analysis was also carried out for specific tests, in order to further investigate some specific characteristics. Each process will be described below.

Uncertainties were determined using the Kline-McClintock second power relationship. Effects of instrumentation, data acquisition and calibration techniques, as well as environmental variations were all accounted for in the analysis. Table 3-3 shows

the major relevant components of uncertainty, in Reynolds number and heat transfer

coefficient, worst case results are presented with a 95% confidence level.

Table 3-3 Major uncertainty contributions

	Re	h	f
Total Uncertainty (+/-)	8.50%	12.30%	8.73%

Uncertainty calculations included multiple pressure and temperature

measurements in order to reduce statistical measurement uncertainty, and corrections for

known biases.

3.2.1   Pressure Data

Discharge coefficients were calculated in the traditional fashion, as the ratio of the

actual flow rate to the ideal flow rate (calculated from compressible flow relations).

During testing, a pressure ratio, mass flow rate, and flow temperature were recorded.

Discharge coefficients were then calculated according to the following equation.

$$C_d = \frac{\dot{m}_a/N_h}{\frac{D^2 * \pi}{4} * P_0 * \left(\frac{P}{P_0}\right)^{\frac{\kappa+1}{(2*\kappa)}} * \sqrt{\frac{2*\kappa}{(\kappa-1)} * \frac{1}{R*T_0} * \left[\left(\frac{P_0}{P}\right)^{\frac{\kappa-1}{\kappa}} - 1\right]}}$$

(2)

With knowledge of the discharge coefficient, and the recorded pressure profiles,

local jet and cross flow mass fluxes were calculated. By rearranging the above equation,

it is possible to solve for a single jet's mass flow rate with knowledge of the static

pressure ratios and air static temperature. The mass flow rate of the cross flow approaching each jet location was simply the sum of the mass flow which exited from the upstream jets. Mass flux (G) was then defined by the following equation.

$$G = \frac{\dot{m}}{A_{cs}}$$

(3)

With knowledge of the channel pressure and flow distribution, it is also possible to calculate a representative channel friction factor so that it may be compared to that of a smooth pipe. Comparisons between different configurations can then be made, allowing some insight to the amount of extra work that has to be done to obtain the high heat transfer coefficients. This value should be representative of the frictional work required to push the fluid through the impingement array and channel. The channel friction factors are calculated according to:

$$f = \frac{(P_{pl} - P_e)}{L} * \frac{D_{ch}}{2\rho U^2}$$

(4)

The pressure drop includes the drop through the array, plus the work required to push the flow out of the channel. The plenum density and the maximum channel velocity were used for these calculations. For comparison, the Blasius solution for the friction factor through a smooth pipe is used. This friction factor is defined according to equation (5), where the maximum channel Reynolds number was used in the correlation.

$$f_0 = .184 * Re^{-1/5}$$

(5)

45

3.2.2 Temperature Data

Heat transfer data processing was slightly more involved, however all calculations were done in a traditional manner. Because testing was taken at steady state conditions, knowledge of the surface temperature, reference temperature, and applied heat flux is all that is required for heat transfer calculations. Heater material properties allowed for corrections on lateral conduction effects and temperature changes across the heater. Computations were carried out in a MATLAB code, so that every pixel of TSP data could be analyzed individually. This resulted in full field heat transfer coefficient calculations. Temperatures at each pixel location were determined by analyzing TSP images with an in-house developed code. Heat loss to the environment was accounted for through separate heat loss tests. The test channel was filled with insulation to prevent natural convection within the channel, and then heated under a no flow condition. Once the heaters reached typical operating temperatures, power input was recorded, knowing all of the produced heat is escaping into the atmosphere. Typical heat losses were on the order of 1 percent (due to the thick low conductivity acrylic walls). Reference temperatures were taken in 2 ways. The majority of the calculations were carried out in the traditional fashion, with the jet supply temperature used as the reference temperature. To investigate the effects of bulk temperature increases along the channel length, a second analysis was carried out, where the reference temperature was taken as a calculated bulk temperature, calculated in several alternative ways. This analysis accounts for the potential mixing between the jets and the developing cross flow. Data processing techniques will be discussed in the appropriate section.

Heater resistances were measured and catalogued, and it was verified that there were negligible thermal effects on the heater resistance. During testing, the voltage supplied to each heater was recorded with the digital multimeter. We were then able to determine total and effective heat fluxes as in the following equations.

$$q'' = \frac{V^2}{R_h * A_h}$$

(6)

$$q''_{eff} = q'' - q''_{loss}$$

(7)

Finally we were able to compute the heat transfer coefficient at each pixel location as:

$$h = \frac{q''_{eff}}{T_w - T_R}$$

(8)

Heat transfer results were presented as both local surface plots, as well as spanwise averaged plots, with the data being averaged as described in Figure 3-11.
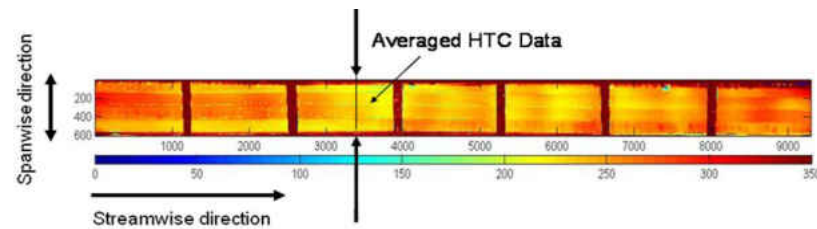
Figure 3-11: Averaging Scheme

As discussed earlier, one important characteristic of these channels is the uniformity of the heat transfer distributions. This value should give some sense to the variations, above and below the mean heat transfer coefficient. As mentioned, a similar analysis was done by Javadi and Javadi (2008), however considering the variations about the maximum effectiveness value. With small variations, the coefficient should approach

1, and zero for large fluctuations. For the current study, the heat transfer uniformity coefficient (UC) is defined according to equations (9).

$$UC = 1 - \frac{\sqrt{(h - \bar{h})^2}}{\bar{h}}$$

(9)

Uniformity calculations are presented in terms of local distributions spanwise averaged plots, as well as channel averaged results. Spanwise averaged uniformity coefficients are plotted with heat transfer distributions, on a secondary axis. This allows for the direct comparison between the two calculated values. These results, together with the heat transfer profiles, should give a clear picture of the performance of each channel.

3.2.3   Channel Performance

There have been limited studies which consider the thermal performance of cooling channels, with few applying this concept to impingement cooling channels. This is partially due to the fact that comparisons to smooth channel data is not necessarily intuitive, nor is the development of a friction factor definition. However, we would like to make these comparisons, in order to effectively compare these configurations against other available cooling schemes. An area averaged heat transfer coefficient is then compared to a channel averaged Dittus-Boelter estimate. Again, smooth pipe predictions were calculated at the maximum channel Reynolds number. In order to compare the effectiveness of the different cooling scenarios, a thermal effectiveness was defined, assuming constant pumping power between the cases according to equation (10):

$$\eta = \frac{\dfrac{h}{h_0}}{(\dfrac{f}{f_0})^{1/3}}$$

<div align="right">(10)</div>

Area averaged heat transfer coefficients were used, as well as maximum base line values (calculated at the channel exit), for this comparison. Although other methods of comparison are possible, the present method allows for a fair comparison of the channel configurations against a smooth pipe of equal total mass flow rate and channel cross-sectional area.

3.3   Experimental Procedure

Once knowledge of the discharge coefficient was obtained, as described in the previous section, pressure tests were conducted for each geometric case. Pressure profiles allowed the determination of how the flow develops within the channel, and should bring insight to some of the heat transfer data.

Pressure tests were performed before heat transfer testing, in order to avoid the effects of property changes with temperature. Once all the thermocouples and pressure taps were connected, testing began. The blower was started and allowed to run for 15 minutes so that it would reach steady operating temperatures. Total flow rates were measured with the venturi flow meter. The flow rate supplied by the blower was nearly constant, so the amount of flow sent to the test section was controlled by adjusting how much flow bypassed the test section. This gave a good control over the applied flow rates. Once the desired mass flow rate was achieved, and steady state was verified, pressure data was recorded. This was repeated for each channel geometry. Typical

testing took 4 hours to set up the test section, and 1 hour to collect data at all of the specified Reynolds numbers. The pressure ratio between the plenum and atmosphere was also recorded so that accurate conditions could be repeated for the heat transfer tests.

For heat transfer testing, the walls instrumented with pressure taps were removed and replaced with solid acrylic walls for the pressure driven rig. With the suction driven rig, pressure taps were simply capped so that no flow could pass through them. For each set of heat transfer tests, it was necessary to clean and re-paint the foils heaters. This was necessary in order to avoid any TSP measurement errors due to paint degradation as described in previous experiments in this facility (Liu, 2006). The locations where the heaters were attached for the first iteration of testing can be seen as blank spots in the local heat transfer data. This was avoided during the second phase of testing, due to the difference in heater assembly.

Before heat transfer tests began, an idea of how much of the heat generated by the heaters is actually conducted out of the test section into the ambient, rather than into the mainstream flow. This 'heat loss' rate would allow us to determine effective heat rates applied to each case. Heat loss tests were performed at steady state conditions. These tests were carried out by filling the interior of the channel with standard home insulation (R-30), in order to eliminate natural convection that might occur within the channel. We then apply a small amount of power to all of the walls, trying to maintain nearly uniform temperatures (on the order of expected testing conditions) around the circumference. Once steady state is achieved, we know that all of the heat being produced is being lost to the surroundings, since no flow is present. This heat loss test is repeated for several temperatures, and the results then correlated for future use. Because of the great deal of

time required for steady state (on the order of 6-8 hours per temperature point), typical testing took 3 days per geometry. Once complete, the insulation was easily removed and heat transfer testing was started.

As mentioned earlier, TSP measurement techniques require a reference image, taken at a uniform, known temperature. This was the first step in heat transfer tests. The LED illumination strip was allowed to warm up (in order to avoid variations in the intensity). Then reference images were taken at all locations along the test section, and the surface temperature was recorded. Uniform reference temperatures were verified by the three thermocouples placed on each wall. The walls were then covered, to prevent paint degradation, and the heaters were all powered prior to starting the flow, at a low heat rate. This allowed time for the test section to warm up, so that steady state could be achieved faster. Once the acrylic walls were near typical operating temperatures, the desired flow rate was achieved. Power was then increases and temperatures were observed (by monitoring the thermocouples). Once desired surface temperatures were obtained the channel was allowed to reach steady state (typically taking on the order of 3 hours); defined as the point when the surface temperature of the channel remained constant (within .25 deg C) for 30 minutes. At this point the wall covers were removed, and TSP images were taken along the tested wall. Temperatures were also recorded via the DAQ and LabView. After the images were taken, the wall covers were replaced and adjustments were made to the flow, or power input, before the process was repeated for all tests on the current wall. Because of the requirement for uniform temperature distributions during capturing of the reference images, only 1 wall could be recorded per run. A complete geometric case therefore took 3 runs (side, target, and jet plates). After

6-8 hours of set up, including TSP painting, a typical run took approximately 10-12 hours to complete, including camera/traversing system set up. A geometric case, therefore took approximately 35-40 hours to complete.

Variations due to the turbulent variations of the flow were also verified to have no effect on the results, as the capture times of the camera were long enough that these effects were averaged out. This, along with the rather slow response time of TSP, was verified through the comparison of successive images showing variations similar in magnitude to the acceptable noise levels. Capture times ranged from on the order of a half of second, to 4 seconds, depending on the lighting and paint quality.

3.4   Test Matrix

The complete test matrix is shown below in Table 3-4. The tests were chosen as to first explore some of the more general characteristics of the impingement channels, such as effects of circumferential heating variations and bulk temperature variations. This allowed proper adjustments to be made to the remaining analysis, investigating effects of Reynolds number and channel configurations.

Table 3-4: Complete Test Matrix

Complete Test Matrix							
Case	**Avg. Jet Re**	**X/D**	**Y/D**	**Z/D**	**No. Holes**	**Heated Surfaces**	**Mode**
5.4.1Ai	17,000	5	4	1	15	A,B,C,D	P.D.
5.4.1Aii						A,B,C	
5.4.1Aii						B	
5.4.3Ai	18,000	5	4	3	15	A,B,C,D	P.D.
5.4.3Bi	45,000	5	4	3	15	A,B,C,D	P.D.
5.4.3Bii						A,B,C	P.D.
5.4.3Biii						B	P.D.
5.4.5Bi	43,000	5	4	5	15	A,B,C,D	P.D.
5.4.5Bii						A,B,C	P.D.
5.4.5.Biii						B	P.D.
15.4.1A	17,000	15	4	1	5	A or B	S.D
15.4.3A	18,000	15	4	3	5	A or B	S.D
15.4.3B	45,000	15	4	3	5	A or B	S.D
15.4.5A	18,000	15	4	5	5	A or B	S.D
15.4.5.B	45,000	15	4	5	5	A or B	S.D

CHAPTER 4   **TEMPERATURE SENSITIVE PAINT**

Temperature sensitive paint (TSP), provides a convenient method for obtaining full field temperature distributions non-intrusively. Because this data acquisition method employs data capturing through a scientific grade camera, excellent quality results can be obtained from a carefully executed test. The method is also rather robust to varying testing conditions, allowing consistent calibration between different batches of paint and even lighting conditions. This allows for calibrations to be made in a separate calibration chamber, reducing some complexities of the test set up. TSP is a luminescent paint containing fluorescent molecules suspended within a binder. Luminescent coating measurement techniques are a relatively new technology for quantitative temperature measurement. The fluorescent, or sensor, molecules undergo a luminescent transition when excited with light of proper wavelength, described in by quantum levels in the Jablonski diagram (Figure 4-1). The reaction is temperature sensitive. The image of a TSP coated model surface can be captured with a scientific grade camera and then processed to obtain full field temperature distributions with very high reliability. The preparation time of the technique is short, allowing multiple configurations to be easily tested. The measurement system offers an economic alternative to conventional testing methods using large number of thermocouples. Uni-Coat TSP, purchased from ISSI Inc., was calibrated to high accuracy, using calibrated thermocouples. The calibration uncertainty of TSP was found to be ±0.93 °C over temperature ranges of 22 to 90 °C in previous studies (Liu, 2006). Light of the proper wavelength is directed at the painted model to excite the luminescent molecules. The sensor molecules become excited to an

elevated energy state. The molecules undergo transition back to the ground state by several mechanisms. For these paints the predominant mechanism is radiative decay (luminescence). Sensor molecules emit luminescent light of a longer wavelength than that of the excitation light, as some of the absorbed energy is dissipated into the surroundings. Proper filters can separate excitation light and luminescent emission light and the intensity of the luminescent light can be determined using a photo detector. The excited energy state can also be deactivated through a quenching processes; the probability of which is increased with increases in temperature (in the case of TSP). Through this important photo-physical process known as thermal-quenching, the luminescent intensity of the paint emission is inversely proportional to local temperature. One is then able, through careful calibration, to determine pixle by pixle temperatures through conversions of the recorded intensity distributions. A detailed analysis and description of TSP and PSP technologies has been presented by Liu (2006). AlFigure 4-1: Jablonski energy level diagram (adapted from Bell, 2001) though the process for any luminophore is described in Figure 4-1, the processes most probable in a temperature sensitive paint mixture are highlighted, with the major process being the excitation to energy level S1, and relaxation to the ground state S0.
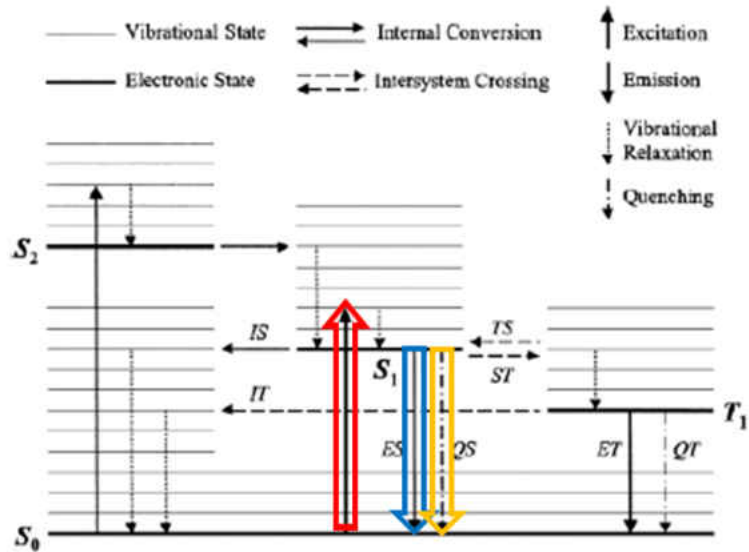
Figure 4-1: Jablonski energy level diagram (adapted from Bell, 2001)

The measurement process involves, after proper calibration, capturing a reference image at a known temperature. Typically 4 successive images are taken and averaged to reduce camera noise. One is then left with a map of known emitted intensities at a known temperature. Next intensities are captured during test conditions; yielding known intensities at an unknown temperature. Calibration curves are constructed in the form of intensity ratio (unknown intensity to reference intensity) versus temperature ratios (unknown temperature normalized by a reference temperature). With the captured reference image and temperature, and data image, one is able to back out local temperature values through simple post processing techniques. Reducing the data in this ratio fashion allows a significant reduction in testing complexity by eliminating errors due to variations in surface and lighting conditions.

CHAPTER 5   CFD ANALYSIS

5.1   Introduction

Although experiments are necessary to obtain an accurate understanding of these channels, there are some aspects of the flow that cannot be easily captured without the use of some numerical techniques. A simple CFD model, although not yielding accurate quantitative results, can give an important insight into the reasoning in the heat transfer distributions. For example, much of the discussion on the side wall performance is based off the assumption that the developed wall jet impacts this surface. However, this is only conjecture until one can actually visualize the flows with CFD. As discussed in the literature review, current numerical techniques do not accurately predict heat transfer characteristics for impingement channels. This is especially true at the locations of impingement, where CFD software over predicts heat transfer values. Nevertheless, flow patterns and features are captured quite well (El-Gabry, 2005). For the current study case 5.4.3B was chosen to be modeled and analyzed using these numerical techniques. This should give a better understanding of how the flow behaves within the channel, especially in locations where we are uncertain of the performance. This numerical analysis, merely intended as support for the experimental data, will allow a thorough description of the heat transfer and fluid results that are found experimentally. As the CFD results are only presented as a means of further understanding the physics of the flow, the scales have been removed so that one is forced to focus on the physics described.

5.2   Computational Domain & Modeling

The computational domain is intended to accurately represent case 5.4.3B, including the plenum and exit into the atmosphere. As is done in the literature (El-Gabry, 2005) the domain is divided in the streamwise direction, along the center plane. This is possible due to the symmetry of the problem, and allows for a reduction in necessary resources. All meshing was carried out in Gambit, after importing geometries created in Pro/Engineer. An image of the mesh is shown in Figure 5-1
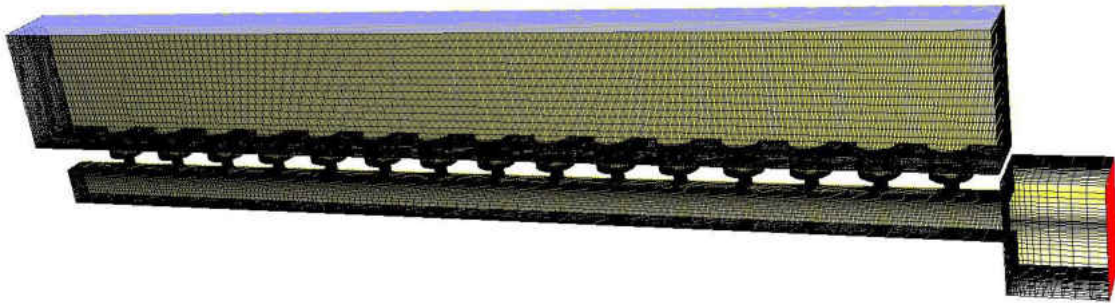
Figure 5-1: CFD Mesh (5.4.3B)

The plenum and exit were meshed with a coarser mesh than the test section and jet holes. The plenum was sufficiently sized so that a uniform velocity approached the jet holes. Meshes were densest at the test section walls, and coarser in the middle. Near the wall, y+ values near 10 were used, although for acceptable heat transfer results, y+ near 1 are necessary. Mesh independence and refinement studies are intended for future work. The computational domain was constructed from hexagonal elements, in order to achieve adequate mesh control and scaling capabilities.

A paved mesh was required to transition the mesh from the circular impingement jet to the rectangular channel. The details of this transition are highlighted in Figure 5-2.
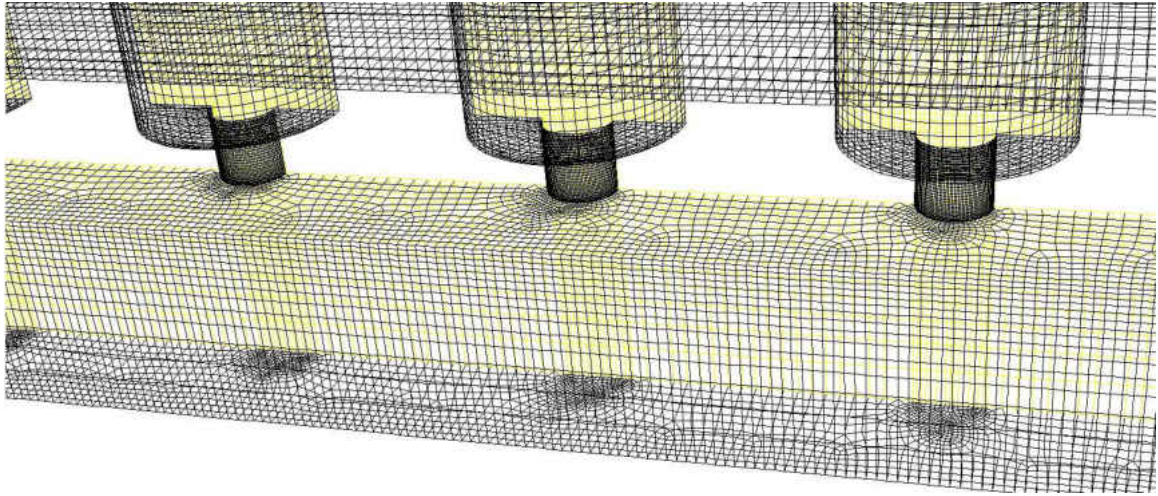
Figure 5-2: CFD Mesh Details (5.4.3B)

5.3   Numerical Model & Boundary Conditions

Commercial software (Fluent) was used to solve this complex 3D turbulent model, using a finite volume discretization method. A realizable k-ε turbulence model, using the SIMPLE algorithm was used; using enhanced wall functions. This model was used considering the results of El-Gabry (2005), where these conditions provided the most accurate results for a similar case. However, in the literature, no side wall was present, as both side boundaries were set up as periodic. Initialization procedures involved initializing the plenum with a measured pressure and velocity, and the test section with an average measured pressure and velocity. Convergence was then restricted to 10^{-6} on energy and continuity, and 10^{-3} for all other variables.

Boundary conditions were set up such that the model represented as accurately as possible the testing conditions measured during the experimental case. Boundary values were set equal to measured pressures, temperatures, and velocities. Heat flux values at

59

the wall were also set equal to those imposed during testing. These boundary conditions and their set values are shown in Figure 5-3.

Mass Flow Inlet (.037 kg/s @ 111.7kPa)

Heat Flux from Walls (10000 W/m²K)

Pressure Outlet (101kPa)
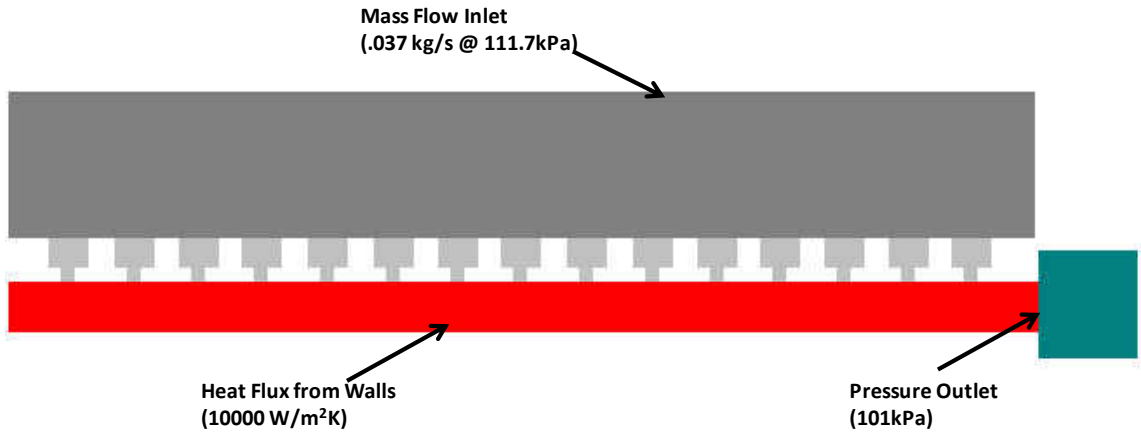
Figure 5-3: CFD Boundary Conditions

Turbulence intensities at the entrance and exit were set at 10%. Adjustments were made to this value with insignificant effects on the results. This is expected, as the experimental results (Hoogendoorn, 1977) show these effects are small. All computations were run on the UCF MMAE Biot server, typically taking 4 hours to converge at 1600 iterations.

5.4   Flow Field Results

As is typical with numerical results, convergence was achieved for the fluid section much more rapidly than for the energy criteria. This is expected, as the addition of the energy equation introduced additional complexities to the solution. The solution was allowed to run initially without the energy equation activated, as to provide for quicker convergence.

Before examining detailed flow field results, a comparison of the pressure ratio distribution and jet mass flux distributions were made, between the numerical and

experimental results. Agreement here would give ample confidence in our fluid results, as is necessary when considering numerical results. This comparison is shown in Figure 5-4 and Figure 5-5.
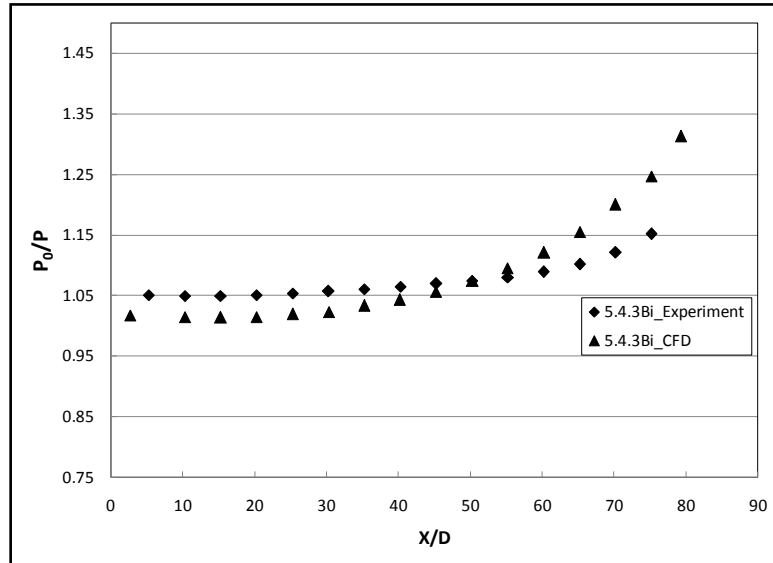
Figure 5-4: CFD Pressure Ratio Comparison

From a comparison of calculated and measured pressure ratios, we see a slight difference between the two, with maximum differences still within experimental uncertainty. Also, the CFD results cross through experimental results, around the half of the channel length.
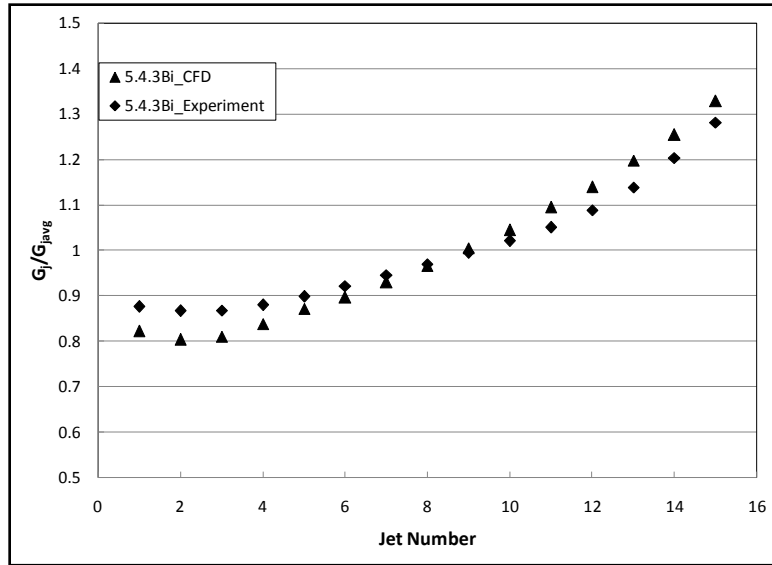
Figure 5-5: Normalized Mass Flux Comparison

As the pressure ratio is the driving force behind the jet velocity distribution, we expect similar agreement. Again the results cross around the middle of the channel, with agreement along the remainder of the channel within experimental uncertainty. The experimental trend is also represented well, except around jets 2-3, where the initial decrease in jet velocity is exaggerated in the numerical results. Examination of the flow results will provide insight into the heat transfer behaviors.

A static pressure distribution along the channel symmetry plane is shown in Figure 5-6. From this plot several details are exposed. As determined experimentally, the static pressure within the channel is uniform in the spanwise direction, except for some small regions around the jet entrance. There is also some evidence of jet deflection from this plot.
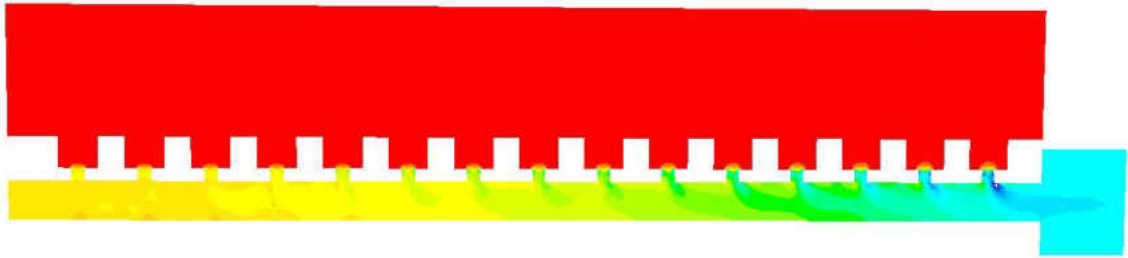
Figure 5-6: Symmetry Plane Static Pressure Distribution

A distribution of the total pressure contours will give some insight into the heat removal capabilities of the various jets. As the cross flow develops the jet potential core is no longer able to impact the surface; due to deflection and mixing with the mainstream flow. The arrival velocity of the flow, and thus its ability to remove heat, is reduced. This is an effect of the viscous effects deteriorating the jet before the potential core can impact the target surface. Figure 5-7 shows these results. Once again, there is some evidence toward the jets being deflected by the cross flow in the downstream regions, as was hinted at during the experimental results. It is also obvious now that the first few jets are able to successfully impact the target surface, as the total pressure from the plenum extends all the way to the surface. This suggests that these first few jets are not degraded from the viscous effects of the cross flow. Comparing these to the downstream jets, we see their impact is significantly reduced from these viscous effects.
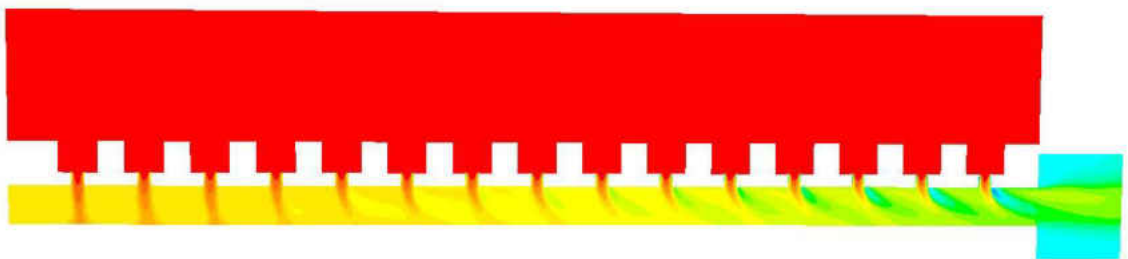
Figure 5-7: Symmetry Plane Total Pressure Contours

These pressure contours help clarify the jet flow characteristics, and the reason for the degradation of the jet performance in the downstream direction. Examination of the velocity contours should further contribute to this.
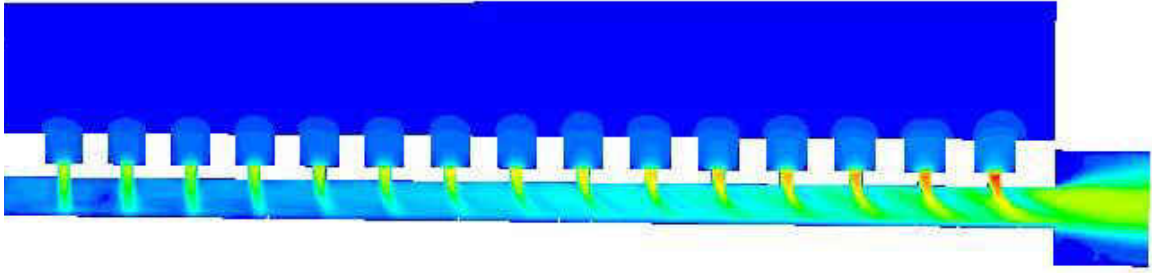
Figure 5-8: Symmetry Plane Velocity Magnitude Contours

As shown in the averaged results, the jet velocity distribution matches experimental results quite well. From Figure 5-8 we see a slight increase in the jet velocity in the downstream direction, due to the increased pressure ratios. The cross flow velocities also continuously increase in the downstream direction, as is required by the mass conservation. This cross flow also tends to deflect the last few jets, keeping the maximum velocities in this region from impacting the target surface. It is evident there is an obvious transition from an impingement dominated flow to one that is predominantly controlled by the cross flow, as the last few jets do not contribute to the heat transfer through impingement. Their contribution, however, is through the introduction of additional turbulence and kinetic energy, as is shown in Figure 5-9 and Figure 5-10. The results also validate our plenum design, as velocities in this region are negligible.
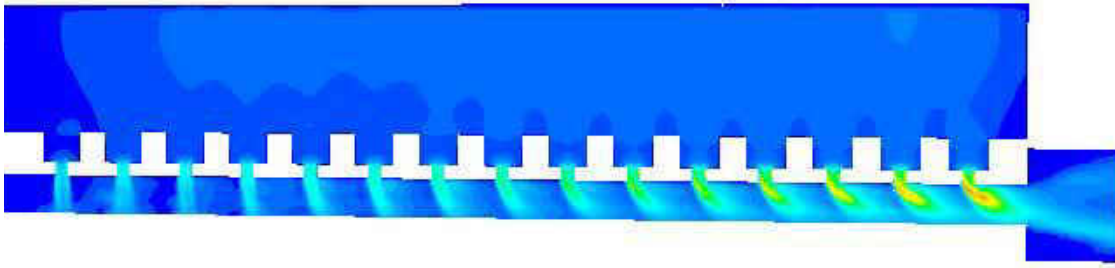
Figure 5-9: Symmetry Plane Turbulent Kinetic Energy

As increased kinetic energy means increased velocities, neglecting density changes, increases in this magnitude should result in increased heat transfer contributions. As alluded to previously, the last few jets still aid in augmenting heat transfer through the addition of turbulence and kinetic energy.
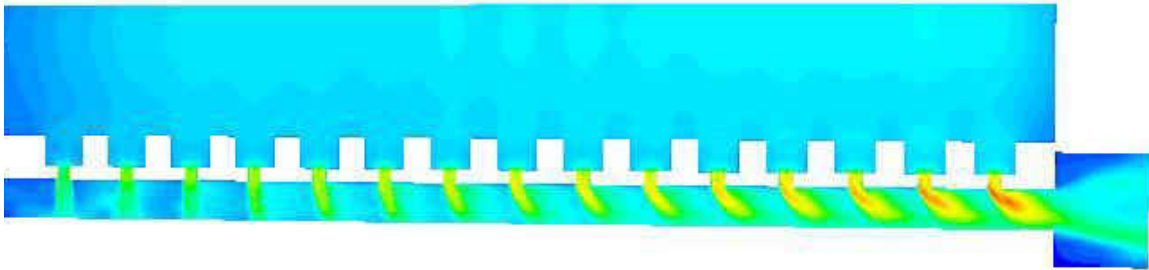
Figure 5-10: Symmetry Plane Turbulence Intensity (%)

Similar effects are seen in Figure 5-10, where the turbulence intensity of the last few jets is greater than the upstream jets. This tends to increase the turbulence through the span of the channel in this region, leading to relatively high levels of heat transfer, without successful impingement. Through examination of the velocity vectors, further details into the flow should be revealed.
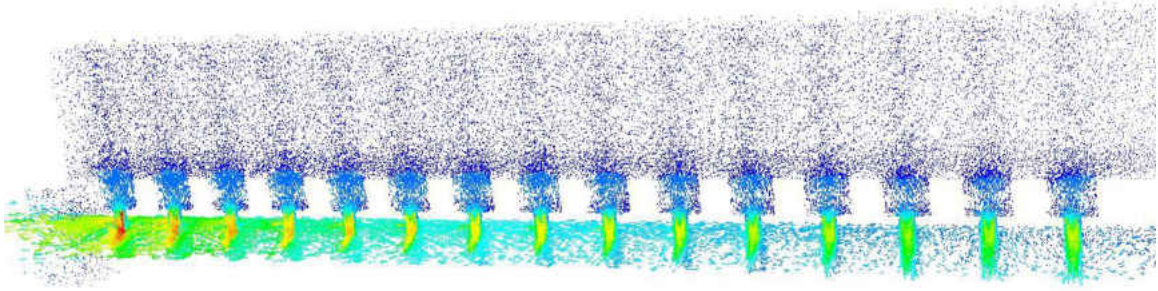
Figure 5-11: Impingement Channel Velocity Vectors

From Figure 5-11, similar to the previous plots, we see the large difference in magnitudes between the impingement velocity and the channel flow velocity. Also as discussed previously, the increase in channel flow tends to deflect the downstream jets. The quality of the plenum design is also confirmed, as the velocity is low and uniform throughout. A close up of various regions should provide further insight, with the first few jets shown in Figure 5-12.
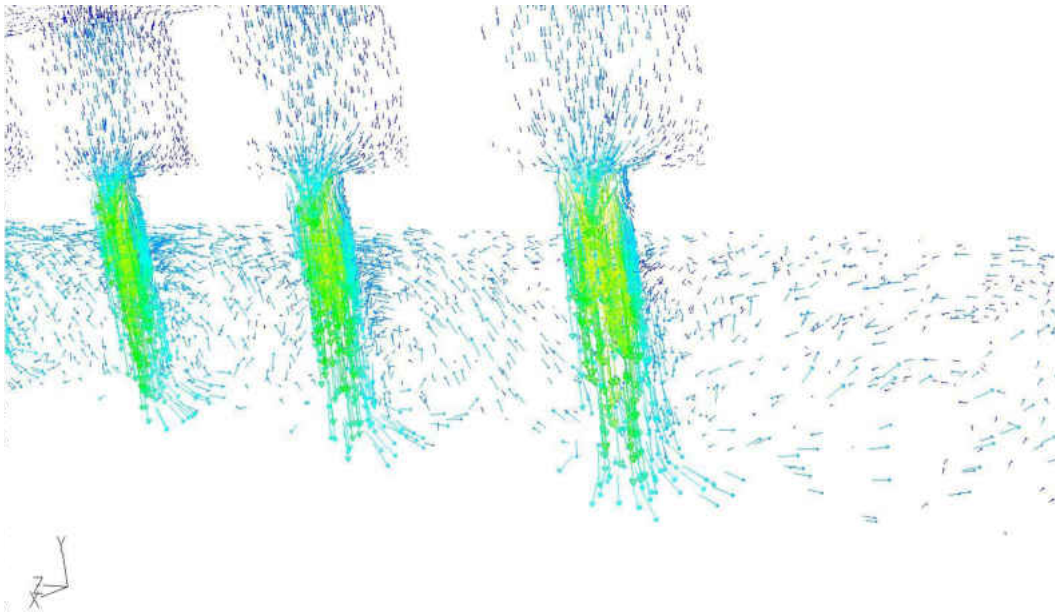
Figure 5-12: Velocity Vectors: Jets 1-3

From this view, the development of the wall jet, as hinted at earlier, is now very clear. The region before the first hole is also interesting, as we see how the flow circulates here, most likely picking up a great deal of heat. Local heat transfer plots from experimental results, also showed very low heat transfer coefficients in this region (consider case 15.4.3 for example). Recirculation is also visible in the spanwise direction, which results after the wall jet has collided with the side wall. This should help promote heat transfer on these surfaces. This recirculation, however, should be very sensitive to effects from cross flow, as we will see in later results. Figure 5-13 shows another view of this recirculation.
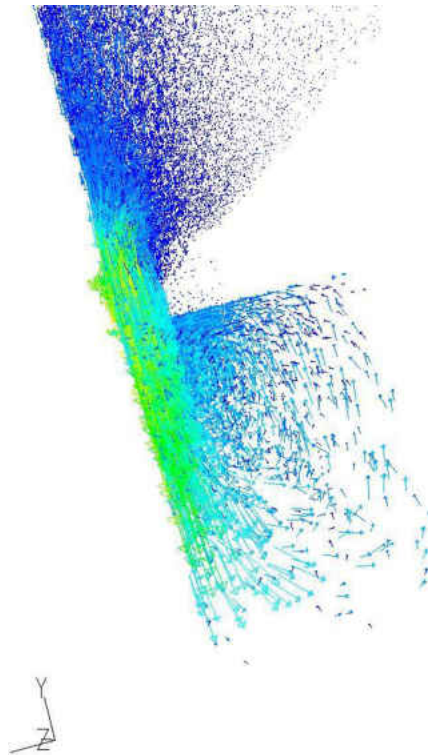
Figure 5-13: Velocity Vectors: Upstream Circulation

Here the degradation of this spanwise circulation is clearly visible. Around the upstream jets the wall jet is able to impinge the side wall and circulate back toward the jet. However, as the cross flow becomes significant, this circulation is prevented, and the flow is predominantly directed in the downstream.
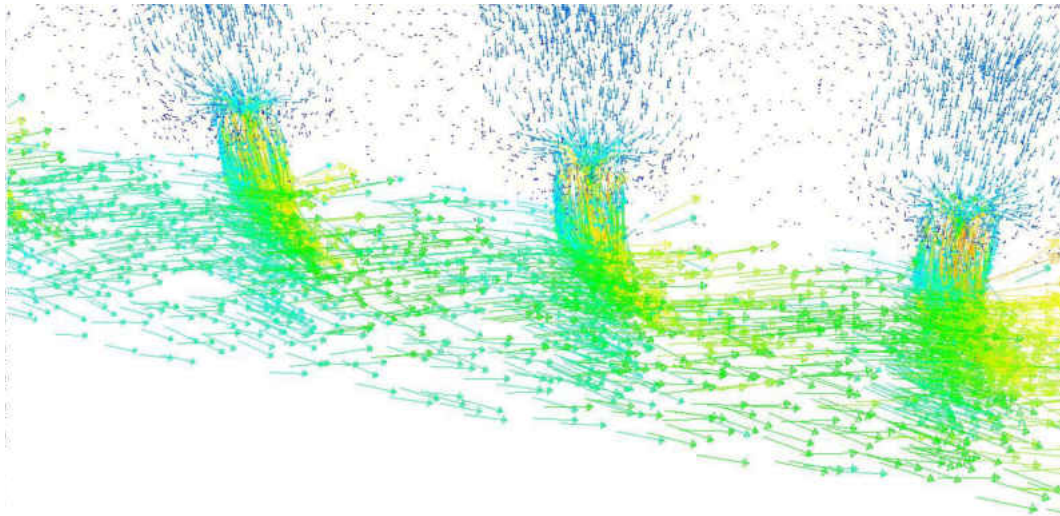
Figure 5-14: Velocity Vectors: Jets 12-14

The deflection of the wall jets by the cross flow is clearly shown in Figure 5-14. At these last few jets, there is no real wall jet formed in the spanwise direction. The jets are not able to impinge the surface directly, because the cross flow momentum is great enough to deflect the jets significantly. However, although the wall jets no longer are able to contribute to the heat transfer on the side walls, the high cross flow velocities do, as will be evident in the results.

Numerical analysis also allows a non-intrusive calculation of the air temperatures within the channel, allowing comparisons against discussions regarding bulk temperature models. This distribution is shown in Figure 5-15.
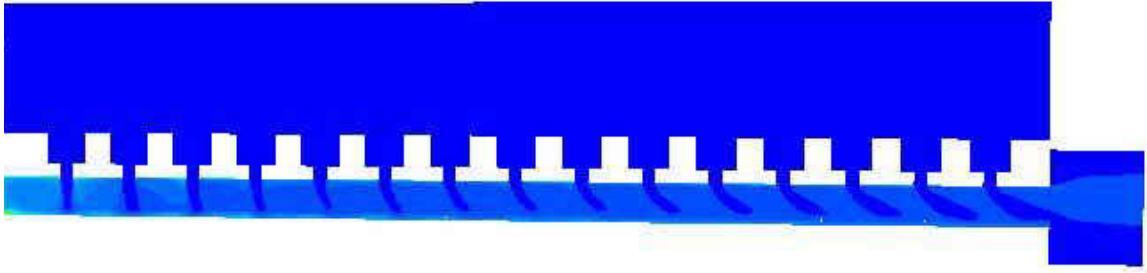
Figure 5-15: Air Temperature Distribution

As is assumed in the literature, for the majority of the channel, the jet temperature is the driving temperature, especially in the upstream stagnation regions. However, there is evidence of bulk flow heat pick up. This is especially true in the region upstream of the first jet, where the lowest heat transfer coefficients were typically seen using a jet reference temperature. It is obvious from this plot that the presented models give crucial insight into the behavior of the bulk flow temperature, and describes the importance of understanding and predicting this behavior.

5.5   Heat Transfer Results

As mentioned, current numerical methods are not able to accurately predict the heat transfer performance of an impingement channel cooling scheme (El-Gabry, 2005). However, the overall trends are accepted, and still are able to give insight into the flow. An overview of the channel performance is shown in Figure 5-16. In order to maintain uniformity between numerical and experimental calculations, a custom field function was created in Fluent to calculate heat transfer coefficients. This definition is identical to that used in the experimental sections.

69
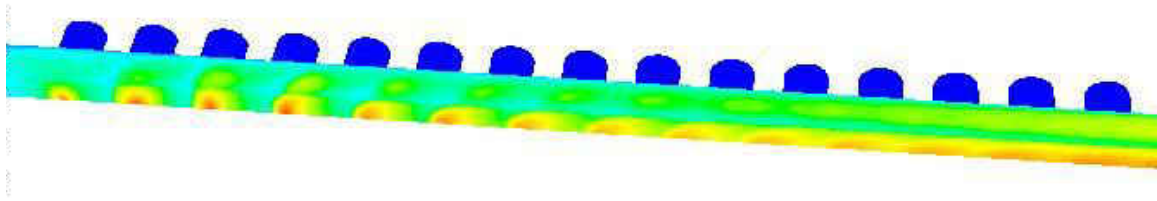
Figure 5-16: Heat Transfer Coefficient Distribution

From initial observations one notices the upstream jets successfully impinge the target surface, and are soon dominated by the cross flow. Wall jet impingement is also visible on the side wall in the upstream regions, and again tends to be overcome by the cross flow accumulation in the downstream regions. In the downstream region, increased heat transfer levels near the center of the channel are evident. The poor performance before the first jet is also evident, as was alluded to in the preceding section. A closer examination of these profiles is shown in Figure 5-17 and Figure 5-18.
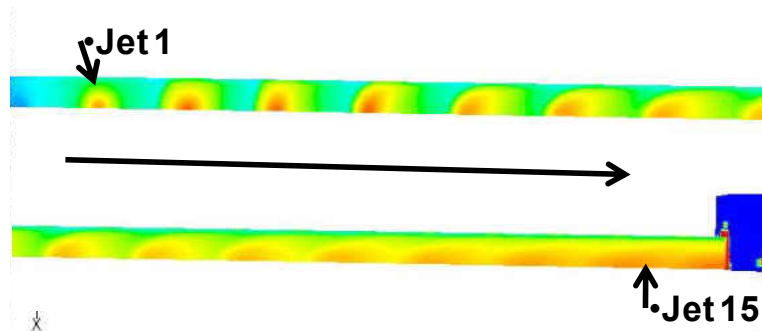
Figure 5-17: Target wall heat transfer coefficient contours

The deflection of the stagnation point is clearly visible in these images, as well as the additional benefit of the last few jets in the downstream regions. There is an obvious transition from a region purely dominated by impingement effects, to one that has competing cross flow effects as well.
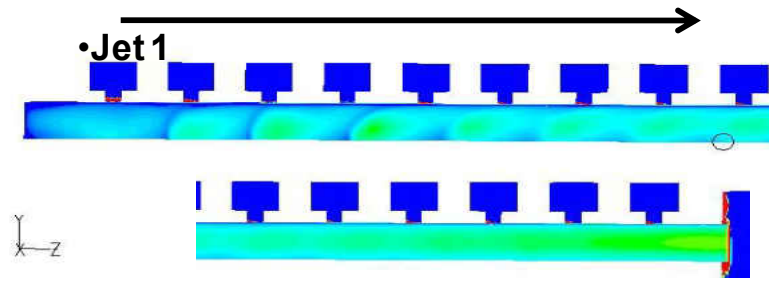
Figure 5-18: Side wall heat transfer coefficient contours

The transition from impingement dominated flow to a competing flow is evident on the side wall as well. As is expected with cross flows of high velocities, the last few jets experience high heat transfer coefficients across the span of the wall. This is a more uniform distribution than is seem upstream where the jet effects are dominating. With a thorough understanding of the behavior of the flow, a clear analysis of the experimental results is possible.

CHAPTER 6   **FLUID ANALYSIS**

6.1   Introduction

Before one is able to fully understand the heat transfer behavior of these cooling schemes, it is necessary to have some insight into the way the flow behaves within the channel. This not only involves understanding how the flow rate is distributed across the array, but also how much pressure head is required to push the flow through the channel. With this information, it should be possible to make some conjectures into why the heat transfer distributions behave as they do.

6.2   Discharge Coefficient

As mentioned earlier, discharge coefficients measured during the first round of testing were applied to the second test rig, and adjusted slightly so that calculated mass flow rates were equal to measured values. As stated in the literature (Florshuetz, 1983 for example), this value is expected to remain nearly constant over the pressure ratios, jet Reynolds numbers, and cross flow to jet mass flux ratios of interest to gas turbine applications. The discharge coefficient results are shown below in Figure 6-1.
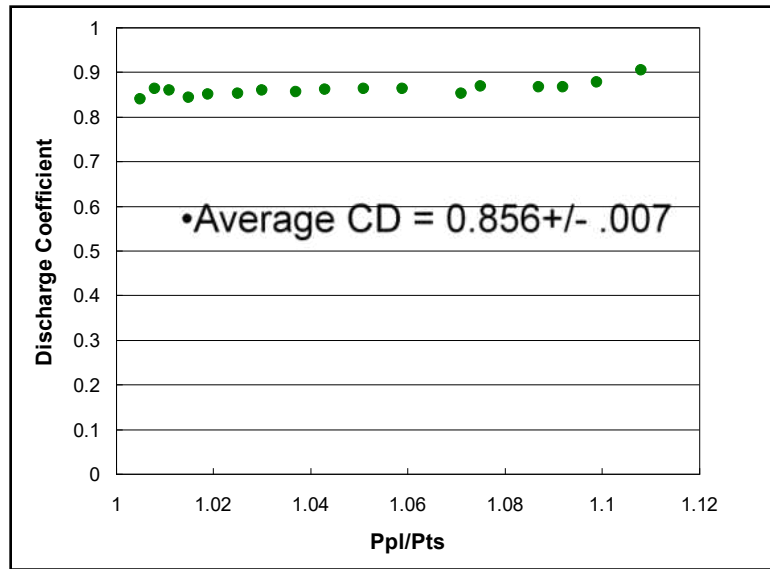
Figure 6-1: Jet Plate Discharge Coefficient

The C_D trend was nearly constant between the tested pressure ratio values of 1.008 and 1.108. The average value was calculated to be 0.857 (+/- .007). A constant C_D is necessary in order to accurately use the model developed by Florschuetz (1981). The fact that the discharge coefficient is constant over this range of pressure ratios is expected, as this trend is seen in the literature. Effects of cross flow should be negligible on the discharge coefficient, unless the mass flux ratios of the cross flow to jet (G_c/G_j) approaches unity (Florschuetz, 1983). The presence of the walls, the target as well as the side walls, leads to concern of potential effects on the discharge coefficient. The added effects of cross flow only increase this concern. However, the work performed by Florschuetz, suggests that cross flow and channel height effects will have no effect on the discharge coefficient when the channel height was larger than 1 diameter, or the cross flow to jet mass flow ratio did not exceed some critical value. Beyond this critical value at small channel heights, the discharge coefficient tends to decrease slowly, until the mass flux ratio exceeds unity. Beyond this point the discharge coefficient cannot be

assumed to be unaffected by the cross flow. Minimal effects from this were only seen for Case 5.4.1 of this study, and have thus been neglected. Regarding the side wall presence, consistency between calculated mass flow rates and those measured by the flow meter confirmed our choice of discharge coefficient.

6.3   Flow Distribution

As previously mentioned, pressure tests were conducted to find the pressure distribution throughout the test section. Along with the discharge coefficient and channel parameters, it was then able to determine the jet and cross flow distribution within the channel.

6.3.1   X/D 5 Flow Results

For the X/D of 5 cases, pressure data was gathered for both the right wall and target wall, and it was observed that the pressure distributions were nearly equal, as has been observed in existing literature (Florschuetz, 1980). Figure 6-2 shows the pressure ratio profiles obtained for each case with an X/D equal to 5 hole diameters.

The pressure profiles for cases 5.4.1 and 5.4.3A were similar until 60 X/D where the case 5.4.1 pressure ratios climb higher and the Case 5.4.3A data remains nearly linear. The two cases had similar Reynolds numbers at ~17,000 which corresponds to where the two curves are very close together and linear. The pressure ratio values of Case 5.4.1, which has the smallest Z/D of 1, begin to increase at 55 X/D. This is due to the fact that as X/D increases, the amount of cross flow increases in a non-linear matter. The channel height is so small that the cross flow accelerates more than any other case,

and there is a very large pressure drop for the downstream jets. In contrast, Case 5.4.3A remains nearly linear even at the last few jets, due to the larger Z/D of 3.
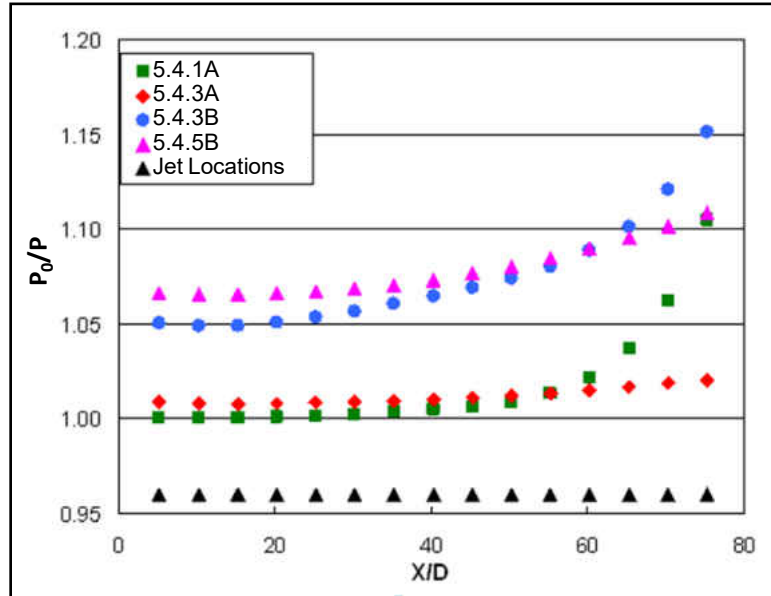
Figure 6-2: Pressure Ratio Profiles

The pressure ratio for cases 5.4.3B and 5.4.5B are similar, which, as mentioned above, is related to their common Reynolds number of 43,000. Their difference in geometry becomes evident at the last few jets, again, with Case 5.4.3B having the greatest pressure ratio at the end of the channel and also a lower Z/D of 3 as compared to Case 5.4.5 which has a Z/D of 5.

For Case 5.4.1, the pressure drop across the channel was so great that due to structural limitations of the rig, the high Reynolds number case could not be run for that configuration. The maximum channel Mach number was nearly considered compressible, at 0.18, with a Reynolds number of 17K for Case 5.4.1.

The ratio of the jet mass flux and average jet mass flux, G_j/G_{javg}, was calculated using the obtained C_D values and the one dimensional model developed in Florschuetz

(1981). This model was then compared to the measured G_j/G_{javg}, based on measurements

made in the pressure profiling test and the C_D test and shown in Figure 6-3.
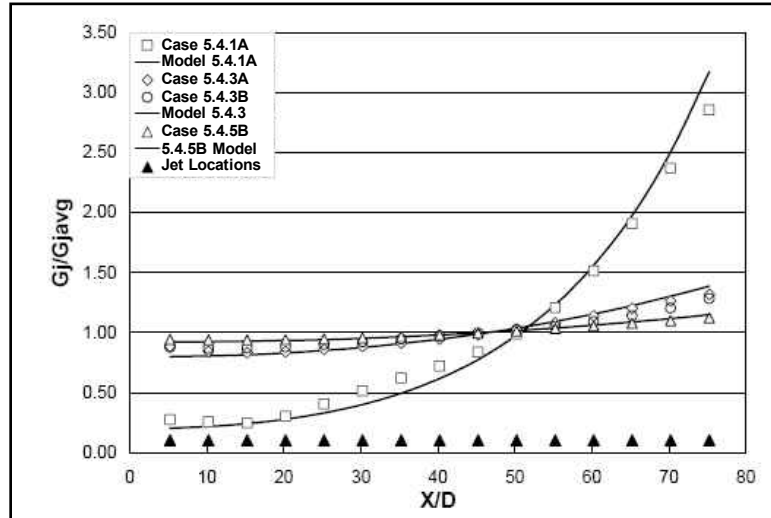
Figure 6-3: Jet Mass Flux Distributions

Figure 6-3 shows that Case 5.4.3A, 5B, and 6 are nearly linear and very similar in

their G_j/G_{javg} values. These cases fall closely to the model developed by Florschuetz.

These cases also resemble the ones shown by Florschuetz that have similar geometrical

parameters. The cases also have a similar pressure profile, which is also mostly linear.

This suggests that there is little interaction between the jets in the spanwise direction, as

only 1 row was tested in the current study.

Case 5.4.1, as mentioned earlier, has the smallest Z/D value, and thus has the

greatest acceleration of cross flow, which can be seen in the pressure ratio plot and the

G_j/G_{javg} plot. In both cases, the curve follows a more exponential trend. Florschuetz also

notes this for their smallest Z/D case, also equal to 1, which exhibits a similar behavior.

Next, an estimated ratio of cross flow mass flux to jet mass flux (G_c/G_j) was

found using another equation developed in the model by Florschuetz. Cross flow mass

fluxes (G_c) were calculated from the collected experimental data. G_c/G_j values determined experimentally plotted against the models developed by Florschuetz, shown in Figure 6-4.
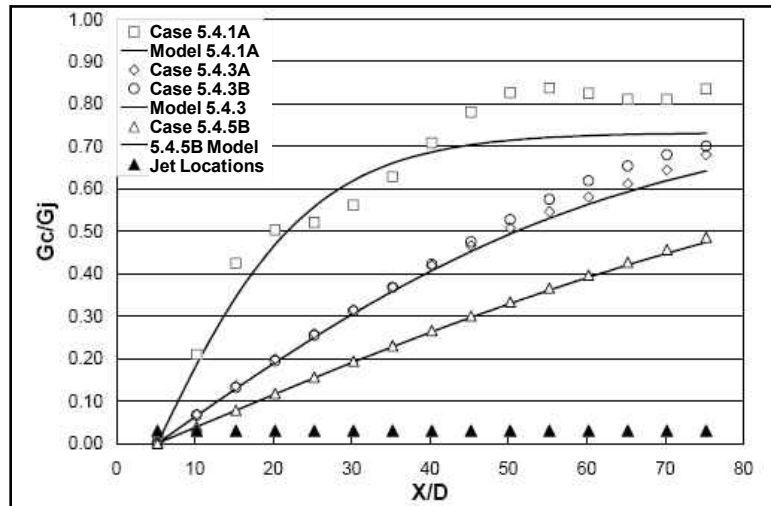
Figure 6-4: Normalized Cross flow Mass Flux Distribution

Figure 6-4 shows that cases 5.4.3A, 5.4.3B, and 5.4.5B follow a nearly linear trend that increases as X/D increases. This follows the G_j/G_{javg} data, which is also nearly linear. Case 5.4.1, as in Florschuetz (1981) has a non-linear trend. At low X/D values, G_c/G_j increases sharply until X/D of 35 where it flattens out at ~0.85. The experimental data does not follow the model as well as in the other three cases. This was also true in Florschuetz's data for cases with Z/D of 1. However, in the case of this paper, Case 5.4.1, the data deviates much more. This is a result of a combination of cross flow acceleration and the flow nearly reaching compressibility. Florschuetz et. al.(1983) did a follow up study on the effects of cross flow on C_D. Their work found that at G_c/G_j values near and above unity, C_D actually starts to decrease. This discrepancy is most likely the largest contributor to the variations in Figure 6-4. This deviation, however, will not be

explored further, as it does not change the results significantly, and the overall trend is still apparent.

Because of the development of cross flow, the channel pressure decreases with an increase in velocity within the channel. This negative pressure gradient is required to push the exhausted jet flow out of the channel. As the plenum pressure is held constant, a variation in pressure ratios then exists, which results in a variation in the jet and channel Reynolds number in the downstream direction. The jet mass flow distribution and cross flow development balance each other within the channel. This characteristic is captured in the previous figures, but can also be represented in the form of Reynolds number distribution along the channel for both the jet and channel, shown in Figure 6-5. The channel and jet Reynolds numbers are defined by their respective diameters, and the channel Reynolds number is that which exists up to the particular jet. This plot will aid in explaining thermal performance of each channel, as the Reynolds number is used for baseline comparisons.
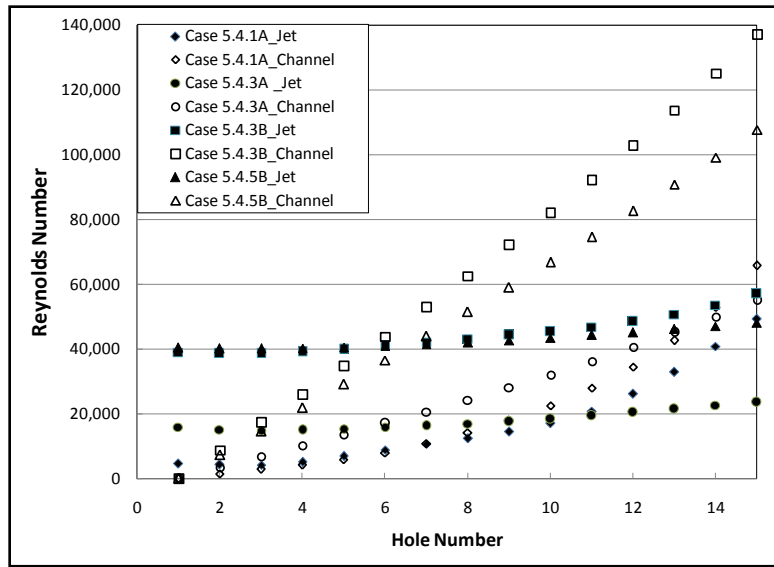
Figure 6-5: Reynolds number distribution (X/D=5)

6.3.2 X/D 15 Flow Results

Similar tests were carried out for the cases with a 15 diameter jet to jet spacing. Due to experience from earlier tests, results were expected to match those presented in the literature, regardless of the presence of the side walls Figure 6-6, shows the pressure ratio profiles for each of these cases.

79
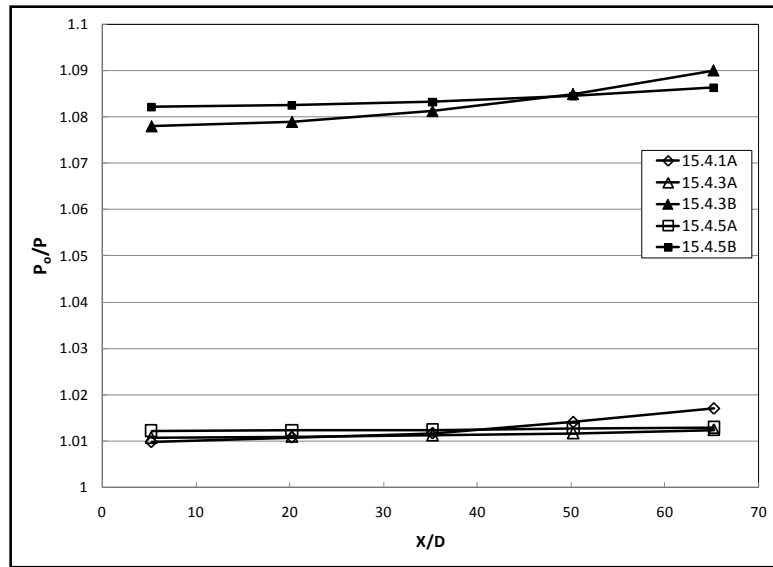
Figure 6-6: Pressure Ratio Distribution (X/D=15)

The distributions are much more consistent for these cases, simply due to the fact that the amount of mass input into the main channel is only one third of the previous case. Considering only the effects of the main channel, one expects a lower channel pressure drop (and thus less variation is pressure ratio) for a lower mass flow and velocity. Nevertheless, we see that the tallest channels yield the most consistent distributions, while the smaller channel height has more variation in the downstream direction due to the acceleration and velocity of the fluid.
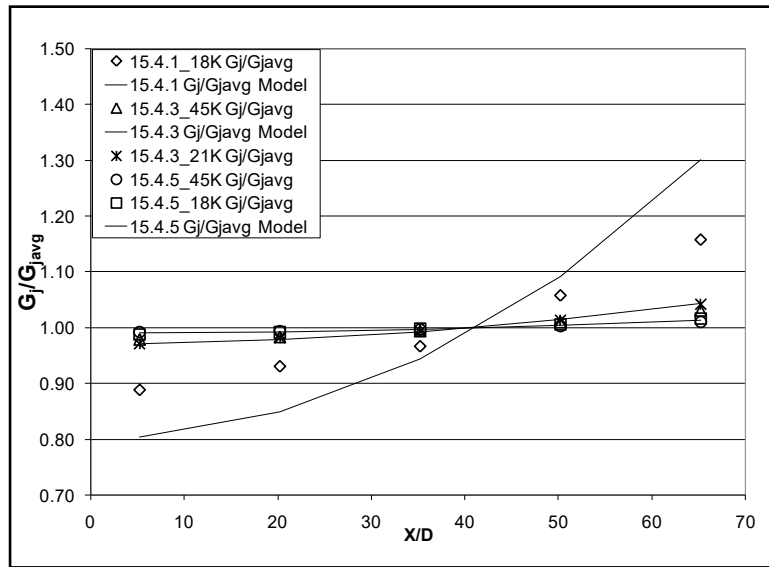
Figure 6-7: Jet Mass Flux Distribution (X/D=15)

Once again, in order to get a sense of how the flow is distributed amongst the jets, Figure 6-7 shows the jet mass flux distribution, normalized by the average jet mass flux. Similar to before, we see the effect of the decreasing channel height is to create a more non-uniform jet distribution. Similar physics lead to this effect, most importantly the larger increase in cross flow velocity in the downstream direction leads to the larger variation in channel pressure in the downstream direction. With the larger channel heights, the ingested mass flow does not lead to high velocity cross flows because of the large cross sectional area in the channel. At the extreme heights, the cross flow velocities are low enough to create a minimal variation of channel pressure.
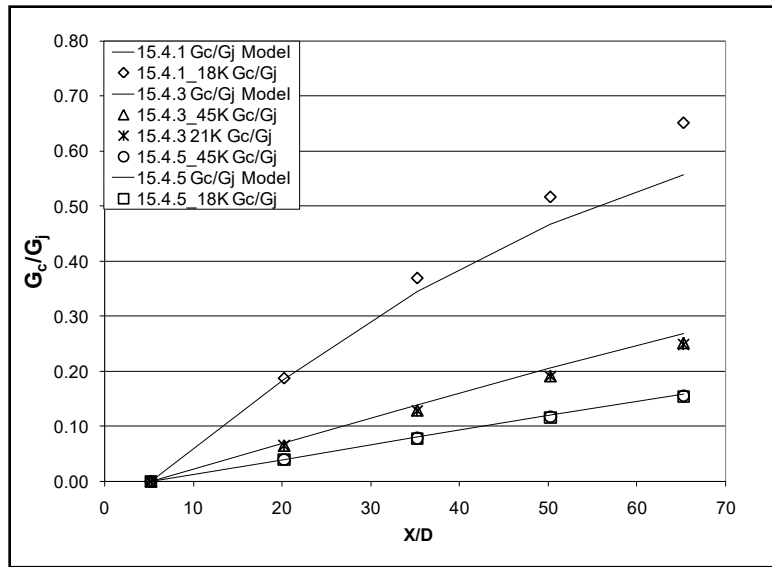
Figure 6-8: Normalized Mass Flux Distribution (X/D=15)

The non-linearity of the jet mass flux distribution is once again expected to show up in the cross flow mass flux distribution (normalized by the local jet mass flux). These results are shown in Figure 6-8. As expected, the smallest channel height yields the largest variations in cross flow mass flux (and thus velocity). As expressed earlier, this is necessary in order to maintain continuity in the small channel, while mass is being periodically ingested. Minimal variations in cross flow are seen as the channel height is increased, as the velocities in these channels are not required to be as high.
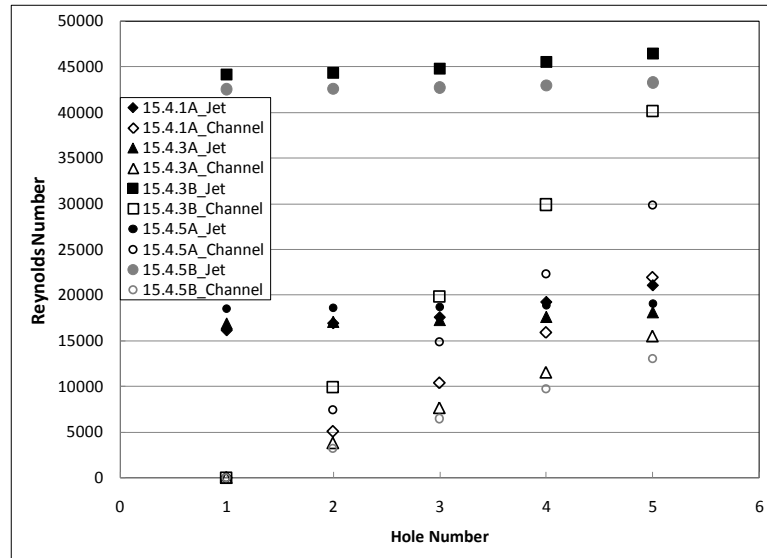
Figure 6-9: Reynolds Number Distribution (X/D=15)

Figure 6-9 presents the flow distribution in terms of Reynolds number distributions, both being defined based on their corresponding hydraulic diameters, up to the listed hole. Immediately one should notice that the channel Reynolds numbers are not as high for the current cases, as is expected due to the lowered total mass flow rate. The Reynolds numbers within the channel are consistently lower than the impingement Reynolds numbers, again suggesting minimal effects due to cross flow for the cases with X/D=15.

6.4   Friction Factor

As discussed earlier, a friction factor was computed for each channel, and compared to the smooth channel estimate, calculated at the highest channel Reynolds number. The results should give some insight into losses associated with each channel configuration for comparisons with other methods of cooling.

83

6.4.1   X/D 5 Friction Factor

The normalized friction factor for the cases with a 5 diameter jet spacing is plotted in Figure 6-10. We can see from this plot, that as the cases progress, the friction augmentation is increased. Several factors contribute to this, including the definition itself. It is interesting to note that although Case 5.4.1 shows a friction factor that is less than the smooth channel prediction, the largest pressure ratios were required to achieve this flow rate. This is a direct result of the flow distribution within the channel. The cross flow develops most rapidly, with some of the largest velocities overall, near the channels exit. As the calculated friction factor is normalized by the predicted value at this location of maximum velocity, the augmentation is less than unity. However, with the remaining cases, the cross flow distribution is much more uniform, as shown previously, resulting in less drastic variations in velocity. The cross flow within the channel for Case 5.4.5, for example, increases linearly, so that the pressure drop along the channel consistently increases. However, as the channel height is reduced, the variation along the channel becomes greater, affecting the calculated friction factor along the channel. The effects of this distribution will become most apparent when considering the thermal effectiveness of the channel.
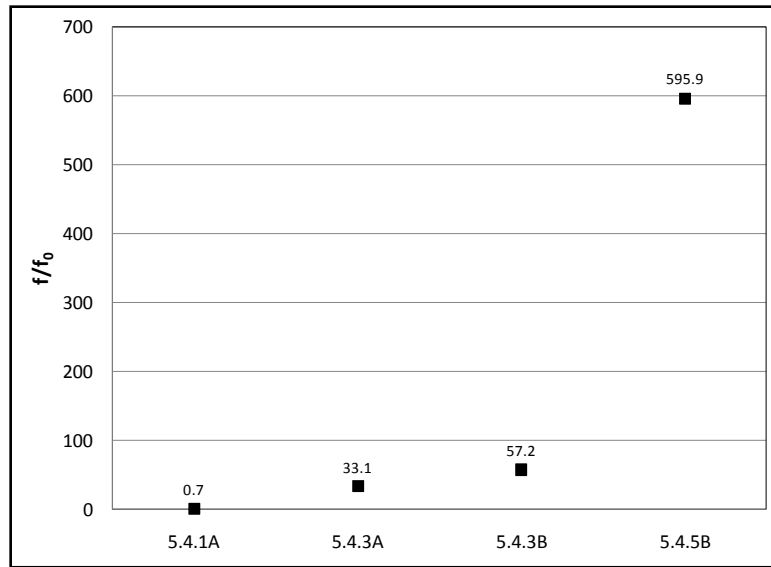
Figure 6-10: Normalized Friction Factor Distribution (X/D=5)

6.4.2 X/D 15 Friction Factor

Similar results were expected for the 15 diameter spaced jets, although the variations from case to case would be less due to the decreased amount of cross flow present in the channel. These results are presented in Figure 6-11, were we see that as the channel height, and Reynolds number are increased, the friction augmentation increases as well. As discussed previously, this is in part due to the definition, which calculated nominal values at maximum channel conditions. As the channel height is increased and channel velocity is reduced, this predicted value is also reduced. However, similar pressures are still required to drive the flow across the jet plate, yielding large augmentations.
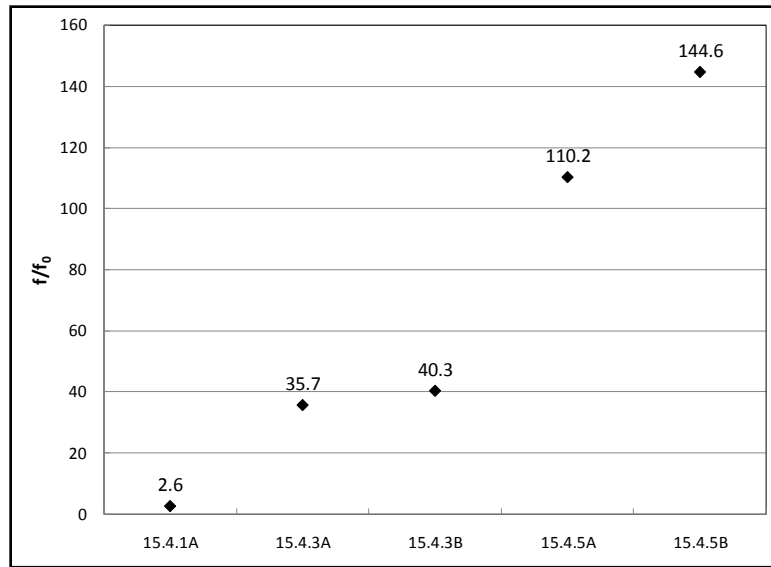
Figure 6-11: Normalized Friction Factor (X/D=15)

It is apparent, however, that changes in channel height play a larger role than changes in Reynolds numbers. This again suggests that the friction augmentation is mainly from the jet plate, and less so from the pressure drop required to drive the cross flow out of the channel. Increases in Reynolds number do, as expected, provide for additional pressure losses, especially as the channel height is increased. These representations of the pressure drop across the channel point out the fact that the cost for the resulting high heat transfer coefficients come about in the increased pressures required to drive the flow.

When considering the results discussed above, it may initially be difficult to accept an enhancement of almost 600 over smooth pipe predictions (case 5.4.5B). However, this is purely a result of the definition employed here which thus requires some further discussion. Because both our baseline friction factor, and our calculated friction factor are dependent on the flow velocity within the channel, the results are very sensitive

to both the channel height, and the amount of flow within the channel. The friction factor is then not only a function of the array geometry, but also the channel dimensions, as well as the total mass flow rate within the channel. These effects are apparent when considering the enhancements among the various cases, with the largest values being seen for the tallest channel size with the largest cross flow velocities. The length of the channel is also expected to be a dependant parameter, as both the amount of ingested flow, and the additional pressure drop required within the channel are affected by this.

6.5   Viscous Dissipation Effects

As the current experiments are carried out in the incompressible flow regime, with maximum jet Mach numbers on the order of 0.2, and with a relatively low Prandtl number working fluid, the heating effects of viscous dissipation are expected to be small. The largest effects would be expected near the last jets, where the velocity gradients would be the largest, considering the presented CFD results. The effect of viscous dissipation would be to increase the adiabatic wall temperature beyond the measured static temperatures that are used in the heat transfer coefficient calculations. This is most noticeable with high viscosity fluids, where the viscous stresses act to diminish the energy of the flow. The effects also become pronounced as the velocities become increasingly high. These effects are not typically considered in the literature, as the majority of applications are with low viscosity fluids. However there has been some work, (Li, 1997 for example), investigating the recovery factor and viscous dissipation trends for high and low viscosity fluids. The two effects are coupled, as the recovery factor is dependent on the viscous dissipation trends. It has been shown through these

works that viscous effects are greatest right outside the impingement location, and are highly dependent on the viscosity and Prandtl number of the fluid.

In order to justify neglecting these effects in the current study, the potential heat up of the fluid due to viscous effects is considered for cases 5.4.1A through 5.4.5B, considering average conditions. This is done by considering both the recovery factor effects on the adiabatic wall temperature, and the viscous heating effects resulting from the pumping power that is transferred to the flow. These results are shown in Table 6-1.

Table 6-1: Viscous Dissipation Calculations

Case	ΔT (PP)	% of measured ΔT	ΔT (re)	% of measured ΔT
5.4.1A	0.9	2.6	0.5	1.4
5.4.3A	0.3	0.9	0.6	1.8
5.4.3B	2.6	7.4	3.2	9.2
5.4.5B	2.6	7.4	3.4	9.6

As expected, especially for the lower Reynolds number cases, neglecting the potential heat up of the fluid introduce small errors. This is explained by considering the average static temperature rise due to pumping work being transferred to the fluid. This is done on a global scale, considering the average work required to pump the jets into the channel, and the resulting static temperature rise that is accompanied with the velocity increase from the plenum to the jet. We see that for the low Reynolds number cases, this results in a maximum 2.6% error in calculated temperature difference. For the high Reynolds number cases, the effects are slightly more significant, on the order of 7.4%, considering the typical measured wall to jet temperature difference of 35K.

Further confidence is established when considering the difference in temperature between the measured static temperature and the adiabatic wall temperature, using

recovery temperature calculations. Using a flat plate turbulent flow recovery factor, which is a function of Prandtl number, one is able to determine the difference in these temperatures. Again, similar trends are seen, with minimal effects seen for the lowest Reynolds numbers. Temperature differences are less than 1 degree for these cases, which is less than the standard uncertainty of the thermocouples used in these experiments. At the higher Reynolds numbers, the effects are still relatively small. This establishes further confidence in the data reduction techniques carried out in the current study.

CHAPTER 7   HEAT TRANSFER RESULTS

7.1   Introduction

Heat transfer data is presented as both local heat transfer coefficient plots, as well as spanwise averaged plots. Validation results will be presented first, followed by a discussion on the potential effects of channel flow temperature increases. The reasoning and proposed methods of channel flow temperature prediction will be given, followed by an investigation into their effects. Circumferential heat flux variations will then be investigated, in order to prove negligible effects on heat transfer results due to these variations. These results will help guide future testing procedures. A discussion on the applicability of existing correlations to the area of narrow impingement cooling will help highlight areas where the side walls are highly influential, changing the predicted heat transfer results. In order to get some sense of how channel geometries can potentially lead to thermal stresses, the uniformity of the heat transfer distributions will be discussed. Finally, with the presented data, a thermal performance factor will be calculated, so that a fair comparison between channel performances can be made. This discussion in itself is unique, since many of the comparisons made have not yet been presented in the literature.

7.2   Rig Validation

In order to assess the accuracy of our measurement techniques, it was necessary to validate our test set up. This was done, as mentioned, by creating a smooth channel scenario to be compared against some of the well accepted correlations available in the literature (Gnielinski and Dittus-Boelter (Incropera, 2002)). Both rig iterations were

validated individually, with acceptable results. Initial testing also involved ensuring all jets were performing similarly through Pitot probe traversing. Testing symmetry was also verified through the comparison between TSP measured temperatures and thermocouple measured temperatures on opposing walls.

7.2.1   Pressure Rig

Heat transfer measurement techniques were validated by setting up a pure channel flow scenario by plugging the jet holes, and introducing only cross flow into the impingement channel. An entrance section of 30 hydraulic diameters was used to allow the flow to become hydrodynamically fully developed before entering the heat transfer test section. The flow rates were measured with a low loss venturi flow meter. The calculated heat transfer results were compared against accepted pipe flow correlations (Gnielinski and Dittus-Boelter (Incropera, 2002)). Fluid bulk temperature for the validation case was assumed to increase linearly across the test section from the inlet to exit air temperatures. This was validated through energy balance considerations. Surface and spanwise averaged plots of the resulting side wall heat transfer coefficients for the validation test are seen in Figure 7-1.
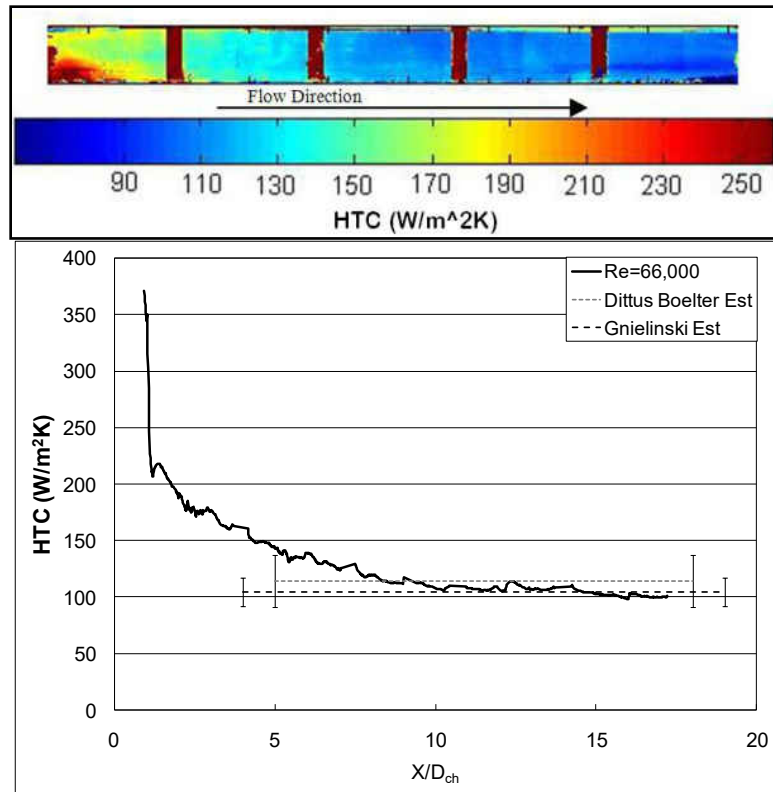
Figure 7-1: HTC Validation Results

The results give great confidence in our experimental set up, as the flow becomes fully developed around 10 diameters, and settles nicely within the uncertainty limits of the two correlations. Similar results are expected with the suction driven rig.

7.2.2   Suction Rig

Similar to the pressure driven rig, the suction rig was also validated under a smooth channel cooling scheme, set up in a similar manner. However, no entrance section was used in this section, so that the hydrodynamic and thermal boundary layers start at the same position. A small grommet was created out of clay at the entrance to reduce some of the vorticity generated at the entrance. The same correlations should hold

in the fully developed section. Again results were compared to known correlations, as is shown in Figure 7-2.
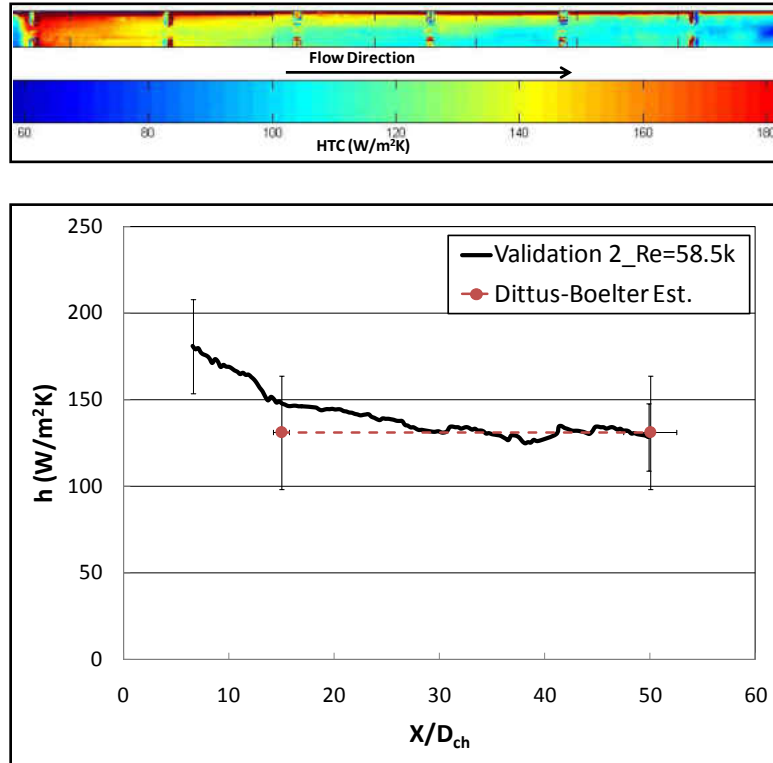
Figure 7-2: Validation 2 Results

Once again the channel behaves as expected, settling right around predicted values. The developing portion is slightly longer than for the previous case, a result of the lack of a hydrodynamically developed entrance flow. Nevertheless, these results build confidence in the remaining discussions.

7.3   Constant Reference Temperature Results

Traditionally, impingement channel heat transfer research calculates heat transfer rates using the jet temperature as the required reference temperature. This normally does not introduce any significant errors, since the high speed jets have little time to pick up

heat as they impinge the surface. The driving temperature difference is then understandably chosen as the jet to wall temperature difference. This is not only convenient, but also realistic as has been shown in the literature. The following results present data calculated in this fashion.

7.3.1   X/D 5-Constant Reference Temperature

7.3.1.1   <u>Target Wall</u>

Target wall heat transfer profiles are shown in Figure 7-3. From this local data, the effect of the accumulation of cross flow can be seen; which has been discussed in previous literature. The distinct stagnation point becomes less evident, while the overall spanwise heat transfer coefficient becomes more uniform as one moves downstream for all cases. The majority of the existing literature has studied channels with fewer impingement holes. We see from this data that for cases 5.4.1A and 5.4.3A (Figure 7-3), the cross flow velocity was great enough to produce appreciable heat transfer, even without the direct influence of the jets, for all Reynolds numbers. However Case 5.4.5B results show a flat profile once the cross flow effects have dominated the impingement effects. This is most likely due to the tall channel size, which would produce slower cross flow velocities. Also evident from the G_c/G_j plots is the buildup of cross flow is less significant for Case 5.4.5B. Case 5.4.5B tended to produce the poorest jet performance, as the large Z/D prevented proper impingement. This is evident when comparing to Case 5.4.3B, where stagnation points are seen for several X/D downstream. An unusual effect was seen for Case 5.4.1A, where the cross flow actually produced heat transfer coefficient values higher than the initial impingement values. This is due to the

significant amount of cross flow near the exit of this channel.   Figure 7-4 presents

spanwise averaged heat transfer coefficients for the target plates.
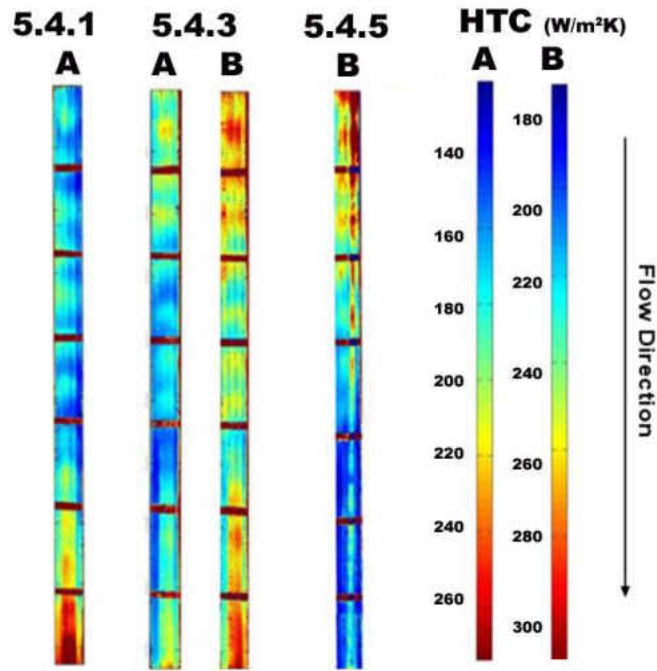
Figure 7-3: Impingement Plate HTC

From Figure 7-4 we see the expected peaks from the jet stagnation from X/D of

zero to 45-50 for all cases. However, beyond this point no significant peaks are seen, as

the cross flow effects have dominated the jet effects. The developing cross flow also

slightly shifts the heat transfer peaks slightly downstream after a few X/D, as well as

causes the impingement peaks to decrease with increasing X/D.   As mentioned

previously, we see the benefit of the smaller Z/D for Case 5.4.1A, as the accumulated

cross flow helps increase the heat transfer coefficient toward the channel exit. However,

although the impingement effects are not as drastic for Case 5.4.5B, appreciable heat

transfer values are still obtained for the first few jets. As expected, the smallest Z/D

produced the most uniform impingement peaks. Peaks are also evident beyond X/D of

50, although cross flow effects seem to have dominated the flow. Just as was seen previously, after significant accumulation of cross flow, the heat transfer coefficients begin to increase again, despite the lack of stagnation points. Also as was seen in the previous comparison, the smaller Z/D provided a larger increase in exiting heat transfer coefficients. These values even surpass those of the first few jets, which is initially surprising. However, after considering the large velocities of the exiting flow, the results seem reasonable.
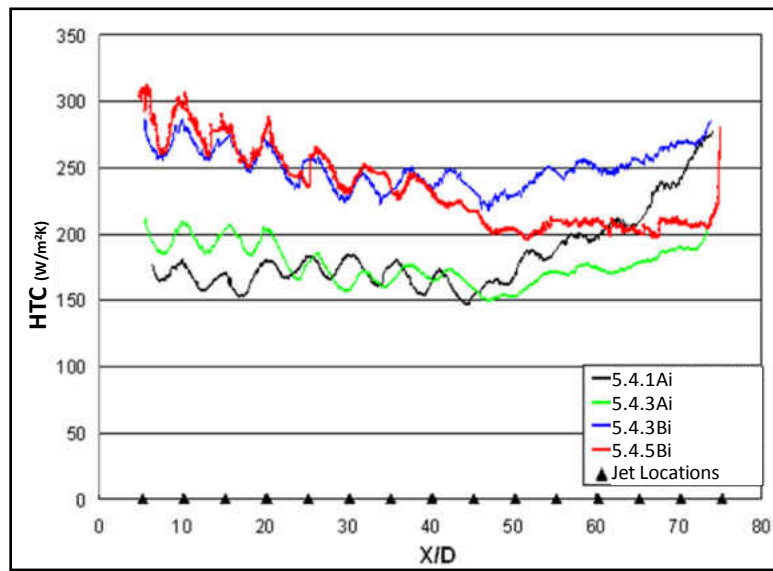
Figure 7-4: Target Wall Spanwise Averaged Results

7.3.1.2   Side Wall

From Figure 7-5 and Figure 7-7 we see the local heat transfer coefficients for the right walls, considering a constant bulk temperature. We see initially the right wall suffers from very non-uniform heat transfer, with the lower portion of the wall having the highest heat transfer, primarily a result of the wall jets on the target plate, formed from

impingement. These results seem to be largely affected by the Z/D. For example, Case 5.4.1A it is initially very evident where the wall jet is interacting with the side wall. Only after significant cross flow has developed does the profile become uniform.
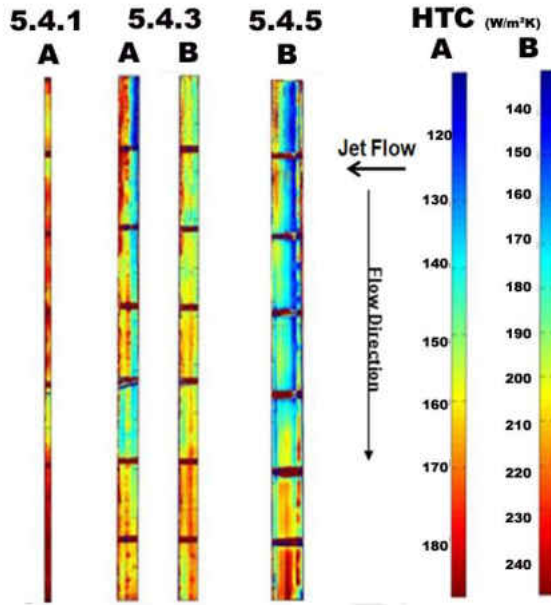
Figure 7-5: Side Wall Local HTC Results
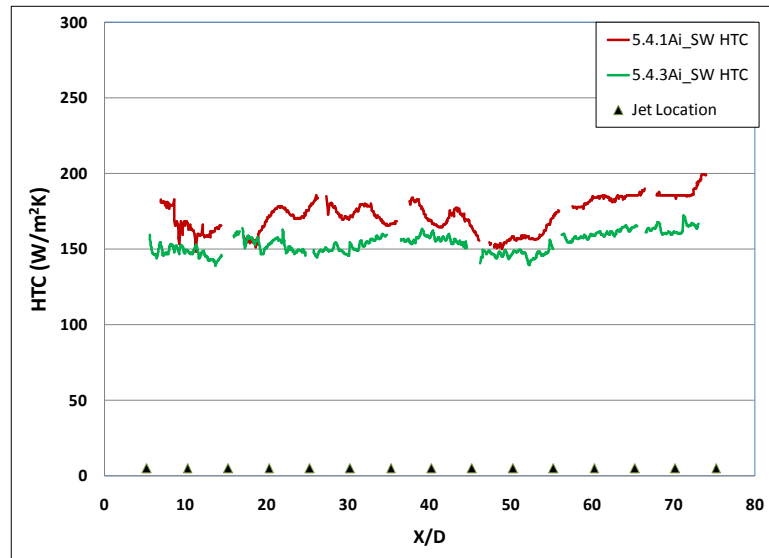
Figure 7-6: Span-averaged heat transfer distribution (X/D=5,A)
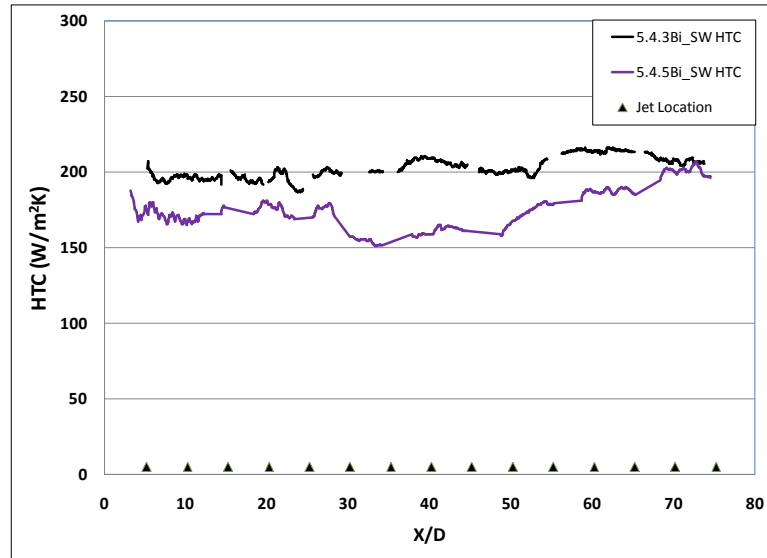
Figure 7-7: Side wall Span-averaged HTC (X.D=5, B)

For the larger Z/D cases near the first few jets, the bottom portion of the right wall has comparable values with the exiting portion. As the cross flow develops, this peak diminishes, most likely due to the interactions between the cross flow and the wall jets. However, the increase in cross flow leads to an increased heat transfer in the downstream direction. Cases 5.4.3A and 5.4.5 seem most similar, while cases 5.4.1A and 5.4.3A also exhibit similar behaviors. This suggests that there is an optimal jet Reynolds number Z/D combination that would provide uniform heat transfer results on the side walls.

The effect of the cross flow developing also leads to the heat transfer coefficient increasing almost linearly after X/D=40 for all cases except Case 5.4.3B. Before this point, however, the heat transfer coefficient is almost constant for all cases. Only Case 5.4.1A has obvious peaks resulting from the impacting jets. For both comparisons, the smaller channel size produces higher heat transfer coefficients, as is expected due to the increased cross flow velocities. Interesting to note, however, is the fact that Case 5.4.3B

yields almost entirely constant values across the entire length. This would be ideal for designers seeking to produce uniform sidewall temperatures. Also worth noting is the rate of increase in heat transfer coefficient for Case 5.4.5B after X/D=50. This must be the result of the rapid increase in cross flow for this case, which directly leads to increased velocities and results higher heat transfer coefficients.

7.3.2   X/D 15-Constant Reference Temperature

It is important for designers to not only design a system which can effectively cool the components below safe operating temperatures, but to also do so efficiently. The next logical step in the investigation is then to see the effects of reducing the number of impinging jets, while maintaining a constant average jet Reynolds number. For these cases, the jet to jet spacing was increased three times, thus reducing the total mass flow rate by a factor of three.

7.3.2.1   Target Wall

Figure 7-8 highlights the heat transfer distribution for the cases with a jet to jet spacing of 15 diameters. Immediately one notices the effects of the reduced levels of cross flow, as all 5 impingement locations are clearly visible in these local distributions.
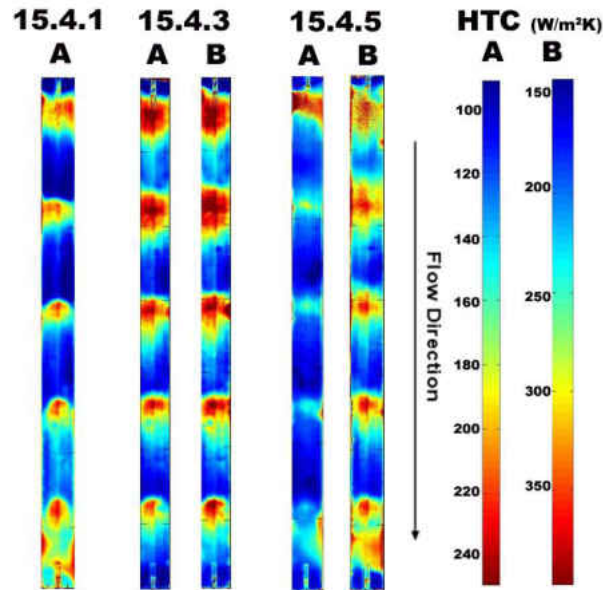
Figure 7-8: Target Wall Heat Transfer Coefficient Distributions (X/D=15)

From this figure, it is evident that the middle channel height (Z/D=3) performs the best at all Reynolds numbers. It is also interesting to note the similarity in the profiles between case 15.4.3A and B, although the levels of heat transfer are different. This suggests that the impingement height plays a dominating role for these configurations. However, considering case 15.4.5A and B, the differences are greater. This suggests that at the taller channel heights, the jet approach velocity has been reduced, increasing the dependence on the jet Reynolds number. At this large spacing, we also see the degradation of the jets, a few diameters downstream of each impingement location. This is expected to create large variations in the uniformity distribution, to be discussed later. Also evident in these plots, is the deflection of the impinging jet and the wall jets from the cross flow. The cross flow is forced to flow around the jet, deflecting the spread of the wall jet in the downstream direction. Impingement locations are also very evident, with distinct peaks at the stagnation locations.

Figure 7-9 shows similar details, with impingement peaks clearly diminishing and shifting in the downstream direction. The cross flow clearly has some negative influence on these geometries. However, proper impingement occurs throughout the channel, and it seems as if there is no transition to a cross flow dominated flow.
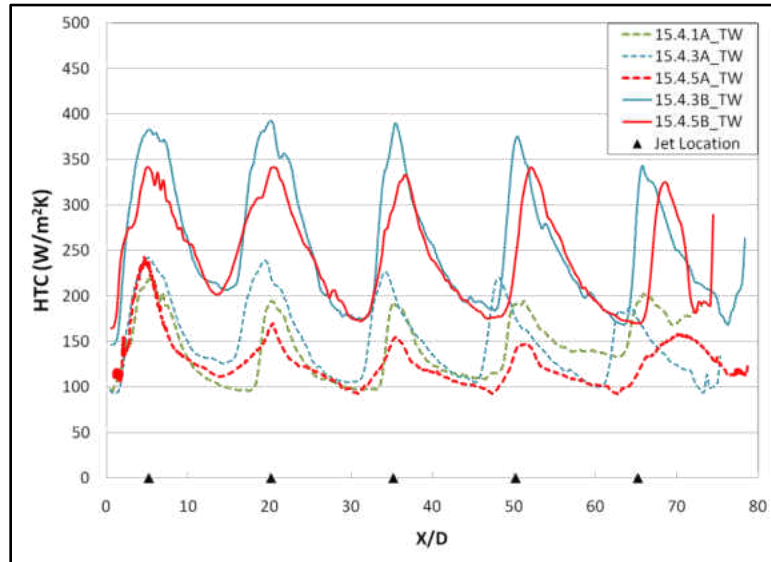
Figure 7-9: Span-averaged Target Wall Heat Transfer Distribution (X/D=15)

Also evident from this spanwise averaged data is the increase in heat transfer with increases in Reynolds numbers, and decreases in impingement height. Results tend to be the closest from case to case at the first impingement jet. This is a reasonable result, as the effects of cross flow have no effect at the first impingement location. The impact of the potential core would then be the driving force at these locations, and would be similar between cases.

7.3.2.2   Side Wall

Similar effects are expected on the side wall, due to the reduced cross flow, which should lead to improved impact of the wall jet. These results are shown in
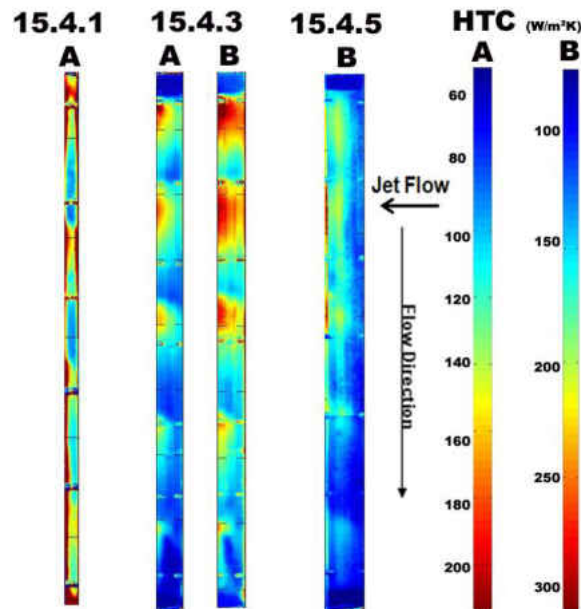
Figure 7-10: Side Wall Heat Transfer Distributions (X/D=15)

As expected the reduced cross flow allows the walls jets to successfully impact the side wall at all jet locations. The effect is reduced, however, in the downstream direction as the cross flow increases. Also evident in these plots is the concentration of the wall jet impact to the bottom of the channel, on the order of 1-2 diameters in height, as discussed earlier. This yields the greatest benefit to the case 15.4.1A, as the wall jet is able to impact the entire side wall. Similar to the target surface, the wide hole spacing allows room for degradation of the wall jet, reducing the heat transfer as one modes away from the impingement location. The stagnation regions are also deflected in the downstream direction, similar to the target surface results. These effects are most evident with cases 15.4.3A and B. Similar characteristics can be explained from the spanwise averaged plots.
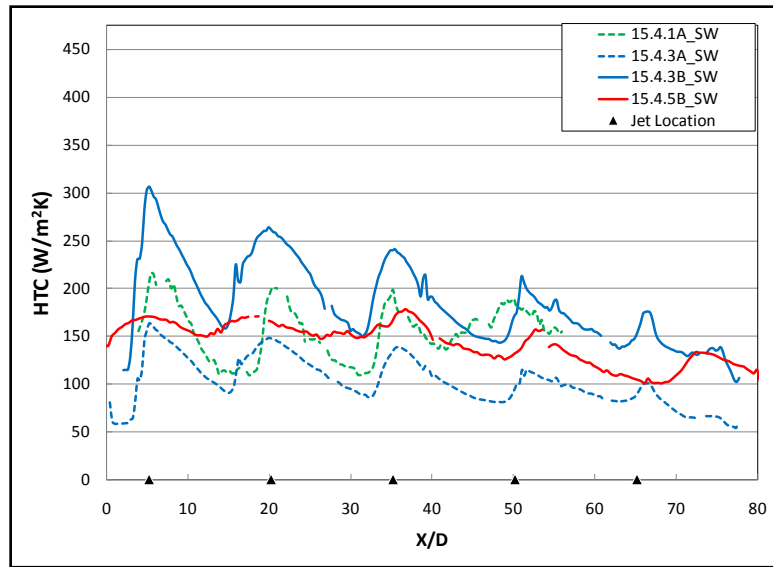
Figure 7-11: Span-averaged Heat Transfer Distribution (X/D=15)

These results again clearly show the effects of increasing the impingement height, and increases in Reynolds number. As the height is increased, the effect of the wall jet is significantly reduced, partially due to the increased surface area, much of which is not affected by the wall jet. Also, as expected, increases in Reynolds number increase the measured heat transfer coefficients, while maintaining a similar profile. The diminishing effect of the cross flow accumulation is also evident in these plots, as the heat transfer peaks decrease in the downstream direction.

7.4   Variable Reference Temperature Effects

7.4.1   Introduction

As mentioned, traditionally the jet temperature is used in heat transfer calculations for impingement and impingement channel cooling schemes. Although in most cases this provides little discrepancies, as the channel length to diameter ratio is increased sufficiently, the jets are no longer the dominating contributor to the heat transferred from

103

the surface. For these scenarios it is necessary to, at the least, examine the trends of potential bulk temperature increase and its possible effects on heat transfer.

It has typically been the convention to use the jet supply temperature as the reference temperature when considering impingement heat transfer calculations, and an energy balance calculated bulk temperature for pure channel flow situations. However, in these unique impingement channel configurations, the actual bulk temperature should lie somewhere between these two extremes. This difference becomes especially important when considering the heat transfer results for the channel side walls or in situations where the cross flow has dominated the heat transfer on the target surface; particularly at large length to diameter ratios. With these cases, the calculated heat transfer coefficient may not be a fair representation of the amount of heat removal potential of the given configuration, especially when comparing to traditional channel flow scenarios. The conversion of this definition, to one that is more physically realistic is therefore necessary. Examination of the different considerations may also give further insight into the behavior of these channels. Three alternative methods are examined, using various available data collected during steady state testing.

A heat transfer coefficient based on a local bulk temperature would then be easily calculated once the bulk temperature can be properly defined. This becomes extremely important to designers, especially considering the spent flow from these channels is often used in film cooling applications. The amount of heat picked up by the working fluid is also a necessary piece of information when one is attempting to calculate the thermal efficiency of these cooling methods (Downs, 2009). An ideal method would be both

easily applied, as well as accurately represent the measured increase in channel bulk temperature.

Neglecting this temperature development has not necessarily introduced significant errors in the literature because of the relatively short channel lengths used. For these cases, heat transfer is typically dominated by impingement, which would have a local bulk temperature close to the plenum temperature used. However, as channel lengths become adequately large, heat transfer characteristics are dominated by the cross flow, which would be at a temperature greater than the reference jet temperature. Additionally, the potential use of the spent cross flow for film cooling requires knowledge of the fluid's average temperature. Several methods of predicting the bulk temperature and recalculating the heat transfer coefficient will be examined.

Bulk temperature trends will be calculated for the three methods, and their effects on the calculated heat transfer results will be discussed. Two cases studied in previous sections will be used to prove the usefulness of the methods.

7.4.2   Steady State Heat Transfer Model

Steady state heat transfer experiments are often used to investigate various flow scenarios, mostly because of the straight forward calculations involved in the process. Heat transfer rates, are defined by Newton's Law of Cooling:

$$Q = h * A * (T_w - T_R)$$

(11)

Experiments typically maintain an isothermal boundary condition, or an isoflux condition on the heat transfer surfaces. Isothermal conditions are only capable in

yielding averaged results; at least with current testing methods. The isofulx condition is often used when one has the ability to measure temperature values at discrete locations. Thermochromic liquid crystals (TLC), temperature sensitive paint (TSP), and infrared are very common measurement techniques allowing this type of measurement. In these scenarios, a known heat flux is generated from the surface of the test specimen, and surface temperatures are measured. The reference temperature is often taken as the local bulk averaged mainstream temperature in most internal flow situations. This value is easily determined from the channel flow energy balance depicted in Figure 7-12.
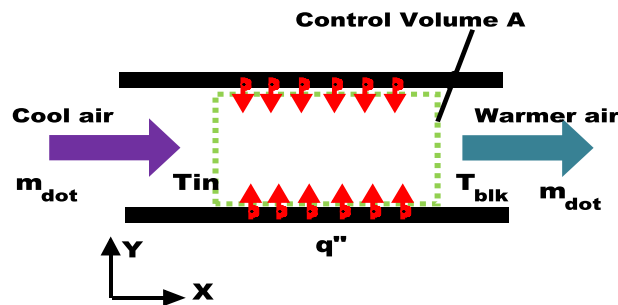
Figure 7-12: Standard Steady State Energy Balance

From the control volume depicted in the figure, a simple energy balance allows one to determine the bulk temperature, from knowledge of the rate of heat input into the air, as given by equation (12). Knowledge of this value, Q_W, is also necessary for heat transfer calculations, and should therefore be readily available. For pure channel flow situations, with a constant heat flux boundary condition, it can be proven that the temperature will increase linearly from inlet to exit.

$$T_{blk}(x) = T_i + Q_W(x)/(\dot{m} * Cp)$$

(12)

An additional control volume is necessary when an impingement channel is considered, however. This, as shown in Figure 7-13, is because there is a periodic injection of cooler fluid into the mainstream. We will assume the two flows are sufficiently mixed directly after the jet, and that the cooler jet does not affect the fluid upstream. It is admitted that this is subjected to disagreement, and is only done for simplicity, as the way in which the two streams mix has yet to be fully understood. We must consider the heat picked up by the heater, plus the additional, cooler mass that enters the control volume.

Figure 7-13: Impingement Energy Balance
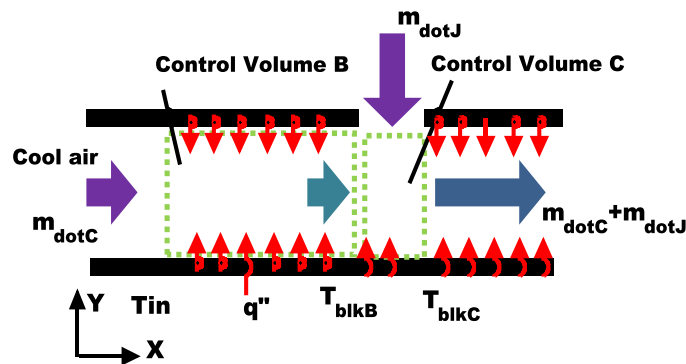
Two sets of equations ((13),(14)) must be solved successively in order to calculate the bulk temperature at all locations within the channel.

$$T_{blkB}(i) = T_{blkC}(i-1) + \frac{\left[Q'_w(i) * X_j\right]}{\left[\dot{m}_c(i) * Cp\right]}$$

(13)

$$T_{blkC}(i) = \frac{\left[\dot{m}_j(i) * T_j + \dot{m}_c(i) * T_{blkB}(i)\right]}{\left[\dot{m}_c(i+1)\right]}$$

(14)

Where:

$$Q'_w(i) = Q_w/L \tag{15}$$

$$\dot{m}_c(i+1) = \dot{m}_c(i) + \dot{m}_j(i) \tag{16}$$

Equation (13) determines the temperature just before the jet of interest, affected by the channel flow heat that was captured by the flow up to this point. The following equation then considers the effect of mixing the warm channel flow air with the cooler jet air.

The amount of heat generated is calculated in various manners, depending on the circumstances. Typically, as is done in the current experiments, the heater resistance is measured (and correlated versus temperature when necessary) and recorded. During testing, the voltage is then measured, and the total heat generated can easily be calculated using Ohm's law. However, it is often necessary to account for heat losses into the environment, as was accounted for in the current tests. This was done by filling the test section with insulation, in order to prevent natural convection, and allowing the heaters to warm the test section to several temperatures. The power required to maintain the rig at each temperature is the amount of heat lost at that point. For the current tests, this was found to be less than 1% of the heat input at any location. Subtracting this amount of heat lost yields an effective q, which should be used in the preceding calculations.

It can be argued that due to the structure of the impinging jet, the jet temperature is a better reference temperature at regions dominated by impingement. However, as mentioned, in some cooling scenarios, the cross flow is ejected in the form of film cooling, and the temperature should therefore be known. It is also sometimes difficult to

determine exactly where one flow feature is dominating. Also, it has been shown in previous works, that when considering the other surfaces of the channel, it may be necessary to consider the effects of bulk temperature increase, especially when cross flow mass fluxes are low. The author intends to examine other methods, which may be simpler to implement.

7.4.3 Proposed Improvements

Three models have been developed in order to conveniently, and accurately predict the bulk temperature rise within an impingement channel. These methods will be explained below, with the baseline case being the traditional jet reference temperature. Resulting methodologies will be applied to two cases, in order to examine their usefulness. Cases 5.4.1A and 5.4.3B have been chosen, with the understanding that the remaining cases will have similar resulting trends. These two cases will be referred to as Case 1 and 2 for the following discussion.

7.4.3.1 Method 0: Jet Reference Temperature

As mentioned, the reference temperature, T_R, is often taken as the plenum temperature, T_P, in impingement and impingement channel heat transfer calculations. It is expected that this technique may prove to be erroneous at large G_c/G_j. However it can easily be argued that this is the correct temperature to use at the impingement location, since the jet is not expected to pick up very much heat as it travels from the plenum to the target surface. Nevertheless, when looking at other surfaces, an actual bulk temperature should be considered. Regardless of the considerations, this method is the most convenient, and is taken as the baseline case.

$$h_0 = q''/(T_W - T_P)$$

<div align="right">(17)</div>

7.4.3.2   Method 1: Linear interpolation between inlet and exit temperatures

As a first attempt at improving the initial assumption of taking the plenum temperature as the reference temperature, one would naturally consider interpolating between the measured plenum temperature, and the exit temperature. This, as discussed, would be accurate during a normal isoflux internal flow situation. Although some error is expected when applying this method to an impingement channel, if it remains within a reasonable amount it would prove to be quite useful as it is also easily implemented. A linear equation could easily be defined and incorporated into the code used to process the data. The accuracy of this method will be explored in a later section. A single thermocouple placed in the exit flow, however, may provide higher uncertainty when highly non-uniform wall temperatures results (Chyu, 1997). A thermopile rake is therefore often chosen as the more accurate alternative, as spanwise variations in the bulk temperature are averaged effectively this way.

$$h_1 = q''/(T_W - T_R(x))$$

<div align="right">(18)</div>

Where:

$$T_R(x) = T_P + \frac{T_e - T_P}{L} * x$$

<div align="right">(19)</div>

7.4.3.3   Method 2: Energy balance marching with points determined before and after
           impingement

Although the exact details of how the bulk flow actually mixes within the channel is anything but certain, it should be expected that a precise energy balance should yield the most physically accurate 1st order results. This would be done using the impingement channel control volumes described earlier. The basic steps are outlined below:

1) Assume the channel temperature is equal to the plenum temperature up to the first hole. This is done to avoid the complexities involved in determining the amount of heat picked up in the small cavity before the first jet. However, it is expected that this change in temperature should be small compared to the remaining influences.

2) Using control volume B, equation (13), the local mass flow rate within the channel, (available from the pressure data), and the known heat fluxes, determine the bulk flow temperature right before the 2nd jet.

3) Using control volume C, equation (14), the mass flow rate through the 2nd jet, and the temperature defined in step 2, determine the mass weighted average temperature leaving the control volume.

4) Repeat this process marching through all of the jet locations.

This method is expected to produce a rather rough, discreet profile, as the continuous ingestion of cooler air should continuously act to push the warmer channel temperature back down. Also, temperatures are only calculated at discreet locations, with the local bulk temperature being linearly interpolated between points. Although it should be the most accurate representation of the bulk flow temperature, it is also expected to be

the most costly in post processing and application requirements. This is because linear interpolation is typically more difficult or memory intensive when included in typical processing codes. The heat transfer coefficient is then calculated according to equation (18), using the interpolated temperature as a reference temperature.

7.4.3.4   Method 3: Energy balance marching with points determined after impingement only

The third method is a simplification of the second method. Although essentially the same amount of post processing work is required, a smoother plot and easier implementation is expected. This is due to the ability to easily curve fit the reference temperature, when calculated in this manner, eliminating the need for interpolation. This method is identical in procedure to the previous method, however only uses the temperatures calculated after the jets (T_{blkC}) for the curve fit. This assumption is assumed to dampen the effects of the continuous ingestion of cooler jet air, which may be a better physical representation. The errors produced by this method are expected to be within the uncertainty of the flow field, again using equation (18) to calculate heat transfer coefficients.

7.4.4   Reference Temperature Results & Discussion

For the conditions given in the selected cases, the resulting reference temperature distributions are plotted. Results are normalized by the plenum temperature (in degrees Celsius), and describe the calculated increase over the measured plenum temperature.
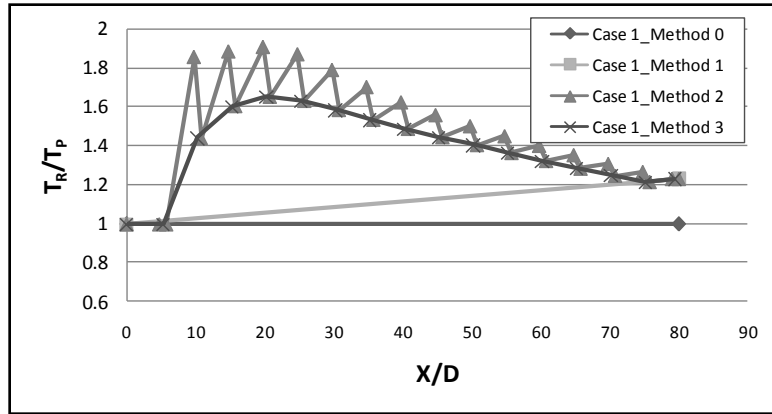
Figure 7-14: Reference Temperature Trends-Z/D=1
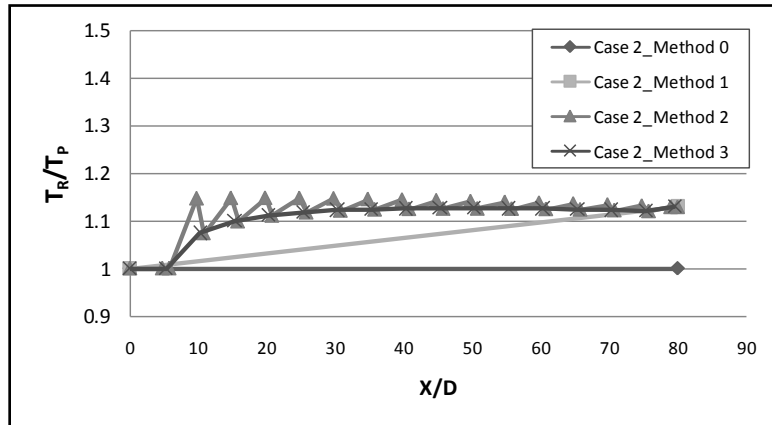
Figure 7-15: Reference Temperature Trends-Z/D=3

The bulk temperature trends for the two different cases foreshadow the effects on the heat transfer expected from the various reference temperatures chosen. It can be argued that method 2 yields the most accurate bulk temperature estimates, as all heat transfer effects are accounted for. All other cases therefore under predict the channels bulk temperature at most locations within the middle of the channel. At locations

downstream, the deviations are small, as all cases, except the baseline, should converge near the measured exit temperature.

It should then be expected that any model will yield heat transfer coefficient values greater than those initially calculated. This is the direct result of using a smaller temperature difference in the heat transfer calculations, resulting from the hotter reference temperature. These effects are highlighted in the next few figures, where the calculated heat transfer coefficient on two of the channel walls (target and side) is presented for the two cases. Plotted with the heat transfer coefficient results are the smooth channel estimates predicted from the Dittus-Boelter (Incorpera, 2002) correlation. The values vary along the streamwise direction due to the progressively increasing mass flow rate within the channel. This value was easily determined from the cross flow mass flux calculations described previously. Its relationship to the impingement results highlight the channel's trend from an impingement dominated flow, with high enhancement, to one that is more dominated by the cross flow, and closer to smooth pipe predictions. Uncertainty bands are also shown to alleviate some of the discrepancies.

Figure 7-16 shows the spanwise averaged heat transfer coefficient results for the target surface of Case 1. As expected, the calculated heat transfer coefficient increases in value along with the increase in reference temperature.
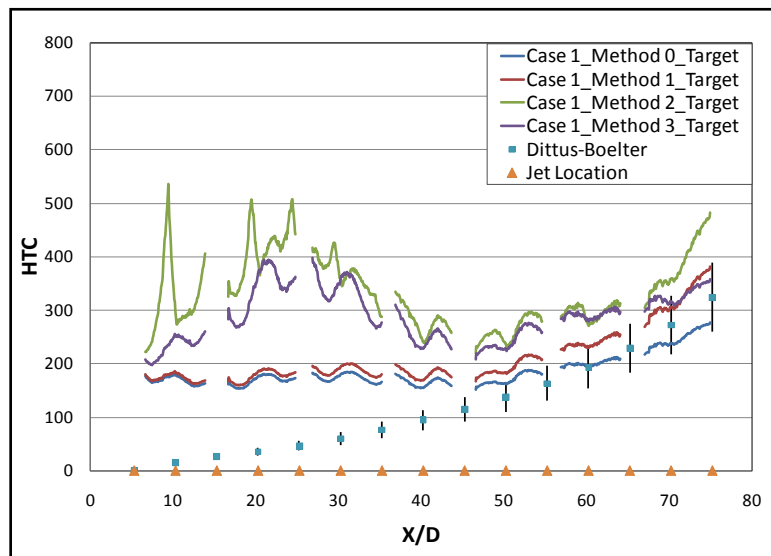
Figure 7-16: Target Wall HTC Trends- Z/D=1

All 4 methods present similar results near the channel entrance, with variations becoming more significant in the downstream direction. Initially one notices the broad peak of methods 2 and 3, between X/D of 10-40. This can be explained in several ways, and is also apparent in Figure 7-17 and Figure 7-14. This peak yields values considerably higher than those calculated from the base line and Case 1. Although these higher values may be unrealistic, they highlight the need for bulk temperatures considerations. More attention will be given to this peak at a later point.
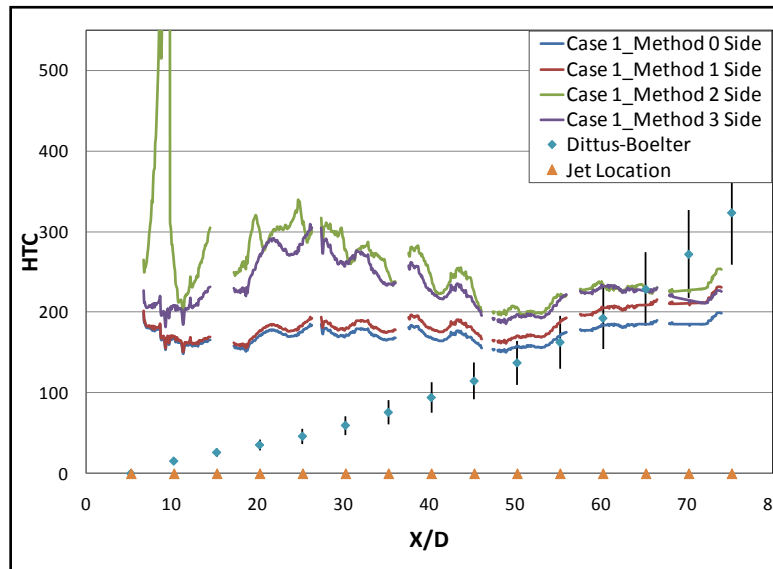
Figure 7-17: Side Wall HTC Trends-Z/D=1

Also worth noting are the large peaks present in the results calculated from method 2. These were also evident in the bulk temperature trends, and represent the large amount of heat that is picked up by the cross flow, while the strong impingement effects maintain low wall temperatures. However, these peaks are expected to be an exaggeration of these effects, since our model did not allow for the cooler jet air to affect the upstream direction, which is more likely the case. Also as mentioned earlier, method 2 proved to be the most difficult to implement, as no curve fit was possible, and bulk temperatures had to be interpolated at most locations. Method 3 yields results that are similar to the method 2, without the large peaks before each jet. The broad peak is still captured, as well as the increased heat transfer values in the downstream direction. Method 1 was implemented with the least amount of additional work, and results in a profile that lies nicely between the base line and the control volume cases.

116

The relative value of these heat transfer coefficient values with respect to smooth channel predictions is also improved by using some sort of bulk temperature consideration. Notice that for both walls, there seems to be very little augmentation in the downstream direction, as the values fall very close to the predictions. This may be hard to accept initially, even though the flow is presumably dominated by cross flow. The expected increased turbulence and mixing from the downstream jets would lead one to believe the values at this location should continue to be greater than those predicted by Dittus-Boelter. Only when the bulk temperature effects are considered is this true.
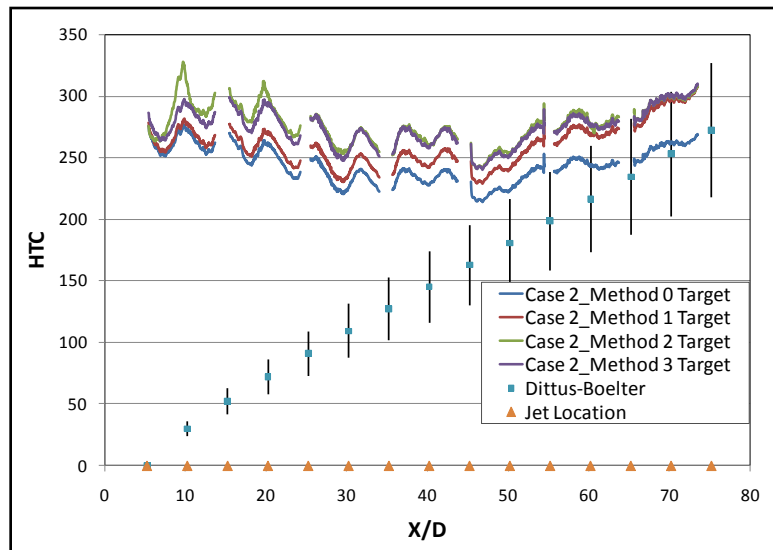
Figure 7-18: Target Wall HTC Trends-Z/D=3

Similar effects are seen when examining the results of Case 2. Because of the relatively larger cross flow and jet velocities in the upstream locations, the difference between methods 2 and 3 is smaller. All methods tend to yield similar results in the upstream locations, with methods 2 and 3 yielding almost identical results along the entire channel. Again, method 1 falls between the two extremes.

117
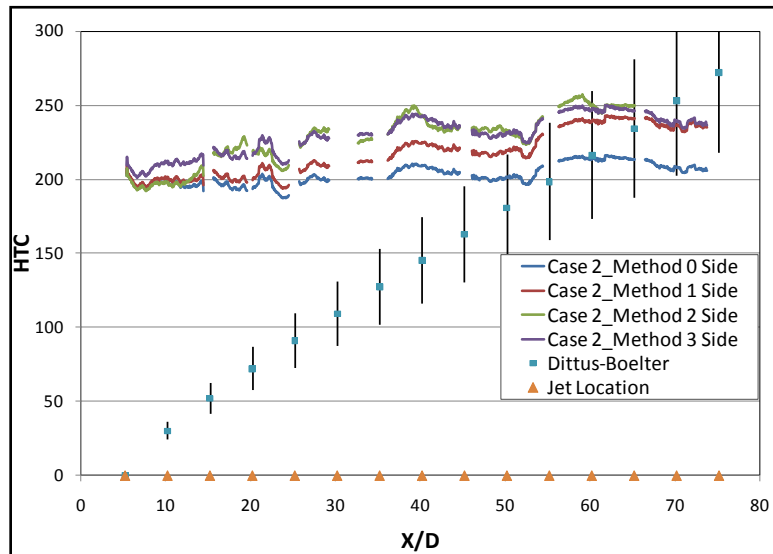
Figure 7-19: Side Wall HTC Trends- Z/D=3

The augmentation effects again become important for this case in the downstream directions. Examining the baseline case in the downstream locations, one would assume that the impingement channel has failed to improve the heat transfer characteristics over that of a smooth channel, similar to Case 1. However, once consideration is given to the possible rise in the reference temperature, the augmentation becomes much more apparent. The differences between the 3 methods are less pronounced for this case, especially in the downstream direction.

7.5 Circumferential Heat Flux Variations

It is a well understood and accepted fact that for a turbulent flow field, the boundary conditions do not play a major role on the heat transfer coefficients. For example, although it is expected that a constant heat flux boundary condition would yield

heat transfer coefficients that are higher than those calculated for a constant temperature boundary condition, these differences are often accepted as negligible for the turbulent flow field. As discussed earlier, there have been several fundamental studies that show experimentally and analytically that the effects of flux variations are small for the smooth channel scenario.

Because double wall cooling is most effective when the channels are placed close to the heat source (the hot gas), they are exposed to highly non uniform heat flux distributions. The target surface would experience the highest temperatures, and thus largest heat loads. The levels of these heat loads will then decrease as one moves around the circumference of the channel to the jet plate, which would experience the lowest loads. Because of this, it is necessary to verify the assumption that these variations will not affect the measured heat transfer coefficients.

A set of tests were carried out, varying this flux distribution by turning off the heaters to selected walls, and recording the resulting distributions. It is expected that these variations would have some effect on the bulk temperature distribution, but not on the actual distribution of heat transfer coefficients. However, since as previously discussed, these effects are not typically accounted for with impingement heat transfer testing, there is expected to be some slight deviations in the downstream direction, where the differences in flow temperatures would have some effect on the measured surface temperatures.

A summary of the flux variation nomenclature is repeated in Table 7-1 for convenience.

Table 7-1: Heat Flux Variation Summary

Heat Flux Variations	
Sub-Case	Heated Surfaces
i	A,B,C,D
ii	A,B,C
iii	B
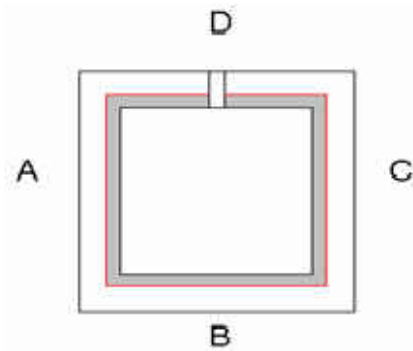
7.5.1   5.4.1A Heating Variations:

Figure 7-20 highlights the effects on the target surface between the different heating scenarios for geometric Case 5.4.1A, with a Z/D of 1. Little difference is seen between the uniform heated case, and the case with only the target wall and side walls active. However, for the condition with only the target surface active, a slight rise in heat transfer coefficient is observed, even at the first few X/D. This suggests that considerable power was input through the side walls, and making them inactive had a significant effect on the amount of heat that is picked up by the developing cross flow. This fact is verified by examining the total heat rate applied to each wall, with the top wall being powered at about 86% of the side wall power; a result of slightly lower heat transfer coefficients on the jet plate surface, and the fact the side walls have a comparable amount of surface area to the jet plate. The difference between Case 5.4.1Aii and Case 5.4.1Ai becomes greater with increasing X/D, as the additional heat input from the jet plate has a noticeable effect on the bulk temperature. As previously mentioned, the fact that the bulk flow temperature is physically lower for the non-uniform cases, it would be expected that the

surface temperatures are slightly lower as well. Because we assume a constant bulk temperature in our calculations, the effect of the lower surface temperature is to yield a larger heat transfer coefficient, possibly unrealistically. The increase in heat transfer coefficient between cases 5.4.1Ai and 5.4.Aiii is an average of 6% that of the uniformly heated case. The average heat transfer coefficient measured for Case 5.4.1Aii is approximately 3% greater than Case 5.4.1Ai.
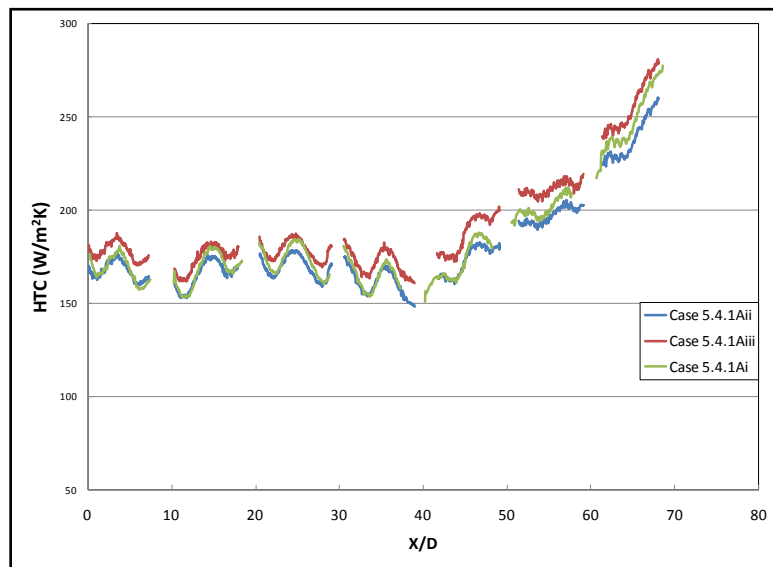
Figure 7-20: Heating Variation effects: Case 5.4.1 Target Wall

Similarly, Figure 7-21 shows the sidewall results. Again, the small contribution of the jet plate to the bulk temperature increase is seen here. The two scenarios yield almost identical results, up to an X/D of about 60, where the non-uniform case rises slightly above the uniformly heated case. This small difference can be attributed to, again, the slight difference in actual bulk temperature. The fact that the difference is only noticeable at the last few diameters also highlights the fact that the jet plate did not provide a significant amount of heat to the cross flow, again because of the lower heat transfer coefficient on this surface.
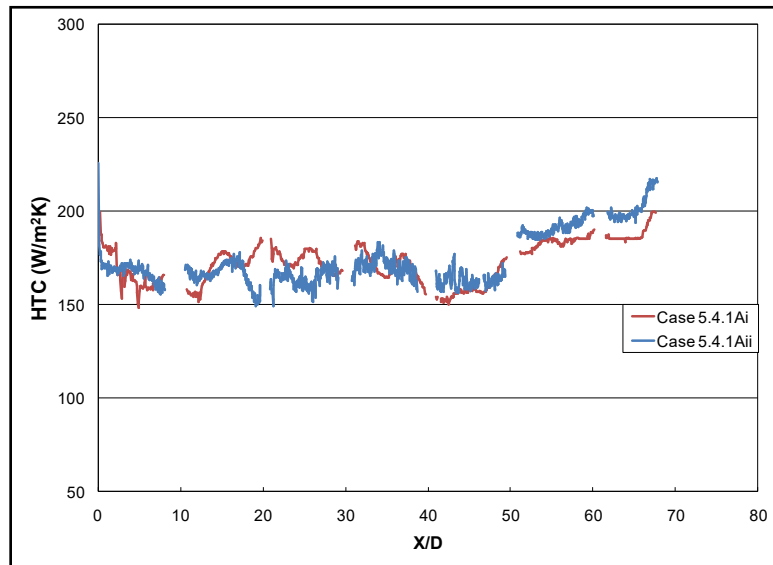
Figure 7-21: Heating Variation Effects: Case 5.4.1 Side Wall

7.5.2   Case 5.4.3B Heating Variations:

Cases 5.4.3Bi through 5.4.3Biii target surface results are shown in Figure 7-22. As with the previous cases, the overall trends are nearly identical, with the average heat transfer coefficient increasing as the walls are turned off. The difference between the first two scenarios, Case 5.4.3Bi and 5Bii is the smallest, around 6% of the uniformly heated case; and the difference between the later 2 cases is larger, with Case 5.4.3Biii measured at about 10% larger than Case 5.4.3Bi. This, as with the previous case, is a result of the larger heat input from the side walls when compared to the jet plate. The difference does not increase significantly as one moves downstream, due to the fact that the cross flow is still moving relatively fast, especially when compared to Case 5.4.5B.
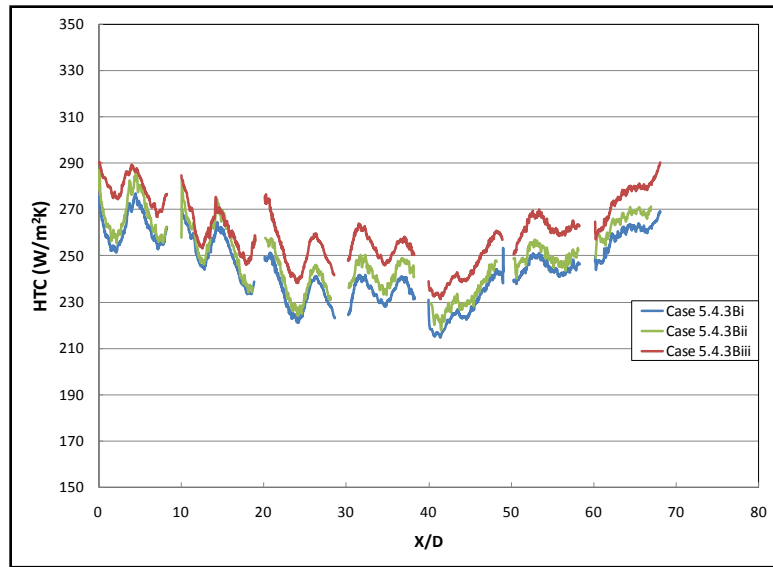
Figure 7-22: Heating Variation Effects: Case 5.4.3B Target Wall

Again, Figure 7-23 shows the side wall results for the various heating scenarios. The differences for this case are smaller than those for the previous, which seems to make sense since the side wall, being larger for this case, must provide a larger portion of the heat than for the previous geometry. Of particular interest is the fact that the curves do not diverge near the channel exit, as they did in the previous case; again the result of a lower significance of the heat input from the jet plate. This again was verified by examining the power inputs for this case, with the jet plate being powered at just 52% of the side walls. This is partially attributed to the fact that the side walls have a slightly better heat transfer coefficient, but also by the fact that the side wall surface area is 50% greater than that of the jet plate, thus contributing a significant amount of heat.

123
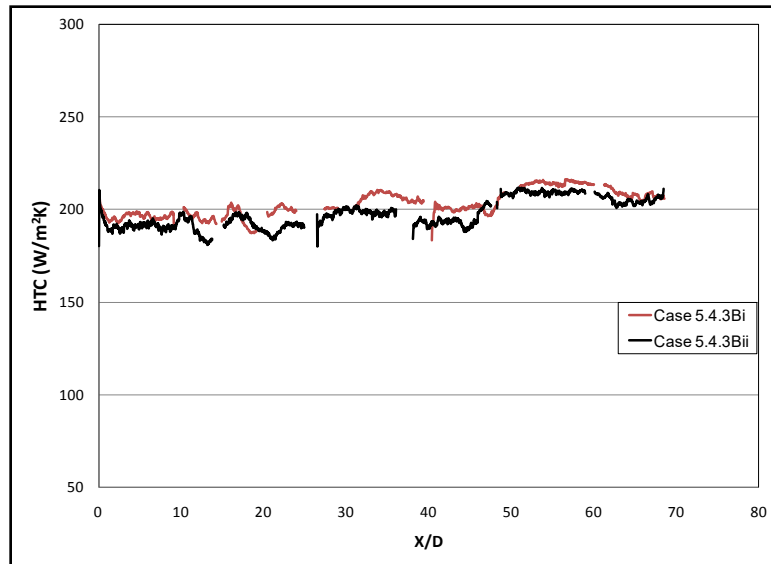
Figure 7-23: Heating Variation Effects: Case 5.4.3B Side wall

7.5.3   Case 5.4.5B Heating Variations:

In Figure 7-24 we see the target plate results for geometric Case 5.4.5. At the first few X/D there is no significant difference between the 3 scenarios. However, as the cross flow develops and potentially heats up, a larger difference is seen. This is the direct influence of the cooler cross flow temperature for the cases with non-uniform heating. We again expect the surface temperature to be driven to a lower value because of the lower bulk temperature. As mentioned this results in a larger calculated heat transfer coefficient, than for the case with uniform heating. However, for this case it seems the jet plate provided a significant amount of heat when compared to the previous cases. This again is verified by examining the power input to the various walls, with the top wall being powered around 75% of the side walls. This suggests that for this large Z/D, the jet plate surface begins to show comparable heat transfer coefficient to the remaining walls. Also, because of the lower cross flow velocities, the sidewalls do not perform as

124

well compared to the remaining surfaces. The area where their influence is most likely greatest is at the channel entrance, where Case 5.4.5Biii is consistently higher than the remaining two cases. This area of the channel, however, has the potential of behaving in an unusual manner, due to the pocket formed between the first jet and the closed channel side. Air must circulate in this section, and possibly pick up heat, before it is carried out the rest of the channel. For cases 5.4.5Bi and 5.4.5Bii, this heat pick up must be significant enough to produce a peak for Case 5.4.5Biii, where the temperature rise would not be as significant. This case also exhibits the largest variation between the cases, especially as the cross flow begins to dominate. This is evident in the fact that the peaks have almost completely diminished by X/D of 35. Because of the larger Z/D, the jets are not able to successfully impinge the lower surface beyond this point, and the major contributor to the heat transfer is the accelerating cross flow. This cross flow, again because of the large Z/D, is moving slower than in the previous geometries, allowing more time for the fluid to warm up while in contact with the active surfaces. The exiting bulk temperature was slightly lower for the two non-uniform cases than for the uniform case. Case 5.4.5Bii yields results 14% greater than Case 5.4.5Bi, and Case 5.4.5Biii yields results 18% higher than Case 5.4.5Bi.
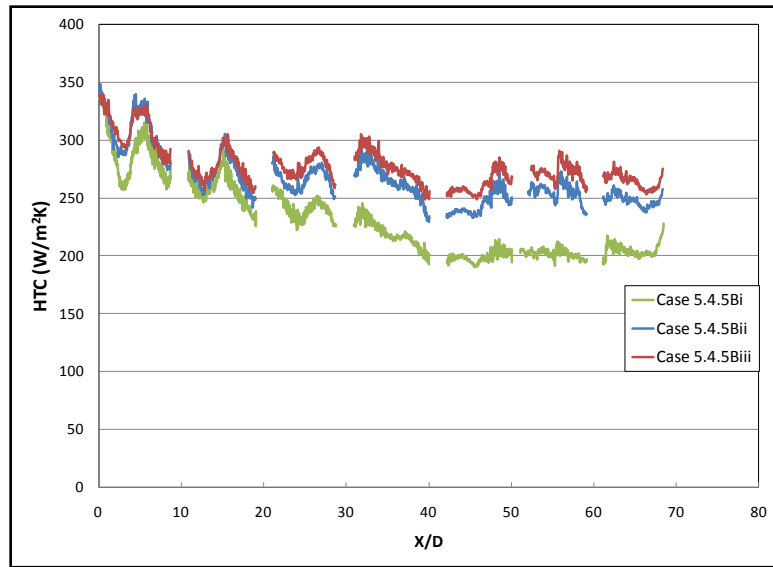
Figure 7-24: Heating Variation Effects: Case 5.4.5B Target

The side wall results for cases 6Bi through 6Bii are shown in Figure 7-25. Again, as expected, the overall trend is similar, and the values are close within the first 30-40X/D. Beyond this point, the heat transfer coefficients begin to deviate, up to 18% at the channels exit. Similar to the previous cases, this is due to the lower cross flow temperature with the non-uniform cases. Compared to the previous cases, providing no power to the top wall has the most significant effect on the side wall heat transfer coefficients. However, this effect is not seen until one moves far enough downstream, where the difference in bulk temperature begins to become significant.
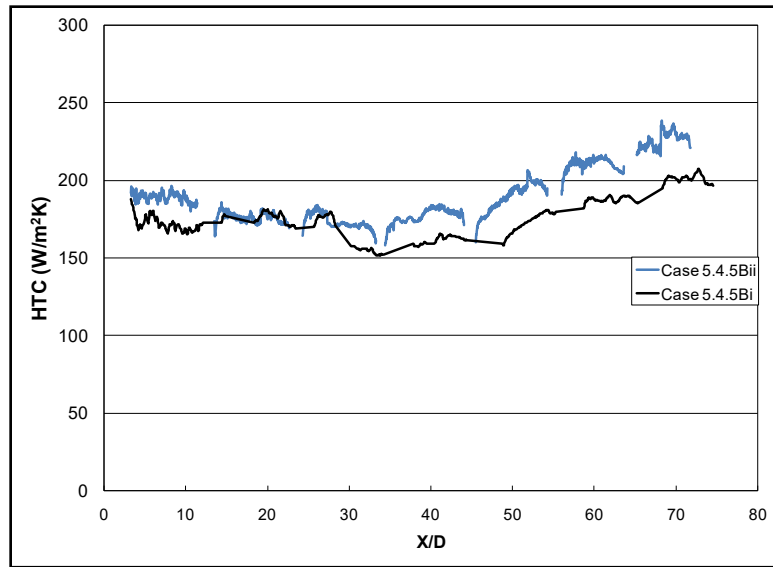
Figure 7-25: Heating Variation Effects: Case 5.4.5 Side Wall

7.6   Comparison to Literature

7.6.1   Introduction

In order to examine the validity of the existing correlations in the presence of side walls, (Florschuetz, 1981), spanwise averaged results are compared against predicted values, for both a smooth channel as well as an impingement channel. This is necessary for several reasons. The majority of the literature and specifically in the study by Florschuetz, multiple rows of jets in the spanwise direction are used. This allows one to neglect the interaction of the side walls. Also, the number of holes used in the first iteration of tests (15 for X/D=5) is larger than that typically tested in the streamwise direction. In this case a large degradation of jet performance results from the large build up of cross flow. The exhausted jets, as described earlier, do not perform as intended, with cross flow effects dominating the heat transfer process.

127

Both the target surface, as well as the side wall spanwise averaged plots are presented, along with per jet averages for the target surface. Uncertainty bands are based on worst case values reported in the appropriate literature: +/-12.3% for presented heat transfer coefficient results, +/- 18% for Florschuetz correlation, and +/- 20% for Dittus-Boelter correlation. Comparisons are made against smooth channel predictions, as discussed earlier, using the channel Reynolds number distribution shown previously. As mentioned, this will aid in distinguishing how beneficial the flow arrangement is, compared to a standard smooth pipe cooling arrangement, run at the same channel Reynolds number.

7.6.2 X/D=5

For Case 5.4.1, with a Z/D=1, the side and target surfaces perform similarly, up to a X/D of 45. These results are shown in Figure 7-26. At this point, the target surface continues to increase in heat transfer coefficient, while the side wall somewhat settles. These effects are due to the increased cross flow at this position, which becomes strong enough to deflect the walls jets formed from impingement, which can still sufficiently occur because of the small channel height. There seems to be a direct interaction between the sidewall heat transfer coefficient and the target surface profile, as they almost lie on top of each other in the upstream part of the channel. When comparing to the available impingement channel correlations, acceptable results are obtained at the first jet as well as from X/D=30-70. The correlation seems to under predict the values in the upstream section and then over predict them in the downstream region. These discrepancies may be the result of the side wall influence, which was not present in the

experiments conducted by Florschuetz (1980). In the upstream region, the side walls tend to increase the heat transfer, because of the second impingement region that is developed from the wall jets impacting the side surfaces. However, as the cross flow develops significantly, the contribution of the side wall is less, and the correlation tends to over predict the recorded results, still within the uncertainty bands. The correlation tends to digress in regions where the side wall influence is large. It is also interesting to note how the smooth channel prediction comes close to the values predicted by Florschuetz (1980), as well as those recorded, beyond an X/D of 50. At this point impingement effects are becoming minimal when compared to the cross flow effects. Nevertheless, the augmentation due to impingement produces some enhancement.
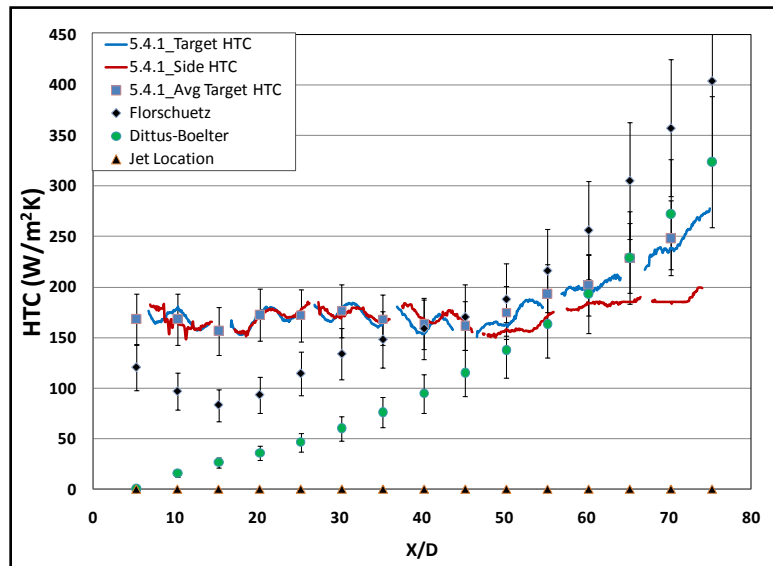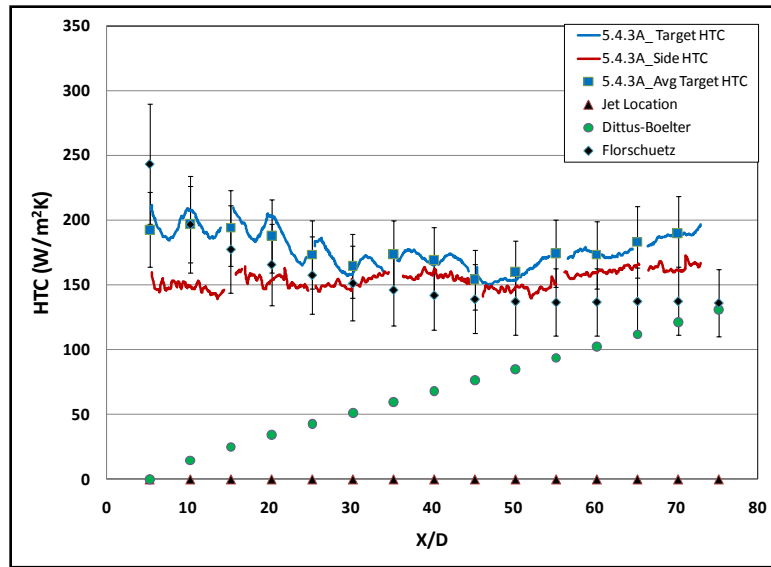

Figure 7-26: Span-averaged literature comparison (5.4.1A)

Similarly Case 5.4.3A averaged results are presented in Figure 7-27. From this plot, it is evident that with the larger impingement height (Z/D=3) the side wall heat transfer coefficient values do not compare as well to the target surface. With the

129

increased channel height, as was evident from the local heat transfer coefficient distributions, there is less influence from the target surface on the side wall. The larger channel height creates lower cross flow velocities, which do not maintain the higher side wall heat transfer coefficient values observed in the previous case. The side wall profile tends to be more flat, with less evidence of impingement. Target heat transfer coefficient values fall within the uncertainty band of the existing correlation along the entire channel, again suggesting less influence from the side wall. However, beyond the first 3 holes, the correlation tends to slightly underpredict the actual heat transfer coefficient values. The slight increase in turbulence due to the presence of the side wall, although the coupling is weak, may be blamed for this inconsistency. Again, smooth pipe predictions approach the recorded values in the downstream regions. For this case however, the enhancement due to impingement is larger, creating some augmentation even at the channel exit. Note, however, that for all cases, the impingement channel correlation approaches that of a smooth pipe when significant cross flow is present. The fact that the heat transfer becomes dominated by cross flow effects in the downstream regions is then more apparent.

Figure 7-27: Span-averaged literature comparison (5.4.3A)

Case 5.4.3B, shown in Figure 7-28, yielded similar results to Case 5.4.3A, when considering the coupling between the side wall and target surface. Again, the side wall underperforms the target surface, as the effects of impingement are less apparent on this surface. As mentioned earlier, this case yielded the most uniform heat transfer coefficient values throughout the channel, suggesting an optimum configuration. However, the existing correlation does not yield very acceptable results for this configuration in the upstream regions. It significantly over-predicts the first few jets, at or beyond the limits of the uncertainty band. Not until significant cross flow has developed does the correlation yield accurate results. However, after 3 jets, the results do overlap. The side walls may cause some recirculation that negatively affects the impingement at this location, causing lower heat transfer coefficients in this region. Visualization methods are required to determine the exact phenomena that cause this discrepancy. Compared to the previous case, there is less enhancement over smooth

131

channel predictions in the downstream regions. Both the side and target walls approach the smooth channel predictions, where as with Case 5.4.3A, the target surface outperforms the side wall and the smooth channel predictions near the channels exit. This increase in Reynolds number also results in increased levels of turbulence. Therefore, any increased turbulence due to the presence of the downstream jets and side walls has less of an effect at high Reynolds numbers. At low Reynolds numbers, the incoming jets may act to increase the turbulence of the flow, even if no impingement successfully occurs.
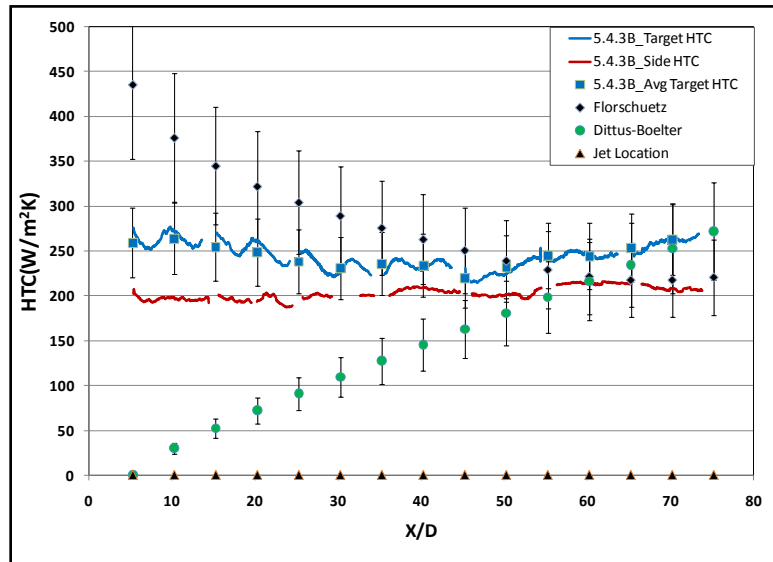
Figure 7-28: Span-averaged literature comparison (5.4.3B)

Finally, at the largest impingement height, the two surfaces again seem to be only weakly coupled, as seen in Figure 7-29. The target surface in this case outperforms the sidewall throughout the channel, due to the low cross flow velocities resulting from the large channel height. Again, there is no evidence of impingement along the side wall, due to the large side wall surface area compared to the possible size of the wall jets

(typically on the order of 1-2 jet diameters (Martin, 1977). This case, however, matched the predicted results with surprising accuracy. It is also interesting to note that this case is beyond the parameters tested in the literature, Florschuetz, (1980), where maximum impingement heights of 3 diameters were tested. Nevertheless, the results match nicely. Throughout the channel, the correlation held well within the uncertainty bands of both sets of data. This agreement implies that as the channel height is increased significantly, the side wall coupling becomes less apparent, and traditional impingement channel correlations apply. However, with these cases, there is the drawback of lower heat transfer coefficients along these side walls.
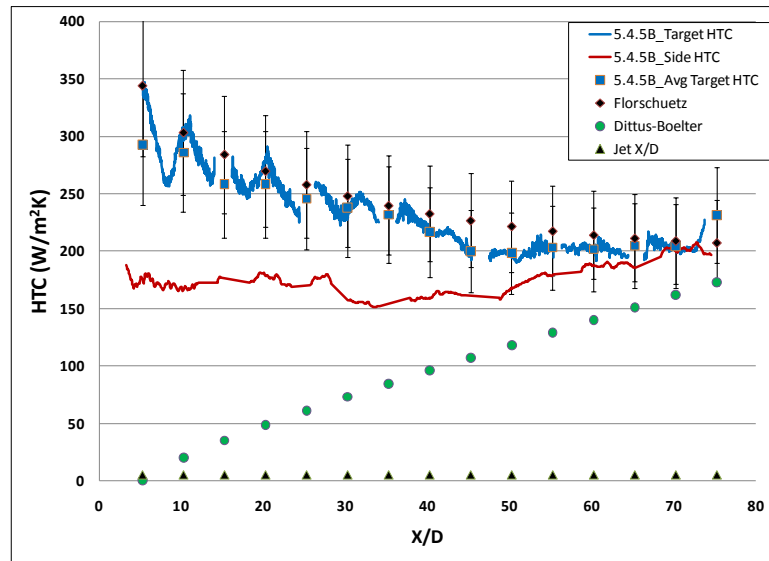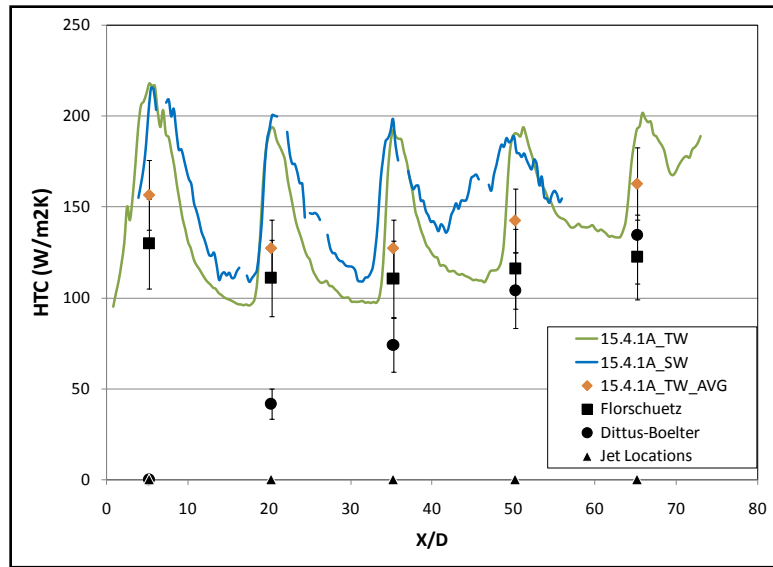

Figure 7-29: Span-averaged literature comparison (5.4.5B)

From these results, it is seen that the influence of the wall does play a critical role in the heat transfer levels, as acceptable predictions were only made for the tallest channel size. A similar comparison with an increased jet to jet spacing would give insight into the dependence of this influence on the jet interaction.

7.6.3   X/D=15

With the previous cases, it was observed that with a large influence form the channel side wall, available correlation predictions introduce some errors. The previous cases, however, include holes that are relatively closely spaced, suggesting there is some interaction between jets in the streamwise direction. By repeating this comparison with larger spaced holes, we wish to show that this side wall interaction is lessened.

Figure 7-30 presents this comparison for case 15.4.1A. One immediately notices that the agreement between the available correlation and the data is surprisingly good. The interaction between walls is still apparent, as the profiles are almost identical. We also notice that the results approach smooth channel predictions in the downstream direction, similar to before. However, they do not quite converge with the predicted results, as the levels of cross flow are less significant for the present case, due to the lesser number of holes. However, cross flow contributions do seem to be significant, as the values do become close near the channel end. It could be inferred that given more jets in the downstream direction, convergence would be achieved.

Figure 7-30: Span-averaged literature comparison (15.4.1A)

There seems to be some evidence that the larger jet spacing reduces deviations from the existing correlations. Figure 7-31 presents this comparison for case 15.4.3A. Similar to the previous cases, we see the coupling effect between the surfaces has decreased slightly. This is evident from the fact that the heat transfer levels on the side wall, although similar in trend, are lower than target heat transfer surface results. Although experimental results are slightly higher than predicted values, the results do overlap throughout the profile. The difference between the results may be due to the increased levels of turbulence, introduced from the wall jet impacting the side walls. The difference between the results tends to be rather consistent, suggesting the increased levels are the result from some additional phenomena that is consistent throughout the channel. Also interesting to note is the fact that smooth channel predictions are significantly lower than the impingement results. Although this is entirely expected in the upstream locations, as the large enhancement levels are expected, downstream one

135

expects the results to eventually converge with the smooth channel predictions. However, for this case, the increased channel size and jet spacing results in low channel Reynolds numbers. This highlights the great benefit of impingement cooling in general; the realization of large heat transfer coefficients with minimal amounts of coolant usage. The drawback, as highlighted earlier, is the large pressures required to drive the flow.
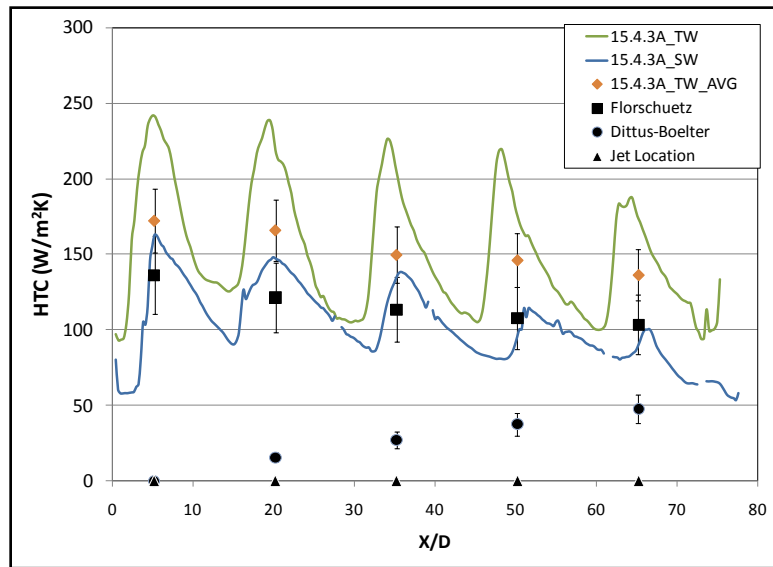
Figure 7-31: Span-averaged literature comparison (15.4.3A)

As Reynolds number is increased, we expect similar comparison between experimental results and predicted values. This is shown in Figure 7-32. Very similar trends result, with increased heat transfer levels due to the increased jet Reynolds number. The behavior and differences between results tends to be the same. This suggests that increasing the Reynolds number, at least within the currently tested range, does not introduce any new physical phenomena. The agreement between predicted values and experimental results are better in this case. This would be the result of the heighted impingement Reynolds numbers. As the Reynolds number is increased the

levels of turbulence introduced by the jet increase, as well as the impact of the impingement itself. The secondary effects from the channel side wall become less significant, leading to better agreement between the data. Notice, however, that smooth channel predictions are still consistently outperformed.
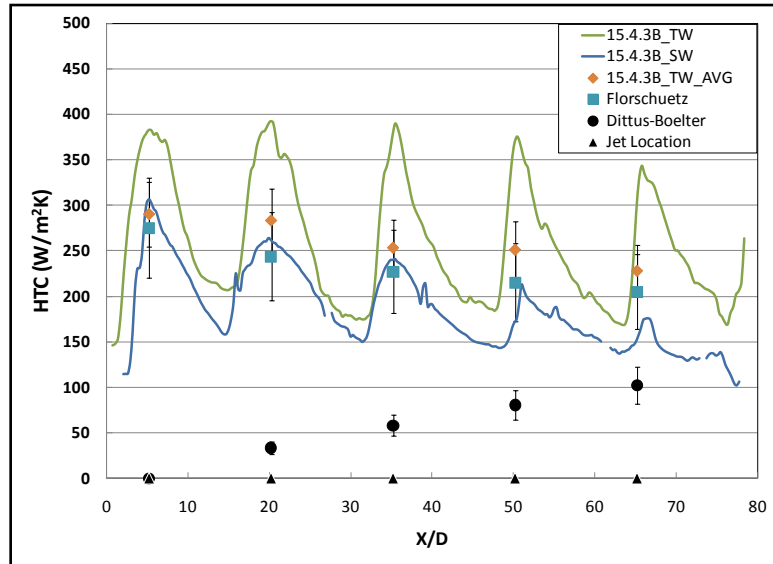
Figure 7-32: Span-averaged literature comparison (15.4.3B)

As the channel height is increased further, cross flow effects will continue to be less. This is the first observation in Figure 7-33. We see that due to the large channel size (and equal total mass flow as the earlier low Reynolds number cases), the smooth channel predictions at the given channel Reynolds numbers are extremely low. This is the most significant deviation from the previous cases, especially those with a jet to jet spacing of 5 diameters. Because there are only 5 jets in the streamwise direction, no appreciable velocities are developed due to cross flow, and all of the contributions to the heat transfer is from the jet impingement against the surface. Similar to the previous

cases with X/D=5, the predicted values match best for the tallest channel size. This again

strengthens the argument of reduced coupling between the side and target surfaces.
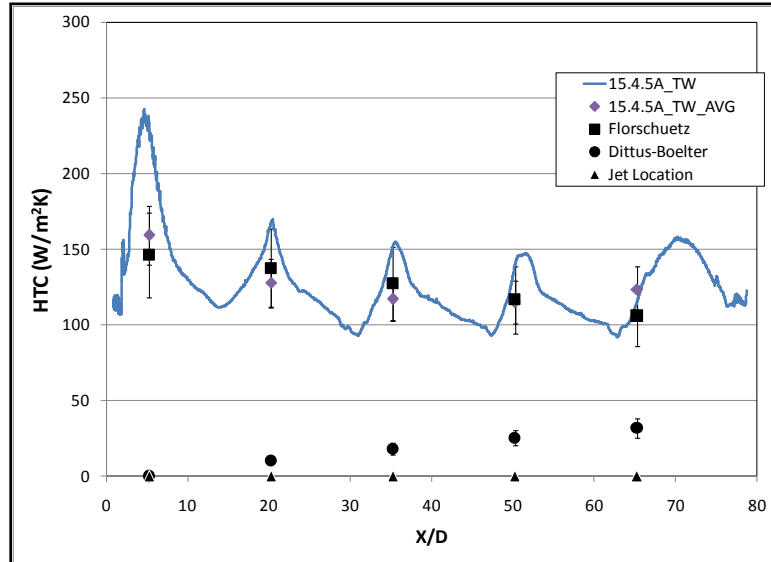
Figure 7-33: Span-averaged literature comparison (15.4.5A)

Finally, for case 15.4.5B, we again expect excellent agreement between our

results and the correlation, as well as significant enhancements over smooth channel

predictions. This is the case as is described in Figure 7-34. Similar to case 5.4.5B, we

see very little interaction between the two surfaces. However, the interaction here does

seem to be more significant, as the impingement of the wall jets against the side walls is

still obvious, although small in magnitude. However, since the heat transfer levels are

significantly higher than the smooth channel predictions, one can conjecture that the

majority of the heat removed in this location is due to this impacting wall jet, as well as

the turbulence created from the impinging jets. Once again, the cross flow contributions

are extremely small, due to the large channel height.
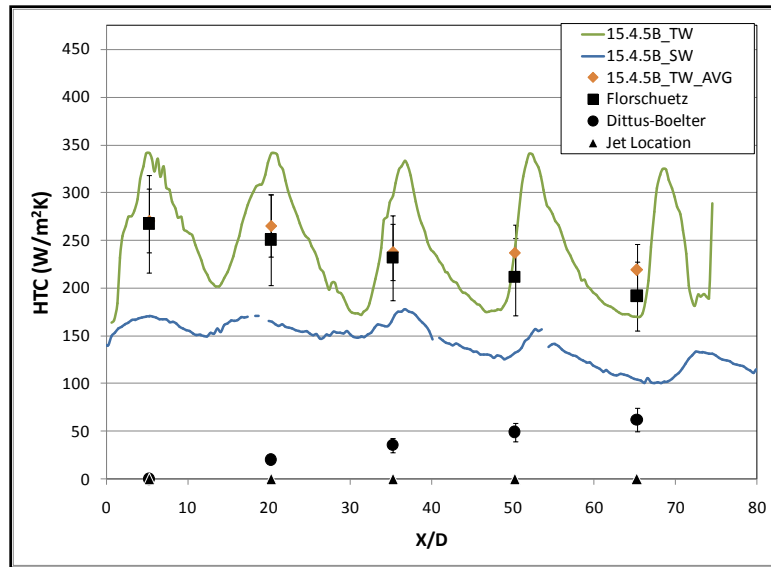
Figure 7-34: Span-averaged literature comparison (15.4.5B)

The presented comparisons against the available correlations suggest several things. Initially, as described, we see that with increases in channel height, the interaction between the target surface and side wall decreases. This tends to drive the measured heat transfer levels down toward the predicted values, which tend to underpredict heat transfer levels for the large spaced arrays. We also conclude that with the increased jet spacing, the contribution from the developed cross flow is almost negligible, especially for the largest case. In order to determine the optimal configuration, however, a deeper analysis is required.

7.7   Uniformity Distribution

A study on the uniformity of the heat transfer coefficient distributions is presented. This cooling technique characteristic is rarely examined in the literature.

7.7.1 Introduction

The introduction of thermal stresses is one possible drawback to the use of impingement jets. Because of the large variation in heat transfer coefficients moving from the core of the impingement location, to regions only slightly affected, there is a high potential for thermal gradients. This is especially important for designers, as these stresses eventually lead to a reduction in the predicted life of the machine.

7.7.2 X/D=5

In order to get a thorough understanding of the performance variations in these channels, uniformity distributions for both walls are shown in Figure 7-35 and Figure 7-36.
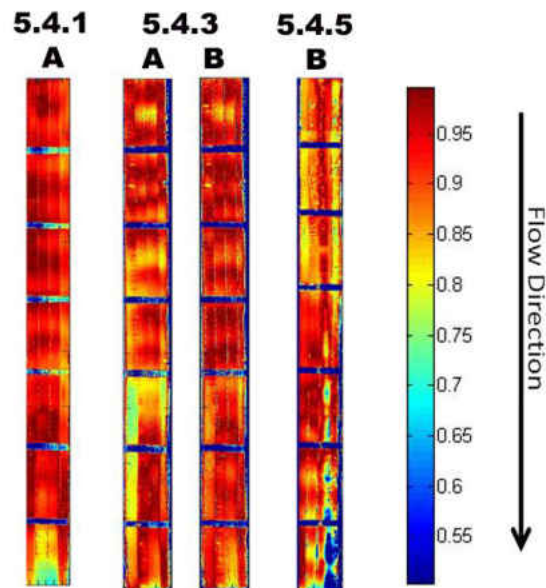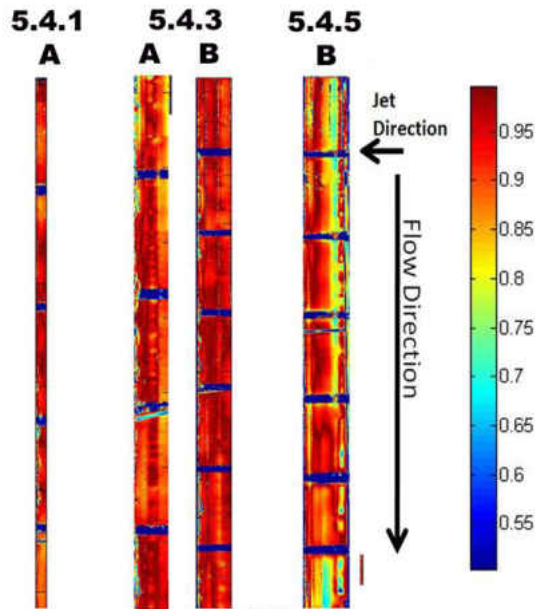

Figure 7-35: Target Wall Uniformity Distribution (X/D=5)

Figure 7-36: Side Wall Unifomity Distribution (X/D=5)

As expected, the trends shown here are similar to the heat transfer trends, highlighting the areas where the heat transfer is above or below the mean value. Considering the scale used, the overall performance of all channels is quite good, with only 50% variations in the downstream region of Case 5.4.5. All other cases are above about UC=0.75. This high level of uniformity is not initially expected, as we know there are peaks of high heat transfer in the vicinity of the stagnation region. However, due to the nature of the cross flow heat transfer effects and the close spacing of the jets (5 diameters), the profile turns out to be rather uniform. Similar effects are seen on the side wall surfaces. Again, Case 5.4.5 tended to be the least uniform in most regions. As expected, in locations of high heat transfer, especially near the locations of the wall jet impact, the uniformity values drop. It is interesting to note, however, that Case 5.4.3B seems to yield the most uniform profiles on both surfaces.

As mentioned earlier, the spanwise averaged uniformity distribution was included
with the heat transfer results (Figure 7-37, Figure 7-38, Figure 7-39, Figure 7-40).

Figure 7-37: Span-Averaged Uniformity and Heat Transfer Distribution (Case 5.4.1A)

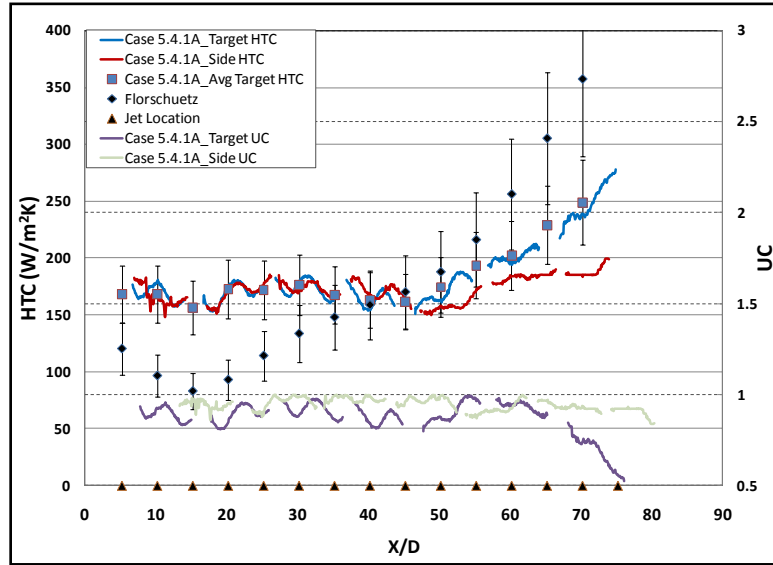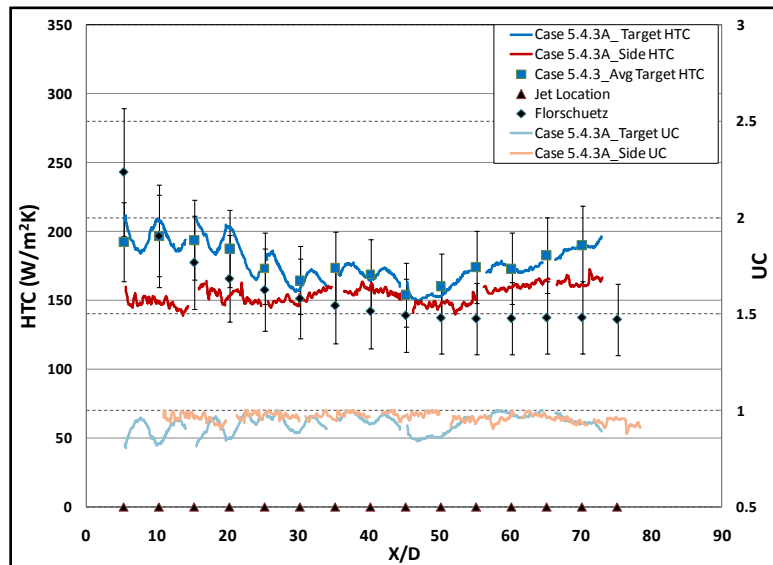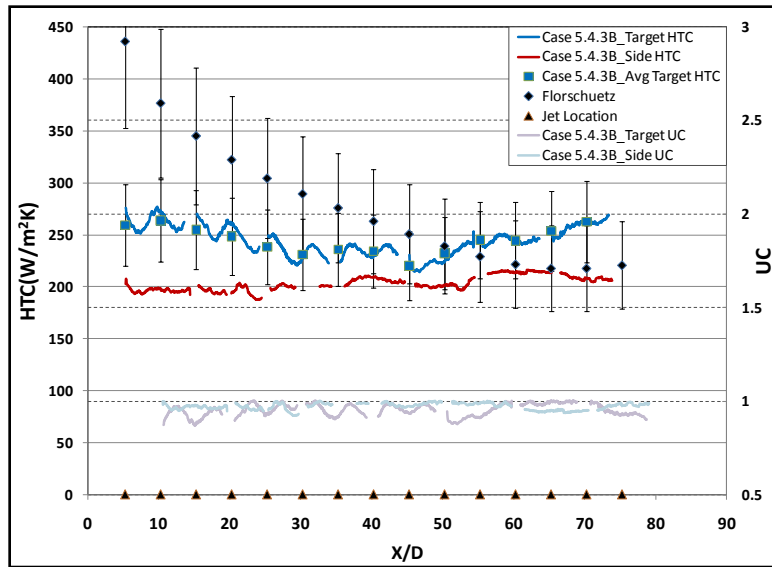**Figure 7-38: Span-Averaged Uniformity and Heat Transfer Distribution (Case 5.4.3A)**

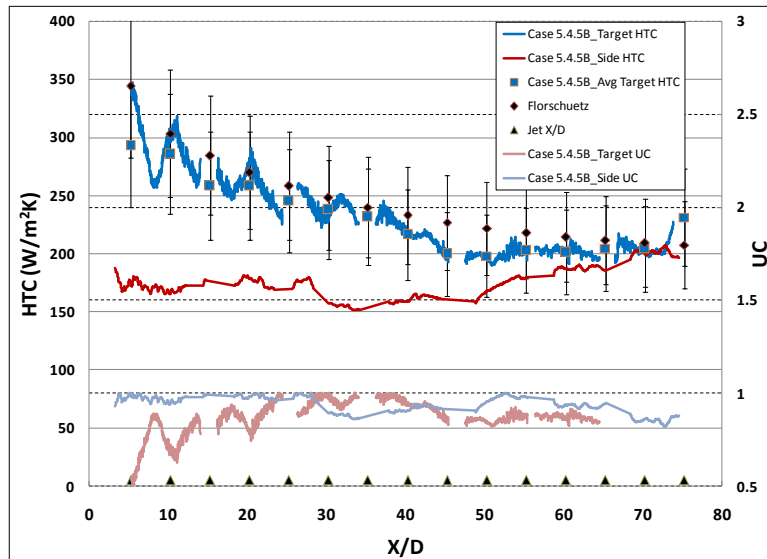**Figure 7-39: Span-Averaged Uniformity and Heat Transfer Distribution (Case 5.4.3B)**

Figure 7-40: Span-Averaged Uniformity and Heat Transfer Distribution (Case 5.4.5B)

The direct relationship between the uniformity and the heat transfer distribution is again apparent. Considering all cases, we see that the side wall surfaces tended to be

more uniform for most of the channel length. This is most likely due to the fact that most of the heat removed on these surfaces is due to the cross flow produced. Examining the target surface plots for all 4 cases, it is apparent that the jets have a negative effect on the uniformity. Also interesting to note is the rapid decrease in uniformity near the exit of the channel for Case 5.4.1. This is due to the large increase in cross flow and jet velocity in this region. Again, it is obvious that Case 5.4.5 performed the worst, with large variations in heat transfer coefficient in the upstream regions. The jets then play multiple roles, as they are beneficial in the fact that they significantly increase heat transfer, yet they also tend to decrease the uniformity in these locations. Nevertheless, the channel heights and average Reynolds number tend to play a major role in the overall uniformity, especially on the target surface. At small channel heights, strong impingement leads to non-uniformities, while at larger channel heights poor interaction between the jets and cross flow yield large variations. These effects are more clearly shown in Figure 7-41.
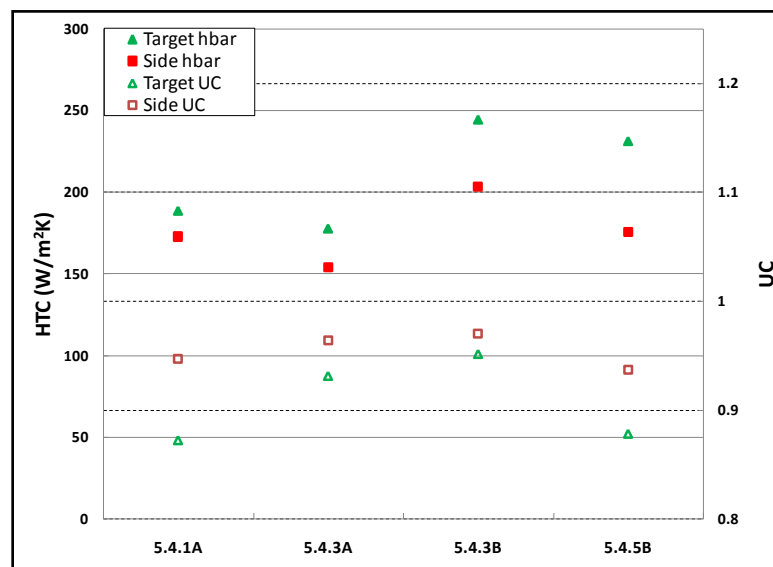
Figure 7-41: Overall Uniformity Comparison (X/D=5)

Here the average heat transfer coefficient and uniformity coefficients are plotted for each case and surface. The benefit of this simultaneous comparison becomes apparent immediately, as Case 5.4.3B seems to outperform the others not only with higher heat transfer coefficients, but tended to be more uniform as well. As mentioned, the target surface consistently removes more heat, while the side wall surfaces are consistently more uniform, especially with cases 5.4.1 and 5.4.5. Interesting to note is that although Case 5.4.5 yields relatively high heat transfer coefficients, the profiles tend to be non-uniform. This is a direct result of the larger channel size employed in this case, where the jets were not able to sufficiently cover the entire side wall, and proper impingement only occurred in the upstream locations on the target surface. Case 5.4.3 tended to be the most uniform at all Reynolds numbers, while the heat transfer coefficient tended to decrease as the channel height increased, holding Reynolds number constant. This optimal channel height is an ideal balance between sufficient jet impact, and the uniform effects of the cross flow, where high heat transfer coefficients are produced, but with minimal gradients. For example, consider Case 5.4.3A and Case 5.4.5. Although Case 5.4.5 yields higher heat transfer coefficients, the uniformity is less. Case 5.4.3A may be a better choice depending on the design requirements. Although one case stands out as the ideal geometry, it is important to mention that all cases yield high uniformity coefficients, within 15% of a perfect distribution.

7.7.3   X/D=15

A similar analysis is carried out for the cases with a jet to jet spacing of 15 diameters. Ideally one would achieve similar performance at equal average jet Reynolds numbers, however with only a third of the total mass flow. This would be ideal, unless the thermal stresses induced are greater. From our previous analysis, one can see the variations are much greater for these larger spaced channels, suggesting that the uniformity distributions will also suffer. Figure 7-42 and Figure 7-43 show the local uniformity distributions.
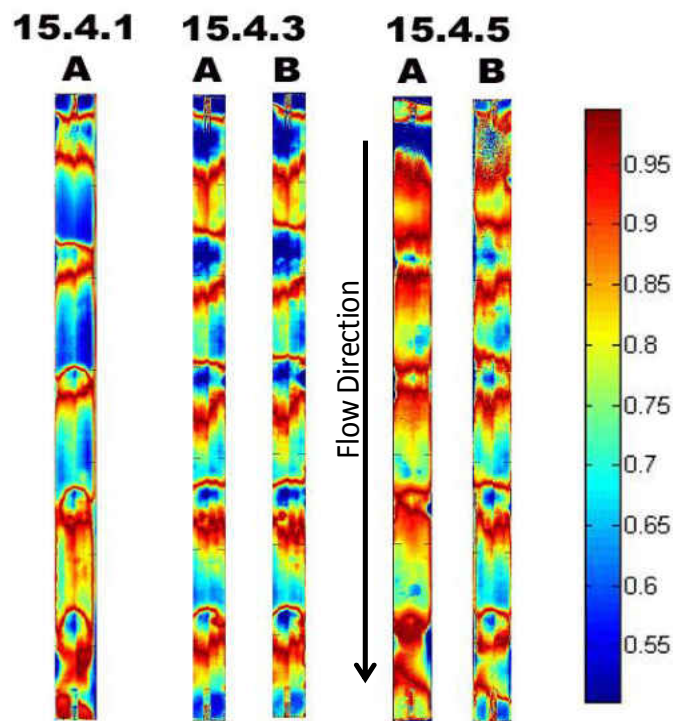

Figure 7-42: Target Wall Uniformity Distributions (X/D=15)
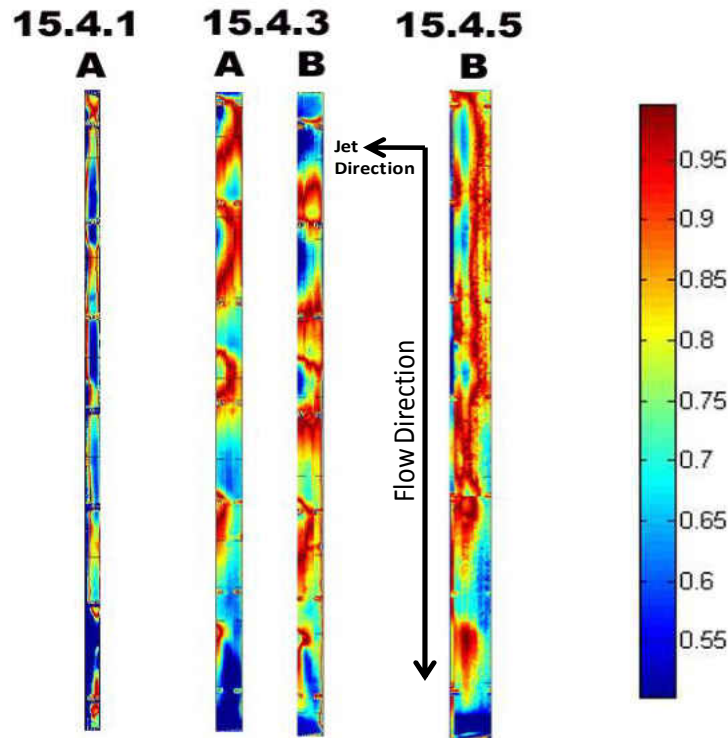
Figure 7-43: Side Wall Uniformity Distributions (X/D=15)

Immediately one notices much more variations across the distribution. This was evident in the heat transfer results, as the longer hole to hole spacing yields larger variations from jet to jet. Similar to the previous cases, the stagnation regions, both from the jet and wall jet impingement, are areas of low uniformity, as the heat transfer peaks in these locations. There are much more regions of low uniformity (<0.7), as compared to the previous cases. The impingement locations tend to produce low values of uniformity, with the uniformity increasing and then again decreasing as one moves away from the impingement location. This initially makes sense, as the decaying impingement effects would pass through the average levels of heat transfer.

It is also important to note the similarity between the two Reynolds number variations for case 15.4.3. The profiles are nearly identical for the target surface, and

very similar for the side wall, suggesting that changes in channel geometry play a largest role in affecting the uniformity distributions; especially at large X/D. Once again, the side walls tend to outperform the target surface in terms of uniformity of the profile. The following figures highlight the spanwise averaged results, again plotted along with heat transfer coefficient (Figure 7-44, Figure 7-45, Figure 7-46, Figure 7-47, Figure 7-48).
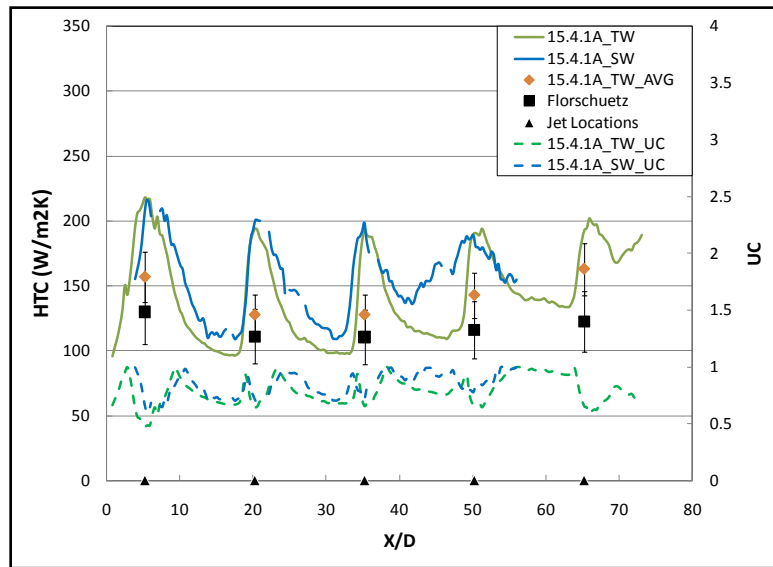
Figure 7-44: Span-averaged uniformity and heat transfer distribution (15.4.1A)

Similar to the previous cases, we see the direct relationship, as expected between the heat transfer coefficient and the uniformity distribution. Regions of impingement, and the regions midway between impingement locations, lead to low uniformity coefficients. While other regions approach the average value. This is somewhat more severe in the wide spaced array than the previous cases. This is due to the increased distance between jets, gives ample time for the effect of the jet to decay.
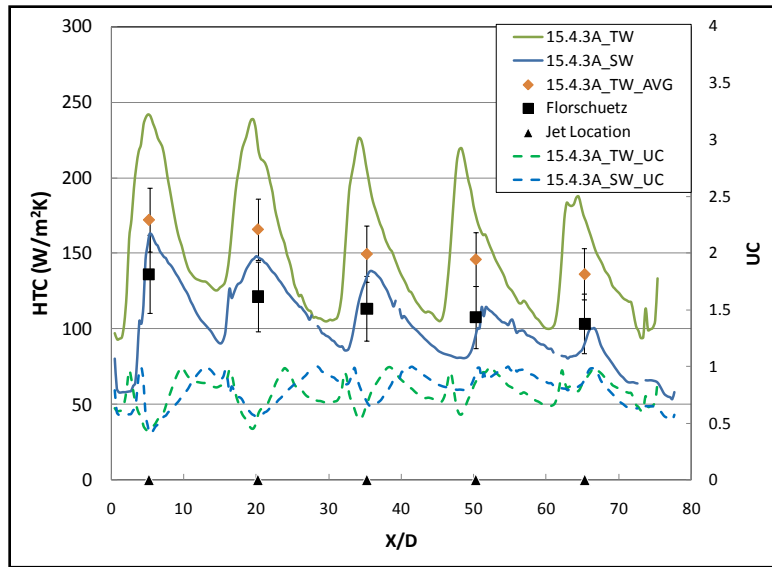
Figure 7-45: Span-averaged uniformity and heat transfer distribution (15.4.3A)

Similar results are seen for case 15.4.3A. Again, regions between the peaks and valleys in heat transfer, as expected, approach a uniformity of 1. Other regions suffer from excessively high or low heat transfer rates. This does leave the opportunity, however, for intelligently placed impingement jets at regions of flux concentrations.
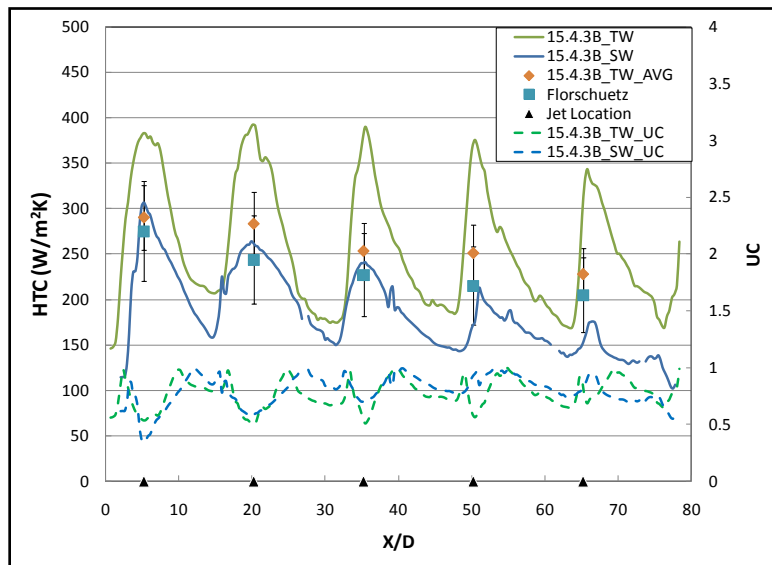
Figure 7-46: Span-averaged uniformity and heat transfer coefficient (15.4.3B)

As expected, the high Reynolds number case of geometry 15.4.3 has almost identical uniformity distribution. This was also evident in the local plots. It can also be seen that as the channel height is extended and the side wall performance decreases, the uniformity of the side wall tends to increase slightly.
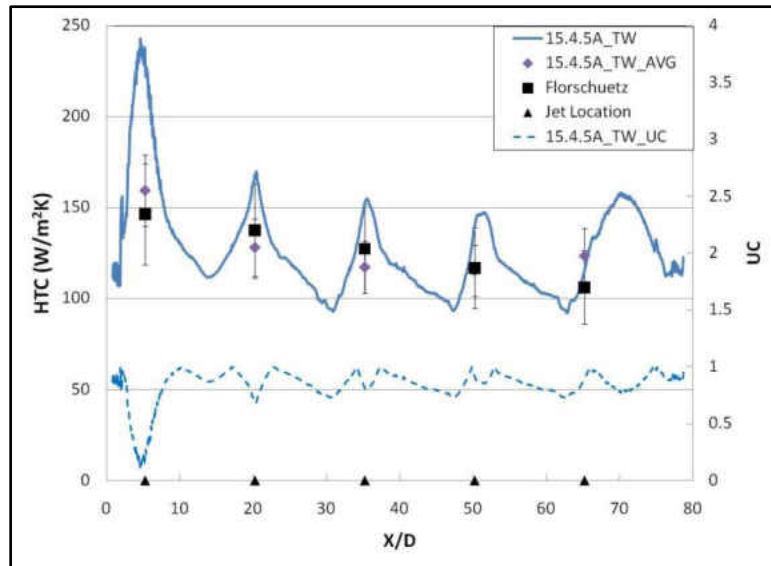
Figure 7-47: Span-averaged uniformity and heat transfer coefficient (15.4.5A)

Similar to the previous cases, for the tallest channel height, there is the largest peak in heat transfer at the first jet. This of course leads to a deficit in uniformity at these locations. This case, however, tends to perform very well in terms of uniformity in the downstream direction, oscillating very close to 1. This results from the lower magnitude of the oscillations in the heat transfer coefficient, as compared to the previous cases. The lessened jet impact velocity resulting from these tall channel heights leads to lower impingement heat transfer coefficients.

150
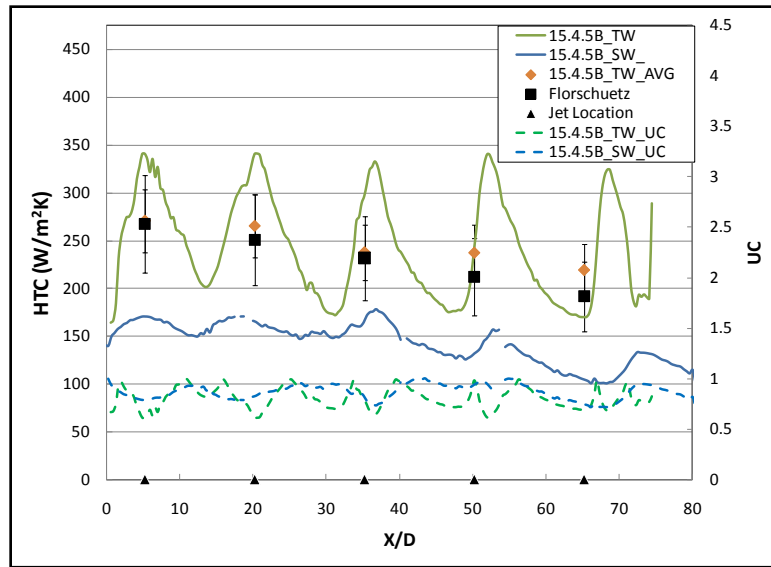
Figure 7-48: Span-averaged uniformity and heat transfer coefficient (15.4.5B)

For case 15.4.5B, we see the best performance for the side wall. However, the performance is much less than the target surface, which may not be acceptable for certain designs. Similar to the previous, low Reynolds number case, the target wall also tends to perform well due to the smaller oscillations in heat transfer coefficient.

In order to get a complete comparison of the uniformity and heat transfer effects of the cases with jet to jet spacing of 15 diameters, average heat transfer coefficient and uniformity coefficients are plotted in Figure 7-49.
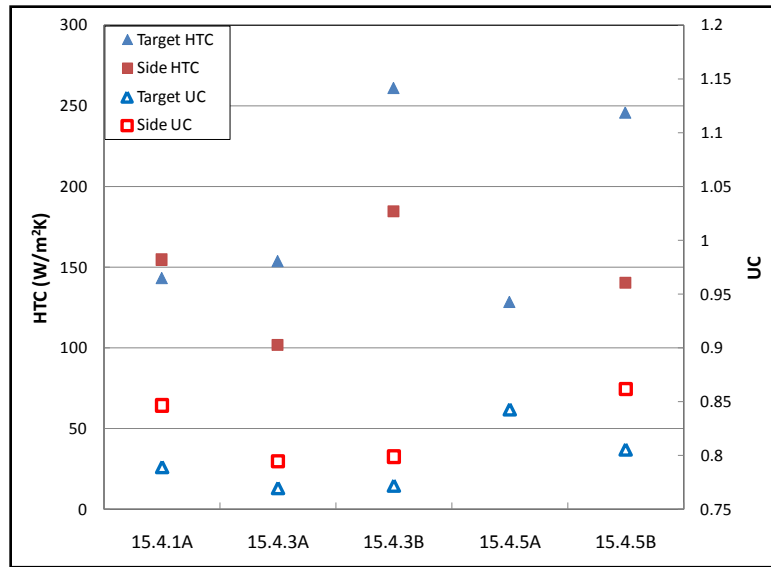
Figure 7-49: Overall uniformity and heat transfer coefficient comparison (X/D=15)

Contrary to the cases with a jet to jet spacing of 5 diameters, the best choice is not as clear for the current configuration. Although case 15.4.3B performs the best in terms of heat transfer coefficient, case 15.4.5A and B performs better in terms of uniformity. It is interesting to note, that when compared to the previous cases (X/D=5), the difference in uniformity between cases 5.4.3A and B was much more significant that for the current case. This may be the result of a larger spacing, suggesting that the benefit of the increased Reynolds number on uniformity does not occur until the number of jets is increased. However, the change in heat transfer coefficient is significant for both scenarios. In terms of a balance between uniformity and heat transfer levels, it seems that case 15.4.3B or 15.4.5B would be most beneficial, depending on the exact needs of the application.

7.8   Thermal Performance

7.8.1   Introduction

In order to obtain a fair comparison of the performance of each channel configuration, the thermal effectiveness of each was compared. It is expected that there is a single case where the increase in heat transfer outweighs the increase in pressure drop required. From the previous analysis, it was apparent that the enhancement of each configuration varies, and is also slightly dependant on the definition used for enhancement levels (computed at the maximum channel Reynolds numbers). A clear understanding of what the heat transfer enhancement, friction factor enhancement, and thermal performance definitions is required at this point.

As all of these definitions are based off of channel exit conditions (maximum values), a comparison against an equivalent smooth channel of equal total mass flow rate and equal dimensions is made. As previously discussed, although the pressure required for most cases is larger, due to the additional work required to push the flow across the jet plate, the heat transfer levels are much higher than for an equivalent channel. However, when we consider a thermal performance, considering equal pumping power, one must keep in mind that the large heat transfer levels achieved with these cases are only possible by employing additional work to develop the jets. For this case, one expects thermal performance factors that are below one, since the pressure drop across the orifice plate is the major contributor to the calculated friction factor.

7.8.2   X/D=5

Examining Figure 7-50, we see that the effectiveness decreases as the channel height and Reynolds number increases.

153

$(h/h_0)/(f/f_0)^{1/3}$

| | 5.4.1A | 5.4.3A | 5.4.3B | 5.4.5B |
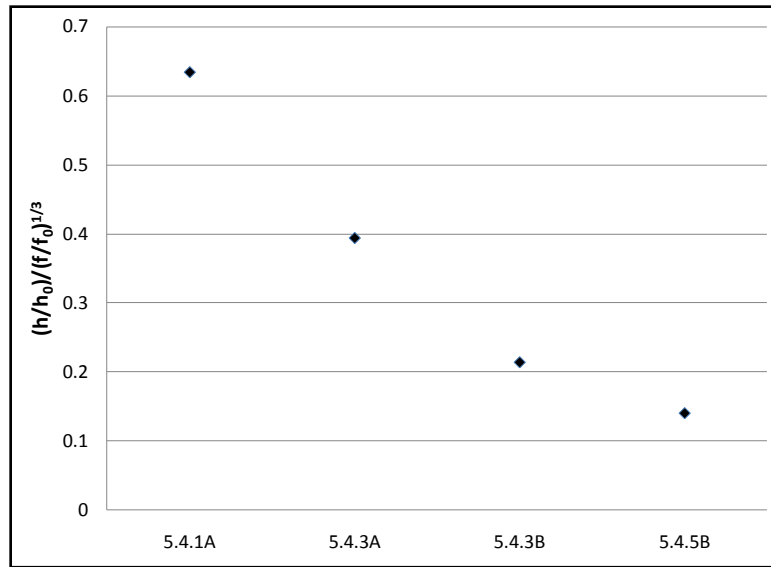
Figure 7-50: Thermal Performance Comparison (X/D=5)

Although Case 5.4.3B yielded the most uniform results, Case 5.4.1 was most efficient when considering the pumping power required for each case. The high effectiveness values for Case 5.4.1 can be attributed to the large heat transfer levels on the side walls, which were comparable to that on the target wall. Because of the small channel height, both the side and target surfaces benefited from the impingement features found within the channel. As the channel height increased, the heat transfer on the side walls was not as beneficial and lowered the channel average. Also, comparing Case 5.4.3A and 5.4.3B, as Reynolds number increased, the effect of the jets was less significant when compared to traditional channel flow. It then becomes obvious that the best channel design, when considering the thermal effectiveness, would be that of a small channel height and lower Reynolds numbers. However, designers may have to consider other factors when designing impingement channels, such as profile uniformity.

154

7.8.3 X/D=15

As previously discussed, the definitions used here play a major role in the values obtained in the analysis. However, similar cases can be compared with confidence since major contributors are the same. This point is important when considering the cases with a 15 diameter jet spacing, as the reduced number of jets leads to lower cross flow Reynolds numbers, and thus lower calculated baseline values. However, the same pressure ratio is required to push the same average jet Reynolds number across the reduced number of jets. This leads to some bias in the definition, where if the channel was made increasingly long, the effect of the large driving pressure would become less apparent. This was the case for the previous data set, where the cross flow velocities were large enough to produce comparable baseline values in the downstream region. Figure 7-51 represents this analysis for the current data set.
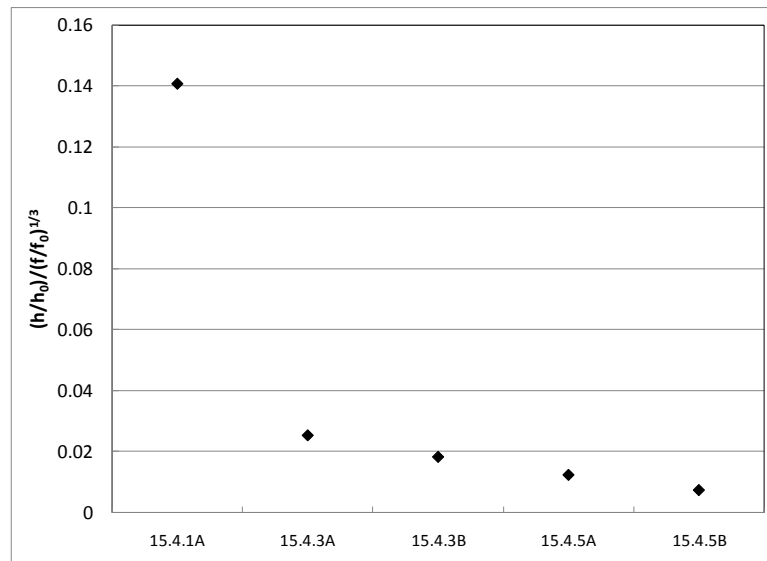
Figure 7-51: Thermal Performance Comparison (X/D=15)

Once again there is a decrease in performance as we increase channel height and Reynolds number. However, as mentioned, the values obtained here are very small, due to the resulting low cross flow Reynolds numbers. As the trends are very similar to the previous cases (with the addition of the point 15.4.5A), we can make similar conclusions. The smallest channel height performed the best, due to the large velocities achieved at the exit, along with the side wall performance being comparable to the target surface. As we increase channel height, the contributions of the side wall decrease and the baseline values decrease as well. Increases in Reynolds numbers lead to a decrease in performance under these considerations. This is due, again, to the increased turbulence levels associated with the increased Reynolds numbers begins to outweigh, somewhat, the effect of impingement. Although not as severe for the previous geometry, it again is an effect here. Nevertheless, this comparison is necessary in order to aid designers in proper cooling channel selection.

CHAPTER 8   **CONCLUSION**

8.1   Conclusion

The preceding study has completely characterized the cooling characteristics of an inline row impingement channel. Numerical results were presented in order to give insight into the complex behavior within these channels, allowing a more thorough explanation of the heat transfer behavior observed experimentally. These experimental results allow comparison of multiple performance characteristics, (heat transfer coefficients, friction factors, uniformity coefficients, thermal performance), under varying jet spacing, impingement heights, and jet Reynolds numbers.

Several conclusions and contributions can be made from this work. It has been shown that the side walls provide significant heat transfer from an impingement jet, and may prove beneficial in near wall cooling designs. This is especially true at small Z/D. With the accumulation of cross flow, high levels of heat transfer are still achieved, even without the impact of the wall jet. The presence of these side walls did not affect the predicted pressure profiles, however did affect predicted heat transfer results. Deviations tended to be the largest for smaller channels of a jet spacing of 5 diameters.

A friction factor was defined for the channel arrangement, with enhancements depending heavily on the velocities of the cross flow at the channel exit. As the majority of the pressure drop was across the jet plate, smaller channel sizes benefited from the lowest friction factors, and largest thermal performances. Increasing the jet spacing generally affected both of these negatively.

A uniformity coefficient was also defined, so that comparisons could be made between the potential thermal stresses caused by each design. It was shown that although decreased jet spacing does not result in significant increases in heat transfer performance, the profiles are superior in terms of uniformity. Side walls were generally more uniform than target surfaces, due to the increased contributions of cross flow. Moderate channel heights and high Reynolds numbers typically yielded the best results. It is then the challenge of the designer to balance the various tradeoffs presented.

Considerations were also given toward the development of the bulk temperature within these channels, showing that critical information can be extracted from their analysis. This included identification of regimes where the cross flow effects begin to become important. This was also made apparent through comparisons to smooth channel predictions, where it was shown that provided enough cross flow, enhancement levels tended toward one. Existing correlations were also shown to hold quite well in these regions, as the side wall effects were minimized.

It was also shown how boundary conditions can affect the results in several ways. Most dramatically, the actual bulk temperature may be affected by the number of thermally active walls. Since the jet temperature is typically taken as the reference temperature in these calculations, this difference would not be accounted for as it would in a traditional channel flow scenario. However, the effects were shown to me generally negligible for the conditions tested.

As improvements in turbine efficiency become more and more difficult to achieve, there becomes a need for multi-disciplinary approaches to research. This requires a complete description of the performance of these channels, a need that has

been alluded to in the literature. The gap between industry application and academic research will always be a hurdle technology will have to overcome, and should continue to be a focus of engineers.

8.2   Future Work

Because the potential for highly effective cooling techniques exists when considering impingement channel cooling concepts, investigations in this area would be quite beneficial. The fact that the wall jets have the ability of contributing to the heat removed is something that deserves further attention. This can be exploited through the sophisticated use of surface features within the channel. The concept of heat transfer uniformity is something that must also be pursued, as reductions in thermal stresses are necessary for future advancements in efficiency.

APPENDIX: RIG DRAWINGS
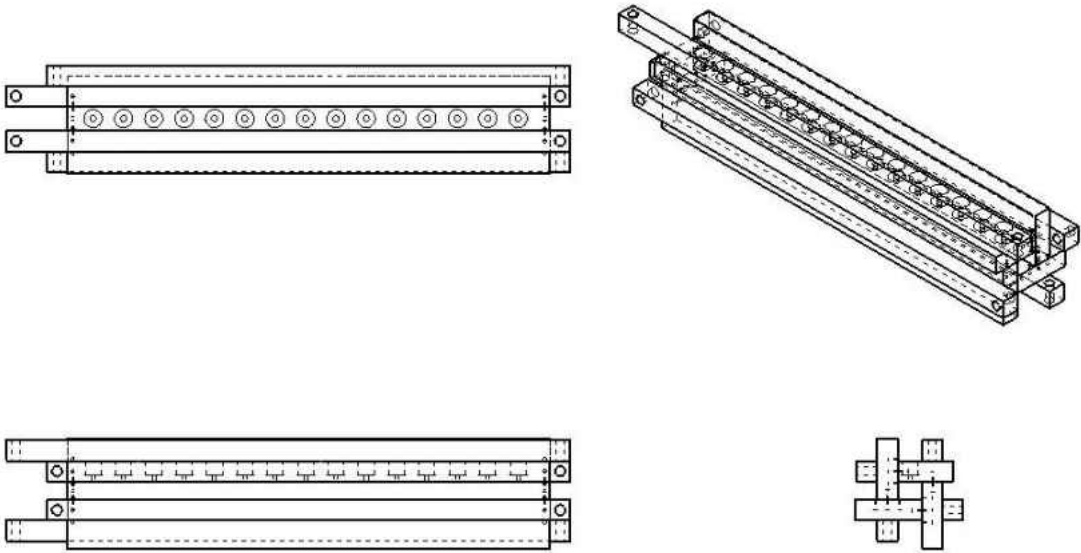
Pressure Driven Rig Assembled
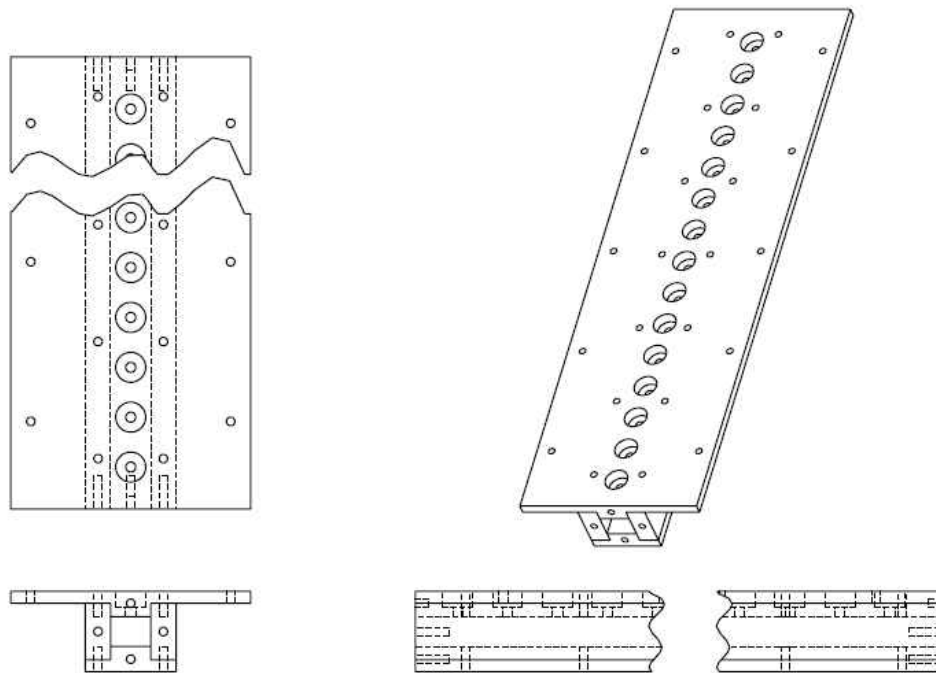
Suction Driven Test Section Assembled

REFERENCES

Al-Aqal, O. M. A, 2003, "Heat transfer distributions on the walls of a narrow channel with jet impingement and cross flow", PhD Thesis, University of Pittsburgh.

Annerfeld, M., Johan, P., Torisson, T., 2001. "Experimental Investigation of Impingement Cooling with Turbulators or Surface Enlarging Elements," Proc. Of ASME turbo Expo, 2001-GT-0149.

Barrow, H., "Convection Heat Transfer Coefficients for Turbulent flow Between Parallel Plates with Unequal Heat Fluxes," Int. J. Heat Mass Transfer, Vol. 1, 1961, pp. 306-311.

Bell, James, Schairer, E., Hand, L., Mehta, R., 2001, "Surface Preassure Measurements Using Luminescent Coatings," Journal of Fluid Mechanics, 33, pp 155-206.

Black, A.W., Sparrow, E.M., 1967. "Experiments on Turbulent Heat Transfer in a Tube with Circumferentially Varying Thermal Boundary Conditions," Trans. ASME 89C, pp. 258-268.

Bower, W., Saripalli, K., Agarwal, R., 1981. "A Summary of Jet impingement Studies at Mc Donnell Douglas Research Laboratories," Paper AIAA-81-2613, VSTOL Conference, Palo Alto, California.

Boyce, M.P., 2006, Gas Turbine Engineering Handbook, Gulf Professional Publishing, 3rd edition, pp 47-48.

Bradbury, L.J.S., 1965. "The Structure of a Self-Preserving Turbulent Plane Jet." J. of Fluid Mechanics, Vol. 23, pp. 31-64.

Bunker, Ronald S., 2007, :Gas Turbine Heat Transfer: Ten Remaining Hot Gas Path Challenges," Journal of Turbomachinery, April, Vol. 129, pp. 193-201.

Chyu, M.K., Ding, H., Downs, J.P., Van Sitemdae, M., Soechting, P.O., 1997. "Determination of Local Heat Transfer Coefficient Based on Bulk Mean Temperature using a Transient Liquid Crystals Techniques," ASME paper 97-GT-489.

Chyu, M.K., Siw, S., Karaivanov, V., Slaughter, W., Alvin, M., 2009, "Aerothermal Challenges in Syngas, Hydrogen—Fired, and Oxyfuel Turbines- Part II: Effects of Internal Heat Transfer," Journal of Theral Science and Engineering Applications, March, Vol. 1, pp. 1-10.

Clifford, R.J., 1985. "Rotating Heat Transfer Investigations on a Multipass Cooling Geometry." AGARD CP 390.

Downs, James P., Landis, Kenneth K., 2009, "Turbine Cooling Systems Design- Past, Present and Future." Proceedings of ASME Turbo Expo 2009, June 8-12, 2009, GT2009-59991.

El-Gabry, Lamyaa, Kaminski, D., 2005, "Numerical Investigation of Jet Impingement with Cross Flow- Comparison of Yang-Shih and Standard k-ε Turbulence Models," Journal of Numerical Heat Transfer, Part A: Applications, 47:5, pp 441-469.

Eckert, E.R.G., and Livingood, John N. B, 1953. "Method for calculation of laminar heat transfer in air flow around cylinders of arbitrary cross section." NACA Rep. 1118.

Florschuetz, L.W., Berry, R. A., Metzger, D. E, 1980, "Periodic streamswise variations of heat transfer coefficients for inline and staggered arrays of circular jets with cross flow of spent air." ASME J. of Heat Transfer, 102: p. 132-137.

Florschuetz, L. W., Truman, C. R., Metzger, D. E., 1981, "Streamwise Flow and Heat Transfer Distributions for Jet Array Impingement with Cross flow," Journal of Heat Transfer, Vol. 103, pp. 337.

Florschuetz, L. W., Isoda, Y., 1983, "Flow Distributions and Discharge Coefficient for Jet Array Impingement With Initial Cross flow", Journal of Engineering for Power, Vol. 105, pp. 296.

Fox, M.D., Kurosaka, M., Hedges, L., Hirano, K., 1993, "The Influence of Vortical Structures o n t he Thermal Fields of Jets," Journal of Fluid Mechanics, Vol. 255, pp. 447-472.

Gallego, N.C., Klett, J.W., 2002. "Carbon Foams For Thermal Management," International Seminar on Advanced Applications for Carbon Materials, Jeju Island, Korea.

Gauntner, J.W., Livingood, J. N. B., 1970. "Survey of literature on flow characticstics of a single turbulent jet." NASA TN D-5652.

Gladden, H.J., Simoneau, R.J., 1988. "Review and Assesment of the Database and Numerical Modeling for Turbine Heat Transfer." In Toward Improved Durability in Advanced Aircraft Engine Hot Sections, edited by D.E. Sokolowski. IGTI, Vol 2. Pp. 39-55.

Glauert, M.B., 1956. "The wall jet." J. Fluid Mech., Vol 1(6): p. 625-643.

Han, J.C., Dutta, S., Ekkad, S., 2000, "Turbine Blade Internal Cooling," Turbine Heat Transfer and Cooling Technology, 1st ed, Vol. 1, Taylor & Francis, New York, 2000, pp 17-21.

Hilgeroth, E., 1965, "Heat Transfer for Jet Flow Perpendicular to the Exchange Surface," Techn 37, Jahrg/ NR 12, pp. 1264-1272

Hoogendoorn, C.J., 1977. "The effect of Turbulence on Heat Transfer at a Stagnation Point," Int. J. Heat Mass Transfer, Vol 20, pp 1333-1338.

Incropera, Frank P., DeWitt, D. P., 2002, Fundamentals of Heat and Mass Transfer, John Wiley & Sons, Inc., New Jersey, pp. 491-493.

Ito, Shoko, Saeki, H., Inomata, A, et al, 2005, "Conceptual Design and Cooling Blade Development of 1700C Class High Temperature Gas Turbine," Journal of Engineering for Gas Turbines and Power, Vol. 127, April, pp. 358-368.

Javadi, Khodayar, Javadi, Aliyar, 2008 "Introducing Film Cooling Uniformity Coefficient (CUC)," Proceedings of IMECE 2008, ASME, Boston, MA, IMECE2008-68502.

Kercher, D.M., Tabakoff, W., 1970, "Heat Transfer by a Square Array of Round Air Jets Impinging Perpendicular to a Flat Surface Including the Effect of Spent Air," Journal of Engineering for Power, pp. 73-82.

Liu, Quan, Kapat, J. May 2006, "Study of Heat Transfer Characteristics of Impinging Air Jet Using Pressure and Temperature Sensitive Luminescent Paint", UCF Dissertation

Liu, Xin, Lienhard, J., Lombara, J.,1990, "Convective Heat Transfer by Liquid Jet Impingement," Journal of Heat Transfer, 113:3, pp. 571-582.

Livingood, J.N.B., Hrycak, P., 1973. "Impingement heat transfer from turbulent air jets to flat plates—a literature survey." NASA TR I-2778.

Lucas, M.G., Ireland, P.T., Wang, Z., 1992, "Fundamental Studies of Impingement Cooilng Thermal Boundary Conditions," AGARD 80th PEP Symposium, Paper no. 14.

Martin, H., 1977. "Impinging jet flow heat and mass transfer." Advances in heat transfer, Vol. 13.

Mushatat, Khudheyer, 2007. "Analysis of the Turbulent Flow and Heat transfer of the Impingement Cooling in a Channel with Cross flow," JKAU: Eng. Sci., Vol 18, No 2, pp 101-122.

Park, Jongmyung, Goodro, M., Ligrani, P., Fox, M., Moon, H., 2006, "Separate Effects of Mach Number and Reynolds Number on Jet Array Impingement Heat Transfer," Proceedings of Turbo Expo 2006, May, GT2006-90628.

Remley, T.J., Abdel-Khalik, S.I., Jeter, S.M., 2001. "Effect of nonuniform heat flux on wall friction and convection heat transfer coefficient in a trapezoidal channel," Int. J. Heat Mass Transfer, vol. 44, pp. 2453-2459.

Reynolds, W.C., "Turbulent Heat Transfer in a Circular Tube with Variable Circumferential Heat Flux," Int. J. Heat Mass Transfer, Vol. 6, 1963, pp. 445-454.

Sautner, M., Clouser, S., Han, J.C., 1992. "Determination of Surface Heat Transfer and Film Cooling Effectiveness in Unsteady Wake Flow Conditions." AGARD Conference Proceedings 527, pp. 6-1 to 6-12.

Sierra, Fernando, Bolaina, C., Jubiak, J., Han, J.C., et al, 2009, "Heat Transfer and Thermal Mechanical Stress Distributions in Gas Turbine Blades," Proceedings of ASME Turbo Expo 2009, GT2009-59194.

Son, C., Gillespie, D., Ireland, P., Dailey, G., 2001, "Heat Transfer and Flow Characteristics of an Engine Representative Impingement Cooling System," Journal of Turbomachinery, published January 2001; Vol. 123, pp 154-160.

Sparrow, E.M., Lin, S.H., "Turbulent Heat Transfer in a Tube with circumferentially Varying Temperature or Heat Flux," Int. J. Heat Mass Transfer, vol. 6, 1963, pp. 866-867.

Taylor, J.R., 1980. "Heat Transfer Phenomena in Gas Turbines." ASME Paper 80-GT-172.

U. Uysal, P-W. Li, M.K. Chyu, F.J. Cunha. 2005 "Heat transfer on internal surfaces of a duct subjected to impingement of a jet array with varying jet hole-size and spacing". GT2005-68106

Van Truen, K.W., Wang, Z., Ireland, P.T., "Detailed Measurements of Local Heat Transfer Coefficient and Adiabatic Wall Temperature Beneath an Array of Impinging Jets," J. Turbomachinery, vol. 116, 1994, 369-374.

Van Treuren, Kenneth, Wang, Z., Ireland, P., Jones, T., Kohler, S., 1996, "Comparison and Prediction of Local and Average Heat Transfer Coefficients Under an Array of Inline and Staggered Impinging Jets," Proceedings of International Gas Turbine and Aeroengine Congress & Exposition, June, 96-GT-163.

Viskantam R., 1993. "Heat Transfer to Impinging Isothermal Gas and Flame Jets." Experimental Thermal and Fluid Science, Vol. 5, pp. 111-134.

Yan, X., Baughn, J.W., Mesbeh, M., 1992. "The effect of Reynolds Number on the Heat Transfer Distribution from a Flat Plate to an Impinging Jet," Proceesings of the ASME Winter Annual Meeting, Anaheim California.

PUBLICATIONS RESULTING FROM THIS WORK

Ricklick, Mark, Kersten, S., Krishnan, V., Kapat, J.S., 2008, "Effects of Channel Height and Bulk Temperature Considerations on Heat Transfer Coefficient of Wetted Surfaces in a Single Inline Row Impingement Channel," Proceedings of the 2008 ASME Summer Heat Transfer Conference. Jacksonville, Florida. August 2008, HT2008-56323

Ricklick, Mark, Kersten, S., Krishnan, V., Kapat, J.S., 2008, "Effects of Circumferential Heating Variations and Channel Height on Heat Transfer Coefficient of Wetted Surfaces in a Single Inline Row Impingement Channel," Proceedings of IMECE 2008. Boston, MA. November 2008, IMECE2008-67787

Ricklick, Mark, Kapat, J.S., Heidmann, J., 2009, "Channel Height and Wall Effects on Surface HTC in a Narrow Impingement Channel" AIAA Aerospace Science Meeting 2009. Orlando, FL. January 2009, AIAA2009-91430

Ricklick, Mark, Kapat, J.S., 2009, "Determination of a Local Bulk Temperature Based Heat Transfer Coefficient for the Wetted Surfaces in a Single Inline Row Impingement Channel," Proceedings of the 2009 ASME Turbo Expo. Orlando, FL. June 2009, GT2009-59327

Ricklick, Mark, Kapat, J.S., 2009, "Comparison of Heat Transfer Uniformity of a Narrow Impingement Channel," Proceedings of the 2009 AIAA Joint Propulsion Conference. Denver, CO. August 2009, AIAA2009-5379

Ricklick, Mark, Kapat, J.S., Heidmann, J., 2009, "Side Wall Effects on Heat Transfer Coefficient in a Narrow Impingement Channel," AIAA Journal of Thermophysics and Heat Transfer.

Ricklick, Mark, Kapat, J.S., 2009, "Determination of a Local Bulk Temperature Based Heat Transfer Coefficient for the Wetted Surfaces in a Single Inline Row Impingement Channel," ASME Journal of Turbomachinery.